
Electronic Thesis and Dissertation Repository

8-18-2014 12:00 AM

Observational Signatures from Self-Gravitating Protostellar Disks

Alexander L. DeSouza, *The University of Western Ontario*

Supervisor: Dr. Shantanu Basu, *The University of Western Ontario*

A thesis submitted in partial fulfillment of the requirements for the Doctor of Philosophy degree in Astronomy

© Alexander L. DeSouza 2014

Follow this and additional works at: <https://ir.lib.uwo.ca/etd>



Part of the [Cosmology, Relativity, and Gravity Commons](#), [Numerical Analysis and Computation Commons](#), and the [Stars, Interstellar Medium and the Galaxy Commons](#)

Recommended Citation

DeSouza, Alexander L., "Observational Signatures from Self-Gravitating Protostellar Disks" (2014). *Electronic Thesis and Dissertation Repository*. 2329.
<https://ir.lib.uwo.ca/etd/2329>

This Dissertation/Thesis is brought to you for free and open access by Scholarship@Western. It has been accepted for inclusion in Electronic Thesis and Dissertation Repository by an authorized administrator of Scholarship@Western. For more information, please contact wlsadmin@uwo.ca.

OBSERVATIONAL SIGNATURES FROM SELF-GRAVITATING
PROTOSTELLAR DISKS
(Thesis format: Integrated Article)

by

Alexander Leonard DeSouza

Graduate Program in Physics & Astronomy

A thesis submitted in partial fulfillment
of the requirements for the degree of
Doctor of Philosophy

The School of Graduate and Postdoctoral Studies
The University of Western Ontario
London, Ontario, Canada

© Alexander Leonard DeSouza 2014

Abstract

Protostellar disks are the ubiquitous corollary outcome of the angular momentum conserving, gravitational collapse of molecular cloud cores into stars. Disks are an essential component of the star formation process, mediating the accretion of material onto the protostar, and redistributing excess angular momentum during the collapse. We present a model to explain the observed correlation between mass accretion rates \dot{M} and stellar mass M_* that has been inferred from the observations of intermediate to upper mass T Tauri stars—that is $\dot{M} \propto M_*^{1.3 \pm 0.3}$. We explain this correlation within the framework of gravitationally driven torques parameterized in terms of Toomre’s Q criterion. Our models reproduce both the observed correlation and spread in the $\dot{M} - M_*$ relation as has been observed for protostars with masses of $0.2 M_\odot \leq M_* \leq 3.0 M_\odot$, such as those found in the ρ Ophiuchus and Taurus star forming regions.

We also examine the formation and long-term evolution of primordial protostellar disks harbored by the first stars (Population III stars), using 2+1D numerical hydrodynamics simulations in the thin-disk limit. The disks that form in the primordial environment are very massive and subject to vigorous fragmentation. Fragments torqued inward due to gravitational interactions with sub-structure within the disk give rise to accretion and luminosity bursts several orders of magnitude above the mean rate—the first evidence for the burst mode of accretion among Population III stars. By considering the cosmological landscape in this epoch, we argue from the Jeans criterion for the existence of clusters of Population III stars. A simultaneity of burst mode accretion events among several cluster members results in fluctuations that are nearly $1000\times$ greater than the mean cluster luminosity, resulting in a total luminosity above $10^8 L_\odot$. This phenomenon arises solely as a result of the gravitational-instability–driven episodic fragmentation and accretion that characterizes this early stage of protostellar evolution. We speculate as to how these extrema may provide a window through which next-generation telescopes will be able to gather observational evidence for the existence of the first stars.

Keywords: accretion disks—cosmology: theory—hydrodynamics—stars: formation—stars: Population III—stars: protostellar disks

Co-Authorship Statement

The idea for the work presented as Chapter 2 originated with Dr. Shantanu Basu. I developed and implemented the numerical simulations. I ran these simulations on a local machine during a period of approximately four to six months during the Spring and Summer of 2013. I was responsible for the writing of the paper and preparation of all of the figures. Dr. Basu provided guidance toward preparation of the manuscript, and contributed to the writing of Section 2.4.

Drs. Eduard I. Vorobyov and Shantanu Basu developed the original idea for the work presented as Chapter 3. The numerical simulations were originally developed by Drs. Vorobyov and Basu (see Vorobyov & Basu 2006). I developed and implemented a subroutine for the chemistry of the code, making it suitable for the early universe. I also developed and implemented the subroutine that allows for the calculation of the protostellar accretion luminosity. I ran the simulations on SHARCNet over a period of roughly six months between Fall 2012 and Spring 2013. Dr. Vorobyov prepared the outline of the paper and aided in the analysis of the simulation results. He contributed to the writing of Section 3.2, all of sub-Section 3.3.1, and the clump analysis contained within sub-Section 3.3.2. His aid was also crucial to the preparation of the paper's figures. Dr. Basu contributed needed supervision and guidance for the preparation of the manuscript.

The idea for the work presented as Chapter 4 was developed by Dr. Shantanu Basu and myself. The numerical simulation code is the same as that used in Chapter 3. I ran a substantial number of additional numerical simulations on SHARCNet over a period of six months between the end of 2013 and Spring 2014. I was responsible for the writing of the paper and preparation of all of the figures. Dr. Basu contributed guidance toward preparation of the manuscript, and assisted in strengthening the presentation of the clustering scenario in Section 4.2, and contributed to the writing of Section 4.5.

Acknowledgements

For their role as both teachers and mentors, I convey my heartfelt appreciation to Drs. Shantanu Basu, Jan Cami, Sarah C. Gallagher, and Martin Houde. With doors always open, your trust in my abilities, together with your support and guidance, has allowed me to challenge the boundaries I create for myself, encouraging my growth academically and scientifically.

To my friends, as eternal antagonists and in your efforts to distract me from all of my goals, thank you. In particular, Konstantin Fedatov, Robbie Halonen, Scott Jones, Amy Orr, and Dave Stock. In your successes to that extent, and to all of their varying degrees, I have valued every moment of insightful discussion, laughter, and hijinks that we've shared together so far. I look forward to many-many more.

To my mother: Your unflinching strength as a person is a characteristic I continue to strive to emulate. You have always put me first, sometimes at great pain to yourself, and for this I am indebted to you, for the years of love and support you have given me, and which I can never repay. A mere acknowledgement fails to convey the depth of my gratitude.

To my sister, Amanda: Twenty-one years ago I unwrapped a simple department-store telescope that you gave to me as a Christmas present. Intentional or not, with that instrument you ignited in me the deep sense of wonder for the natural world that has allowed me to pursue this today, as I now prepare to earn a Doctorate of Philosophy in Astronomy. Your influence on my life has been nothing short of inspirational.

To Allison: You have shown me a tremendous amount of warmth, understanding, and care through what has sometimes been a difficult journey. I have come to love and depend on you for your humor when feeling bleak, your strength when feeling low, and your continued confidence and encouragement in and of me. I know that whatever my goals, with you by my side, they will never be that far out of reach.

Looking up at the stars, I know quite well
That, for all they care, I can go to hell,
But on earth indifference is the least
We have to dread from man or beast.

How should we like it were stars to burn
With a passion for us we could not return?
If equal affection cannot be,
Let the more loving one be me.

Admirer as I think I am
Of stars that do not give a damn,
I cannot, now I see them, say
I missed one terribly all day.

Were all stars to disappear or die,
I should learn to look at an empty sky
And feel its total dark sublime,
Though this might take me a little time.

—*The More Loving One*

W. H. Auden, 1957

Contents

Abstract	ii
Co-Authorship Statement	iii
Acknowledgements	iv
List of Figures	viii
List of Tables	x
1 Introduction	1
1.1 The Collapse of a Molecular Cloud	2
1.1.1 Fragmentation	3
1.1.2 The Angular Momentum Problem	4
1.2 The First Stars	6
1.2.1 Cosmogony	7
1.2.2 Formation of a First Star	10
1.3 Viscosity	10
1.4 Outlook	14
2 The $\dot{M} - M_*$ Correlation	21
2.1 Introduction	21
2.2 Disk Model	23
2.2.1 Viscous Evolution of an Axisymmetric Thin Disk	23
2.2.2 Viscosity	24
2.3 Results	27
2.3.1 Initial Conditions	27
2.3.2 Mass Accretion Rates	29
2.3.3 $\dot{M} - M_*$ Correlation	31
2.4 Summary & Discussion	34

3	Primordial Star Formation	42
3.1	Introduction	42
3.2	Model Description	43
3.3	Results	48
3.3.1	Cloud Core at the Onset of the Formation of the Central Protostar . . .	48
3.3.2	Formation and Evolution of a Primordial Disk	51
3.3.3	Accretion and Luminosity Bursts	58
3.3.4	Parameter space study	63
3.4	Discussion	65
3.5	Model Caveats	67
3.6	Conclusions	68
4	The Luminosity of Population III Star Clusters	72
4.1	Introduction	72
4.2	The Case for Population III Star Clusters	74
4.3	Individual Cluster Members	75
4.3.1	Numerical Simulations	75
4.3.2	Initial Conditions	76
4.3.3	Evolution of the Protostellar Disk	79
4.3.4	Accretion Luminosity	82
4.4	Clusters of Population III Protostars	85
4.5	Discussion & Conclusions	91
5	Conclusions	97
	Bibliography	100
A	Appendix A	110
B	Appendix B	112
	Curriculum Vitae	114

List of Figures

1.1	Images of Young Stellar Objects in the Orion Nebula	2
1.2	Geometry of the Classical Spherical Collapse Problem	6
1.3	Temperature Fluctuations from the Cosmic Microwave Background	7
1.4	Power Spectrum of Linearly Extrapolated RMS Fluctuations	9
1.5	Heating and Cooling Processes in Primordial Gas	11
1.6	Radial Profiles of the Collapse of a 1D Primordial Gas Cloud	12
1.7	Schematic of Angular Momentum Transport Processes	15
2.1	Disk Characteristics at $t = 0$ and 2×10^6 yr	28
2.2	Mass Accretion Rates in Disks Evolved with Q based Viscosity	30
2.3	Mass Accretion Rates in Disks Evolved with α Viscosity	31
2.4	Mass Accretion Rates versus Protostellar Mass (All Simulations)	32
2.5	Histogram of the Correlation Index of the $\dot{M} - M_*$ Relation	33
2.6	Simulated Measurements in the $\dot{M} - M_*$ -Plane	34
2.7	Comparison between Actual and Simulated Measurements in the $\dot{M} - M_*$ -Plane	35
2.8	p -values from Comparisons between Actual and Simulated Measurements . . .	36
3.1	Temperature Evolution of Zero-metallicity Gas	45
3.2	Comparison of Primordial Cloud Core Properties	49
3.3	Projection of the Gas Surface Density at $t = 800$ yr	50
3.4	Projections of the Gas Surface Density Over Time	50
3.5	Contour Maps of Gravitational Instability in the Disk	52
3.6	Number of Fragments in the Disk versus Time	53
3.7	Σ and Normalized- τ along Radial Cuts through the Disk	55
3.8	Tracking Fragments in the Disk in Time	56
3.9	Mass Accretion Rates, Mass Growth, and Accretion Luminosity in the Refer- ence Model	60
3.10	Mass Accretion Rate and Global Toomre Q	62
3.11	Parameter Space Study Effects on \dot{M} , M_* , and L_{acc}	64

4.1	Projection of the Disk Surface Density 1000 yr After Formation	77
4.2	Projections of the Disk Surface Density within a 2000×2000 AU Volume . . .	78
4.3	Mass Accretion Rates and Mass Growth in the Reference Model	81
4.4	Identifying Accretion Luminosity Bursts in the Reference Model	84
4.5	Accretion Luminosity of a $N = 2$ Member Cluster of First Stars	86
4.6	Normalized Accretion Luminosity for $N = 16$ and 128 Member Clusters	87
4.7	Mean Cluster Luminosity as a Function of Cluster Size N	89
4.8	Fractional Duration of Time a $N = 16$ Cluster Spends at Luminosities $> L$. .	90
4.9	Fractional Duration of Time Clusters of Size N Spend at Luminosities $> L$. .	90
A.1	Disk Aspect Ratio in the Thin-Disk Approximation	111

List of Tables

1.1	Parameters of the Concordance Λ CDM Cosmological Model	8
3.1	Parameters of the Barotropic Relation	46
3.2	Model Parameters	48
3.3	Fragment Characteristics	58

Chapter 1

Introduction

Stars are the single most fundamental units of luminous matter through which we are able to trace the formation and evolution of structure in the universe across cosmic time. Understanding how and where stars form is thus one of the most important problems in astrophysics. Despite this, the history of inquiry into this subject has been almost entirely confined to the modern era. The first intensive efforts into understanding star formation began with a paper by Jeans entitled *The Stability of a Spherical Nebula* (1902), wherein Jeans established how gravitational instability within an otherwise uniform density gas can lead to the onset of its collapse.

For decades however, the details of the star formation process remained obscured by the very environment in which stars formed: densely shrouded by infalling gas and dust. Prior to the 1980s almost all of what was known regarding the physics of star formation came from a handful of theoretical models. The first of these was arguably the work by Larson (1969) and Penston (1969) who independently developed numerical and analytical treatments for the gravitationally induced hydrodynamic collapse of spherical bodies.

Extended insights into the formation of stars and their disks arrived in the now seminal paper by Lynden-Bell & Pringle (1974). They posited that, as a result of the collapse of protostellar cloud cores, young stellar objects would be surrounded by large disks of gas and dust. In doing so Lynden-Bell & Pringle were able to successfully demonstrate that many of the characteristics of young stellar objects—variability in the infrared and ultraviolet parts of their spectrum, and the episodic flaring in the luminosity of T Tauri objects—could readily be accounted for in this new paradigm in which disks followed as a necessary outcome of the star formation process. Shu (1977) substantially expanded upon these ideas, developing a self-similar model for the collapse of a singular isothermal sphere into an identifiable protostellar object. But it was Terebey, Shu, & Cassen (1984) that finally developed the numerical simulations demonstrating these processes, including for the first time, the formation and evolution

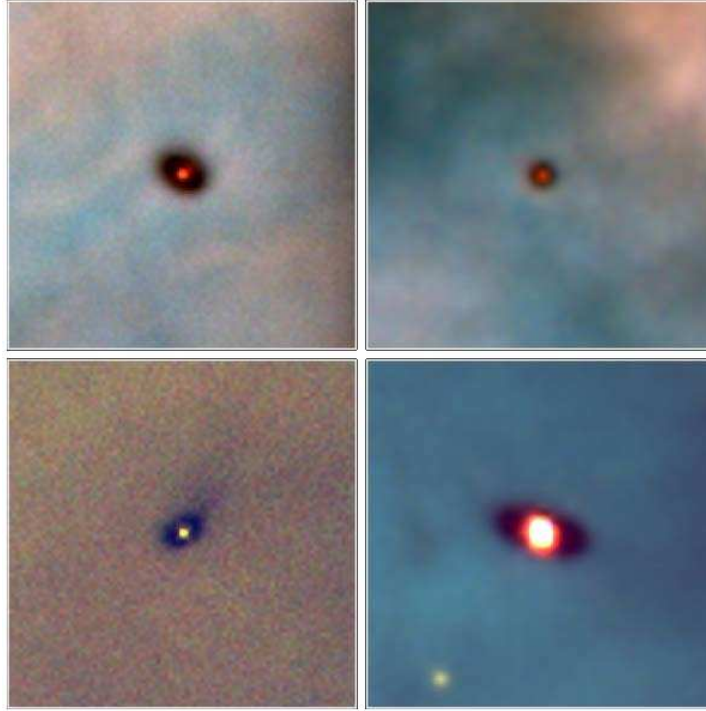


Figure 1.1: Composite emission line images of young stellar objects harboring disks from the Hubble Space Telescope survey of the Orion Nebula (McCaughrean & O’Dell, 1996). Radiation from [N II], [H α], and [O III] are respectively represented in red, blue, and green. The cooler material of the circumstellar disks are visible only as silhouettes around their host stars. The frequency of disks around protostars is estimated to be $> 90\%$.

of an accretion disk as a corollary of the star formation process.

With the benefit of increasingly sophisticated observational tools and numerical simulations, the formation of circumstellar disks is today understood as a crucial element of the star forming process: integral to the resolution of the so-called “angular momentum problem” (Section 1.1.2, below); allowing for the development of multi–star systems (e.g., Boss, 2001; Rice et al., 2003; Basu & Vorobyov, 2012); and acting as the nursery for later planetary formations (e.g., Boss, 1997; Chiang & Youdin, 2010). Understanding the formation and evolution of circumstellar disks therefore allows us to probe the physics of star forming processes on both micro- and macroscopic scales.

1.1 The Collapse of a Molecular Cloud

Stars form from the self-induced gravitational collapse of dense molecular clouds that are structured in a highly inhomogeneous way. The result is a hierarchy of size scales, as successively smaller portions of a cloud decouple from one another during the collapse process (e.g., Larson,

2003, and references therein). Giant molecular clouds are the largest coherent objects within this hierarchy, measuring hundreds of pc across and containing up to $10^6 M_\odot$ of material. However, they are still comparatively denser than the interstellar medium, at ~ 20 molecules per cm^3 compared to ~ 1 molecule per cm^3 in the interstellar medium. On the next level of scale, an enhancement in the density of a localized region within the cloud give rise to configurations of irregular and filamentary substructure, collectively referred to as clumps. Though these objects are often only a few pc in size, they can contain as much as $10^3 M_\odot$ of material. These clumps are often viewed as the progenitors of entire star clusters, and typically undergo additional sub-fragmentation, resulting in the production of several pre-stellar cores (Hartmann, 2009).

1.1.1 Fragmentation

We can best understand these successive stages of fragmentation in the context of the following simplified framework. Consider an isothermal, initially uniform gas with sound speed c_s , density ρ_0 , and pressure P ; such a region experiences no net pressure or gravitational force. A small compression perturbation within the background uniformity produces a local density enhancement within a radius λ , and correspondingly, an increase of the inward gravitational force. However, the compression of regions of a size λ greater than some critical value λ_J (known as the ‘‘Jeans length’’; Jeans, 1902) are likely to undergo further collapse as the gravitational force now exceeds the outward pressure of the gas. A detailed analysis (see Binney & Tremaine, 2008) of this physical argument reveals the critical length to be

$$\lambda_J = \left(\frac{\pi c_s^2}{G \rho_0} \right)^{1/2}. \quad (1.1)$$

Straightforwardly, we can derive an associated critical mass (the ‘‘Jeans mass’’) as well:

$$M_J = \rho_0 \lambda_J^3 = \left(\frac{\pi c_s^2}{G} \right)^{3/2} \rho_0^{-1/2}. \quad (1.2)$$

These quantities are often likewise related to the temperature of the gas as $c_s^2 = k_B T / \mu m_p$ —where k_B is Boltzmann’s constant; the mean molecular weight of the gas is $\mu \simeq 2.27$ (for a medium that is mostly H with a 24% admixture of He); m_p is the proton mass.

The Jeans criterion implies that as long as a region is optically thin (the condition for approximate isothermality), it will fragment. In the linear analysis of the gravitational instability in more complicated geometries, such as sheets and/or filaments, a preferred scale for fragmentation is found that is approximately equal to λ_J (Larson, 1985). Additionally, at number densities in excess of 10^{11} cm^{-3} the cloud gas will become largely opaque. As this happens,

rising temperatures will cause the Jeans length to again rise ($\lambda_J \propto T^{3/2}$), stabilizing a stellar core against further collapse.

Although cores are themselves occasionally classified into a number of related sub-categories (see review by André et al., 2009), they are most often regarded as the smallest scale progenitors for the formation of individual stars. This conclusion is substantiated by the comparison of cloud core surveys with even simple analytic arguments. In the limit that thermal gas pressure is the principal force opposing gravitational collapse, one can relate the core mass M_c and radius R_c to its temperature, which in hydrostatic equilibrium is

$$\frac{GM_c}{R_c} \simeq c_s^2 = \frac{k_B T}{\mu m_p}. \quad (1.3)$$

Assuming a standard gas constituency, $\mu = 2.27$, and a typical temperature of $T = 10$ K, a $1 M_\odot$ molecular cloud core would have a radius of $R_c = 0.1$ pc; an estimate relatively consistent with surveys of cloud cores in nearby star forming regions (the essential reference survey being Myers & Benson, 1983).

1.1.2 The Angular Momentum Problem

Once a hydrostatic core is established, continued accretion from the protostar's natal surroundings necessitates the formation of a circumstellar disk as a result of angular momentum conservation. Studies of the velocity gradients in nearby molecular clouds typically observe rotation rates of a few $\text{km s}^{-1} \text{pc}^{-1}$ (e.g., Goodman et al., 1993). Perfect angular momentum conservation during gravitational collapse would therefore require a typical star to have angular momentum several orders of magnitude larger than is possible for the star to maintain radial force balance (Bodenheimer, 1995). For example, an object's specific angular momentum (i.e., angular momentum per unit mass) is simply

$$j = r^2 \Omega. \quad (1.4)$$

An initial cloud core with a radius of $r = 0.1$ pc, containing $1 M_\odot$ of material, and rotating at a rate of $\Omega = 1 \text{ km s}^{-1} \text{pc}^{-1}$ possesses

$$j_c \simeq 2.7 \times 10^{21} \text{ cm}^2 \text{ s}^{-1}. \quad (1.5)$$

By comparison, the product of that core's collapse, a Sun-like star with radius $r = R_{\odot}$, and rotation rate $\Omega \sim 3 \times 10^{-6} \text{ s}^{-1}$), has

$$j_* \simeq 1.5 \times 10^{16} \text{ cm}^2 \text{ s}^{-1}. \quad (1.6)$$

The ratio of the specific angular momentum between the progenitor and its product is thus

$$\frac{j_c}{j_*} \sim 10^5.$$

Hence, the collapse of a molecular cloud into a young stellar object must also include some mechanism for dissipating the excess of angular momentum, while simultaneously ensuring that the majority of the mass of the system still ends up in the protostar.

Imagine instead that the initial configuration of the molecular cloud is that of an isotropic, spherical distribution of matter uniformly rotating around a centrally located gravitating point source (i.e., a protostar; see Figure 1.2). Material falling inward along the axis of rotation is able to do so unabatedly. However, material falling inward along axes of greater inclination θ (with respect to the axis of rotation) must overcome the centrifugal barrier imposed by the cloud's rotation. Instead of falling directly onto the protostar, this material falls inward to its respective minimum orbit, defined as the radius r at which the centripetal acceleration is equal to the gravitational attraction of the protostar:

$$\Omega^2 = \frac{GM_*}{r^3}. \quad (1.7)$$

Once in its minimum orbit, the material will fall parallel to the axis of rotation at this radius, where it impacts material following analogous trajectories in the symmetric hemisphere. These collisions give rise to the formation of a shock front along the equator of the cloud—a circumstellar disk is formed (Lodato, 2008).

Once nearly all of the angular momentum of a cloud has been dissipated, the multiplicity of a star systems or the presence of planets can account for the rest of the excess angular momentum. For example, Lada (2006) has shown that the probability for stars to form in multiples increases with mass, and therefore, with greater angular momentum in the parent cloud. Planetary systems can also take up some of the excess angular momentum. In our Solar System, the Sun contains 99% of the mass, but 99% of the angular momentum is contained within Jupiter and Saturn; with both of their orbits presumably within the centrifugal radius of the Solar Systems parent core (estimated to be ~ 15 AU; Basu, 1998). Hence, the present configuration of the Solar System is inherently a bi-product of the dissipation of angular momentum from the progenitor cloud core of our Sun.

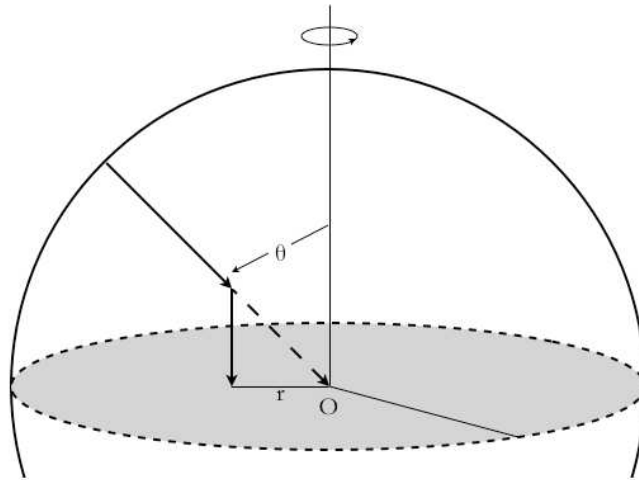


Figure 1.2: The geometry of the classical spherical collapse problem. Infalling material at an angle θ , with respect to the axis of rotation, is halted at a distance r , where the centripetal acceleration due to rotation of the cloud is balanced against the gravitational attraction of the protostar at O . Thereafter this material falls parallel to the rotation axis where it accumulates in a shock front along the equator of the cloud.

Clearly however we have neglected a great deal of the physics that accompanies the sort of collapse process described above. Heating of the gas can be induced through compression brought on by the gravitational collapse, as well as from the irradiation of material by the young stellar object. This is just one example of a process that can drastically alter the dynamics of the collapsing cloud (for thorough reviews on the dynamics of collapsing clouds see Larson, 2003; Hartmann, 2009). Nevertheless, the frequency with which disks are found as a collateral outcome of the star formation process suggests that they are the primary agent responsible for angular momentum and mass transport during the protostellar evolutionary phase (André et al., 2009).

1.2 The First Stars

The mass of a collapsing core is often regarded as a proxy indicator of the mass of the star being formed. But ultimately, the stellar mass will be a product of the interaction between a number of competing feedback processes that occur during the evolution of the collapse. A giant molecular cloud with an average density of 10^2 cm^{-3} collapsing into a protostellar object with a density of 10^{23} cm^{-3} is a problem spanning 21 orders of magnitude in density, 9 orders of magnitude spatially (from parsec scales to those of stellar radii), and 7 orders of magnitude in time (Hartmann, 2009). The additional presence of magnetic fields, chemistry involving metals

(i.e., elements heavier than lithium) and dust, and radiative processes, substantially complicate the physics of present-day star formation processes. From this perspective, understanding star formation in the early universe is a considerably more tractable problem owing to the absence of these complex interactions. The primordial environment also reflects nearly ideal conditions for the direct application of the Jeans criterion (equation [3.9] and [1.2]).

1.2.1 Cosmogony

The expansion of the universe (Hubble, 1929) presents immediate implications for the chronology of its evolution. If one imagines a reversal of the expansion, we realize that the density of the universe must have been higher in the past than it is today (and will be in the future). If we extrapolate far enough back, we arrive at a point in time at which the entirety of the universe itself must have been confined within an infinitesimal volume of infinite density; the moment of the so-called Big Bang (Lemaître, 1931). Relics from this hotter, denser time are detectable today via measurements of the abundances of the light elements (such as deuterium, helium, and lithium), and most notably from the cosmic microwave background (Figure 1.3; Penzias & Wilson, 1965; Dicke et al., 1965; Hinshaw et al., 2013, most recently).

But the universe we observe today bears little resemblance to its primordial infancy. Less than one billion years after the Big Bang, the universe had already evolved a myriad of hierarchical structures: stars, their remnants, and the progenitors of early galaxies. However, this transformation of the universe’s early homogeneity into such highly complex objects remains obscured from direct observation. This period of transition, during which the distribution of matter was still quite uniform and no luminous objects had yet formed, has come to be known as the “dark ages.”¹

The Λ CDM model of the universe— Λ , referring to the cosmological constant, manifested as dark energy; CDM, to the presence of cold dark matter—is the most coherent framework developed to date that successfully accommodates nearly all cosmological observations (a thorough review of the theory underpinning this paradigm has recently been provided by Frieman et al., 2008). Surveys of galaxy clustering (e.g., Cole et al., 2005) and high redshift supernovae (Perlmutter et al., 1998; Riess et al., 1998, 2004) confirm the existence of the so-called exotic components, dark matter and dark energy.

The existence of dark matter in particular, is also a requirement for explaining how fluctuations in the intensity of the CMB acted as the loci around which large-scale structure formed; galaxies, and the clusters of them, that are observable in the present-day (Davis et al., 1985; Springel et al., 2005). Prior to the era of recombination, strong coupling between the back-

¹Coined for cosmological use by Martin Rees in Tozzi et al. (2000).

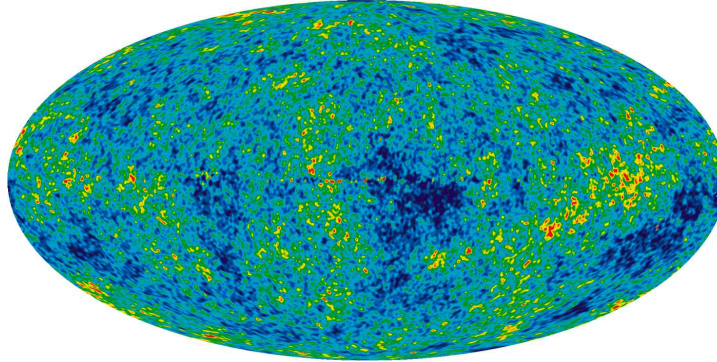


Figure 1.3: All-sky image of the temperature fluctuations (red identifying warm regions; blue, cool) of the primordial gas from a redshift of $z \sim 1100$. The amplitude of the variations correspond to $\pm 200 \mu\text{K}$, demonstrating the extreme isotropic homogeneity of the gas in the early universe (image credit: NASA/WMAP Science Team).

Table 1.1: Parameters of the Concordance ΛCDM Cosmological Model

Ω_b	Ω_m	Ω_Λ	h_0	n_s	σ_8
0.0464	0.281	0.719	0.697	0.971	0.820

Table 1.1: The values of Ω specify the ratios of the baryon density (subscript-b), total matter density (-m), and contribution from dark energy (- Λ) to the critical density of the universe. h_0 is the dimensionless Hubble parameter ($H_0 = 100 h_0 \text{ km/s/Mpc}$). n_s is the power-law index associated with the power spectrum of primordial density fluctuations. $\sigma_8 = \sigma(R = 8 h_0^{-1})$ is the normalization of the corresponding power spectrum at $z = 0$ (Hinshaw et al., 2013).

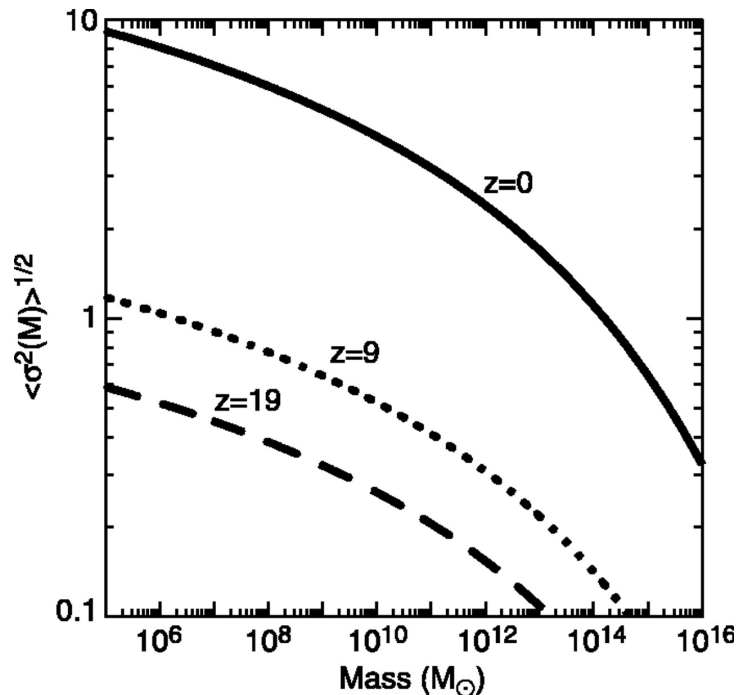


Figure 1.4: Amplitude of density fluctuations $\sigma(M)$ (in units of M_{\odot}) at different redshifts z . Dark matter halos form in regions that exceed the background density by a factor of order unity. This threshold is surpassed only by rare (many- σ) peaks for high masses at high redshifts (figure from Miralda-Escudé, 2003).

ground radiation of the CMB and baryonic matter would have quickly smoothed variations in density field to the same temperature (as in Figure 1.3). But collisionless, non-interacting (i.e., cold) dark matter particles would not have been subjected to such smoothing. By the time of recombination (redshift $z \sim 1100$), whatever small perturbations that had existed within the initial density field of the dark matter thus became amplified. The resulting morphology presented itself as a kind of scaffolding upon which future higher-order structure would be built.

The power spectrum of these fluctuations can be represented in terms of the root mean square fluctuations of a mass, δM , enclosed by a sphere of radius R (its volume times the mean density of the universe produces on average a mass M). The linearly extrapolated fluctuations, $\delta M/M$, are shown in Figure 1.4 as a function of M . These grow in proportion to the scale factor, as $(1+z)^{-1}$, during the era of matter domination; up to $z \lesssim 1$, at which point dark energy begins to suppress further growth (Loeb, 2010). At the present time, fluctuations are typically of order unity on scales containing masses of $\sim 10^{14} M_{\odot}$, corresponding to mass found in a typical galaxy cluster. At the time at which the first stars were beginning to form, $z = 9$, typical fluctuations collapsed on much smaller scales of $M \sim 10^6 M_{\odot}$.

The first stars are thus predicted to form in dark matter minihalos of mass $\sim 10^6 M_{\odot}$ at a

redshift of $z \sim 20 - 50$ (e.g., Couchman & Rees, 1986). The virial temperature in these low-mass halos is below the threshold $\sim 10^4$ K that is required for efficient cooling of the gas by atomic hydrogen. Molecular hydrogen (H_2) is therefore the coolant of choice during this epoch (Bromm & Larson, 2004, and references therein). These theoretical predictions of the masses of dark matter halos, and their associated virialization temperatures, underlie the framework for the discussion to follow, of the end of the dark ages, and the formation of the first stars.

1.2.2 Formation of a First Star

Within this cosmological framework, although the dark matter is likely to be in virial equilibrium by this point, it is expected that the gas will continue to collapse, eventually forming a protostar with an initial mass of roughly $5 \times 10^{-3} M_\odot$ (Yoshida et al., 2008). Initially the primordial gas is unable to cool efficiently because the atoms in its constituency have excitation energies that are too high, and those molecules that do have accessible rotational energies are very rare. The formation of molecular hydrogen through the pathway $\text{H} + e^- \rightarrow \text{H}^- + \gamma$, followed by $\text{H}^- + \text{H} \rightarrow \text{H}_2 + e^-$, is eventually able to cool the gas down from temperatures of roughly 1000 K to that of a order 100 K (e.g., Abel et al., 2002; Bromm et al., 2002). However, this state is prohibitive against further collapse at temperatures less than 100 K, due to the lack of additional cooling mechanisms in the primordial environment (Figure 1.5). At this point, the clump is forced to enter into a state of quasi-equilibrium. But the gradual accumulation of additional material within the dark matter potential eventually drives the system toward runaway gravitational collapse, in accordance with the Jeans criterion (Clarke & Bromm, 2003),

$$M_J \sim 400 M_\odot \left(\frac{T}{300 \text{ K}} \right)^{3/2} \left(\frac{n}{10^5 \text{ cm}^{-3}} \right)^{-1/2}. \quad (1.8)$$

The aforementioned groups of Abel and Bromm have independently constructed large-scale simulations of the collapse of primordial gas clouds. Though beginning from similar initial conditions, their simulations predict somewhat different mass outcomes for the first stars. Abel et al. (2000, 2002) argue that Population III stars are formed in relative isolation, one star per dark matter minihalo. Assuming that the subsequent accretion lasts only as long as the lifetime of a very massive star, their simulations produce an upper limit of approximately $500 M_\odot$ for the first stars. Bromm et al. (2002) instead argue for the sub-fragmentation of clumps, producing small clusters of between 1 and 5 stars. However, both of these approaches possess neither the requisite mass- nor time-resolution required to accurately follow subsequent clump collapse to actual protostellar densities; stopping at $n \sim 10^8 \text{ cm}^{-3}$, several orders of magnitude before the $n \sim 10^{22} \text{ cm}^{-3}$ density characteristic of a hydrostatic core.

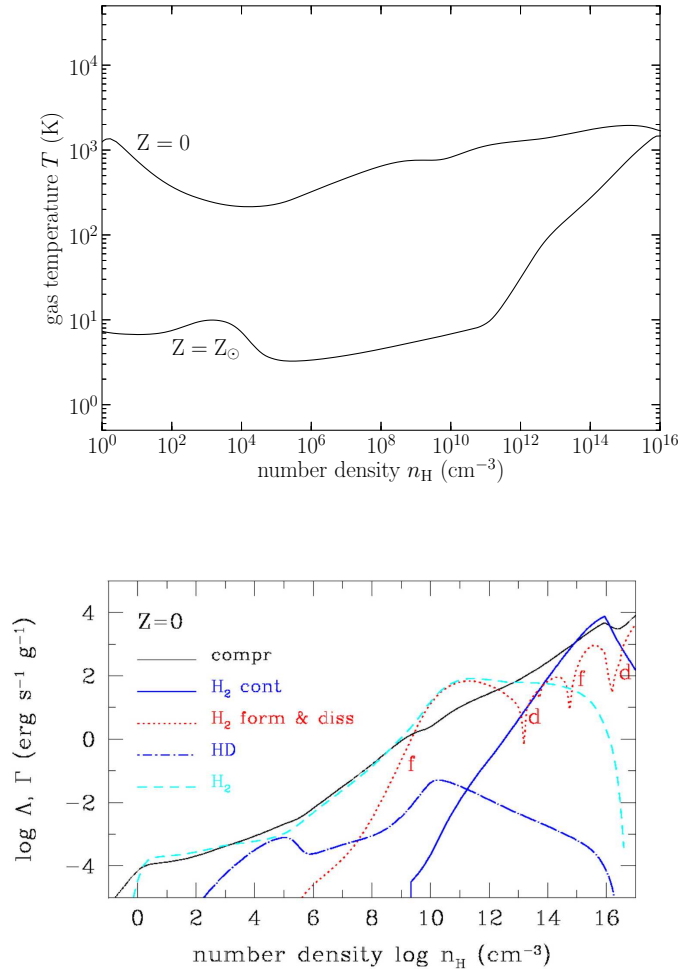


Figure 1.5: **Top:** Temperature evolution as a function of number density in gas with metallicity $Z = 0$ and Z_\odot , as labelled. **Bottom:** Energy balance diagram indicating the total heating (Λ) and cooling rates (Γ) from each process in primordial gas, i.e., with metallicity $Z = 0$. The black line, labelled “compr”, indicates compressional heating. The blue line, labelled “ H_2 cont” indicates cooling via collisionally-induced emission. The red dotted line, “ H_2 form & diss”, indicates heating due to H_2 formation (labelled f in the figure) and cooling due to dissociation (d). “HD” and “ H_2 ” (the blue dot-dashed and cyan dashed lines, respectively) trace the line-emission cooling rates due to those specific species. These individual curves produce $Z = 0$ that appears in the top panel. Adapted from Omukai et al. (2005).

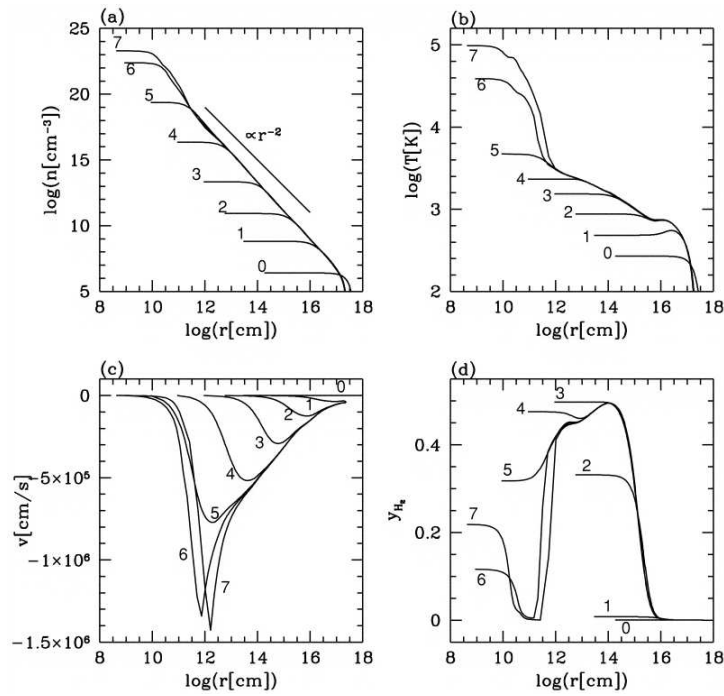


Figure 1.6: An example of an early one-dimensional simulation of the collapse of a primordial gas cloud, with time progressing as labeled, from 1 to 7. The panels depict (a) number density, (b) temperature, (c) velocity, and (d) H_2 abundance, as a function of radial distance. Curve 6 corresponds roughly to the formation of a central hydrostatic core (adapted from Omukai & Nishi, 1998).

1.3 Viscosity

Inevitably, the final mass of any star—primordial or otherwise—depends upon how efficiently accretion mechanisms are able to incorporate the clump mass into the growing protostar. As we have discussed, the role of the circumstellar disk in the redistributive transport of angular momentum is a crucial element of the star forming process. Many mechanisms have been proposed for angular momentum transfer in collapsing cloud cores, as well as in the late stages of the evolution once a protostar and its disk have been formed. Shakura and Sunyaev proposed early on (1973) that viscous dissipation in a differentially-rotating disk can affect angular momentum redistribution. However, the microphysical origin of this viscosity remains unknown. Classical mechanical viscosity is orders of magnitude too small to account for the observed mass accretion rates. In absence of a physical model, the viscosity is most often parameterized mathematically simply as some α (Shakura & Sunyaev, 1973); its value provided by the accretion rates deduced from observations of young stellar objects that it was purported to explain.

A natural source of viscosity in any fluid motion is the so-called molecular viscosity that arises as a result of the random motions of the particles that constitute the fluid,

$$\nu = \ell v, \quad (1.9)$$

where ℓ is the typical mean free path of a fluid particle, and v is a characteristic peculiar velocity. A circumstellar disk having an extent of $r \sim 10^{14}$ cm might typically be composed of particles having velocities on the order of $v \sim 10^5$ cm s⁻¹, and a mean free path as large as $\ell \sim 10^{10}$ cm. In this scenario the time scale for the viscous evolution of the system would be greater than the age of the universe (Bodenheimer et al., 2007).

It stands to reason that there must be a source of anomalous viscosity, one or more physical mechanisms that give rise to turbulence in an analogous manner, acting on much shorter time scales. Turbulent convection (Lin & Papaloizou, 1980) is one such mechanism, however more recent studies suggest that convection may actually be more efficient at transporting angular momentum inward, rather than outward (e.g. Stone & Balbus, 1996). By far the most popular methods today invoke an α -parameterization (Shakura & Sunyaev, 1973) of one or more actions that could be responsible for viscosity:

$$\nu = \alpha c_s H, \quad (1.10)$$

in which c_s is the sound speed of the disk medium, and H is the disk half-thickness; the value of α thus regulates the efficacy of the viscous action. It is generally believed that the length scale of turbulence within the disk will be less than the scale height, and that the velocity of

eddies will not exceed the sound speed. By tuning $\alpha \leq 1$ the detailed theory of viscous stress within the disk is parameterized. Thorough reviews of the α -model of viscosity can be found in Balbus & Hawley (1998), and more recently Lodato (2008).

However, protoplanetary disks are so cold and dense that thermal processes are unable to sufficiently ionize the disk material to levels required to support magnetohydrodynamic turbulence (Blaes & Balbus, 1994). In these scenarios the growth of gravitational instabilities brought on by the disk's self-gravity may act as the dominant mechanism through which angular momentum transport is possible. The schematic of Figure 1.7 illustrates the essential characteristics of angular momentum transport through both magnetorotational and gravitational instability.

One possible physical mechanism for the dissipation of angular momentum in disks is the action of self-gravity owing to gravitational torques that act between nonaxisymmetric structures within the disk. A parcel of gas that moves radially outward will experience a decrease in its orbital velocity with respect to its velocity in its equilibrium orbit. However, gravity can bind this parcel to other parcels of gas that remain in the equilibrium orbit. Complimentarily, these equilibrium parcels will be retarded, losing centrifugal support, and move inward into a lower orbit. At the same time, the originally-displaced parcel will be accelerated by this motion, causing yet again an increase in its angular velocity, causing it to move outward yet again. Differential rotation within the disk clearly exacerbates this problem and leads to angular momentum transport from the inner parcel to the outer one. This effectively constitutes a torque on the cloud.

In the local universe magnetic fields act to provide outward support against gravitational collapse. Coupling between the magnetic field and the gas and dust of the collapse medium strengthens the field, and thus the degree of support, as a region within a molecular cloud collapses. This leads to the so-called magnetic braking catastrophe, in which runaway collapse of the protostellar core enhances the local magnetic field (Basu & Mouschovias, 1994). If the collapse proceeds unabatedly, the emerging star would contain 10^3 to 10^5 times more magnetic flux than is typically observed among protostars. It has been shown that this effect can be so drastic as to suppress the formation of large scale disks entirely (Allen et al., 2003; Mellon & Li, 2008; Hennebelle & Fromang, 2008). In reality, several mechanisms—ambipolar diffusion and Ohmic dissipation (e.g., Nakano et al., 2002; Dapp & Basu, 2010; Dapp et al., 2012)—allow for the dissipation of magnetic flux.

For two reasons we ignore the effects of magnetic fields in our models. First, the disks we consider in Chapter 2 are established disks around protostars that are already 1 to 2 Myr in age. Secondly, in the case of the first stars, significant magnetic fields are thought to originate in the aftermath of the supernovae of the first stars as the motion of charged particles in the

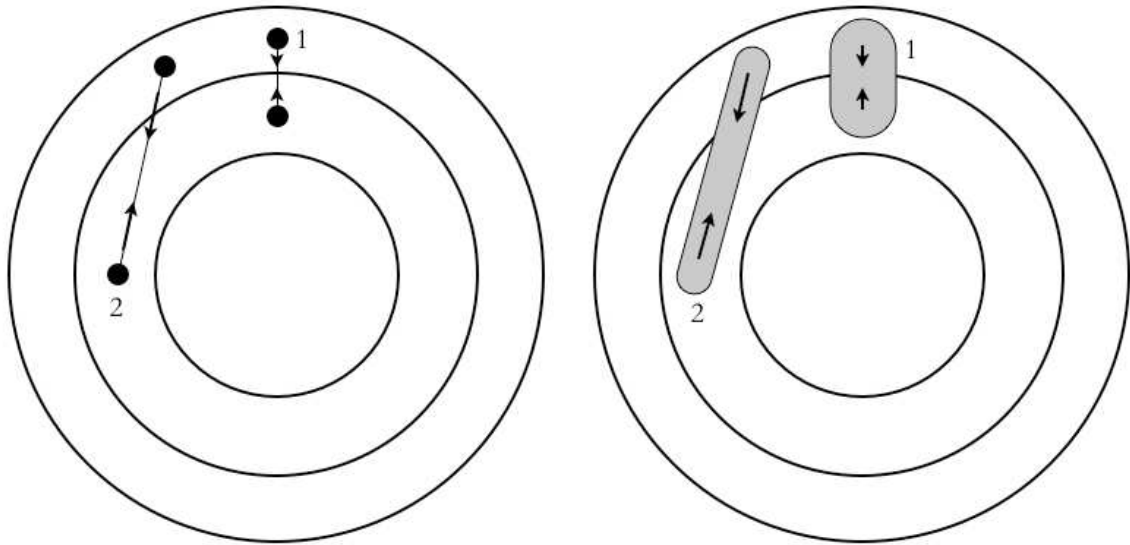


Figure 1.7: Schematic of angular momentum transport processes in viscous accretion disks (the disks depicted here rotate counter-clockwise). The panel at left depicts the effects of magnetorotational instability. Two parcels of fluid in adjacent annuli are connected together by a magnetic field line. As a result of the shearing caused by the parcels having different angular velocities, the field line connecting them at time t_1 is stretched at a later time t_2 . The resulting tension in the field line thus works to accelerate the outer parcel while simultaneously decelerating the interior parcel. In this manner the two parcels of gas respectively gain and lose angular momentum: the outer parcel carries a larger fraction of the system's angular momentum outward, while the inner parcel transports matter inward. The panel on the right-hand side depicts the analogous process mediated by gravitational instability. In this case the gravitational attraction across a slab of material conjoining two adjacent annuli serves as a restoring force when the material is sheared by the differential rotation of the two annuli. Adopted from Hartmann (2009).

supernovae ejecta give rise to small order fields that eventually align and grow (e.g., Pudritz & Silk, 1989). Hence the formation of the very first stars is believed to take place in a truly pristine environment in which no significant magnetic fields even yet exist (e.g., Turner & Widrow, 1988).

1.4 Outlook

The ubiquity of disks as the outcome of the protostellar collapse process makes them important targets of study to further our understanding of both the micro- and macroscopic physics that are responsible for the formation of stars. In this work we investigate some of the observational signatures of young stellar objects, linking their (mass) growth to the significance of self-gravity in mediating the formation and early evolution of stars. In Chapter 2 we construct a semi-analytic model to study the late-time (i.e., protostars with ages of a few Myr) quasi-steady state evolution of viscous circumstellar disks around young stellar objects. We employ these models to explain the long-standing correlation between these objects' mass and their observed rates of accretion. In Chapter 3 we shift our focus to the formation of the first stars in the universe—Population III stars. Employing a more sophisticated 2+1D model (two spatial dimensions in \hat{r} and $\hat{\phi}$ polar coordinates, plus a synthesized vertical structure along \hat{z}) we show that the first stars too must have harbored massive circumstellar disks analogous to those around stars forming in the present-day. Episodic gravitational-instability-induced fragmentation and accretion gives rise to a primordial burst mode of accretion, analogous to that experienced by protostars in the early universe (e.g., Vorobyov & Basu, 2006, 2010). This burst mode is the primary accretion channel through which the first stars incorporate material from their surroundings, with $\sim 30\%$ of their final mass stemming from the episodic accretion of material in this way. In Chapter 4 we consider the formation of clusters of Population III stars and calculate their luminosity. The importance of the primordial burst mode of accretion becomes most evident in this analysis, wherein we show that individual accretion events produce luminous bursts on the order of $10^{6-7} L_{\odot}$. From this we predict that aggregates of Population III protostars in clustered environments could allow for particularly luminous events in excess of $10^8 L_{\odot}$. The existence of the primordial burst mode of accretion therefore permits observational access to primordial star formation even in the event that the first stars are significantly less massive than previously thought (Hosokawa et al., 2011). Finally, Chapter 5 summarizes these findings and highlights those lingering questions that remain for future research.

Bibliography

Abel, T., Bryan, G. L., & Norman, M. L. 2000, *ApJ*, 540, 39

—. 2002, *Science*, 295, 93

Allen, A., Li, Z.-Y., & Shu, F. H. 2003, *ApJ*, 599, 363

André, P., Basu, S., & Inutsuka, S. 2009, in *Structure Formation in Astrophysics*, ed. G. Chabrier (Cambridge University Press)

Balbus, S. A. & Hawley, J. F. 1998, *Reviews of Modern Physics*, 70, 1

Basu, S. 1998, *ApJ*, 509, 229

Basu, S. & Mouschovias, T. C. 1994, *ApJ*, 432, 720

Basu, S. & Vorobyov, E. I. 2012, *ApJ*, 750, 30

Binney, J. & Tremaine, S. 2008, *Galactic Dynamics* (Princeton University Press)

Blaes, O. M. & Balbus, S. A. 1994, *ApJ*, 421, 163

Bodenheimer, P. 1995, *ARA&A*, 33, 199

Bodenheimer, P., Laughlin, G. P., Różyczka, M., & Yorke, H. W. 2007, *Numerical Methods in Astrophysics: An Introduction* (Taylor & Francis Group)

Boss, A. P. 1997, *Science*, 276, 1836

—. 2001, *ApJ*, 563, 367

Bromm, V., Coppi, P. S., & Larson, R. B. 2002, *ApJ*, 564, 23

Bromm, V. & Larson, R. B. 2004, *ARA&A*, 42, 79

Chiang, E. & Youdin, A. N. 2010, *AREPS*, 38, 493

- Clarke, C. J. & Bromm, V. 2003, MNRAS, 343, 1224
- Cole, S., Percival, W. J., Peacock, J. A., Norberg, P., Baugh, C. M., Frenk, C. S., Baldry, I., Bland-Hawthorn, J., Bridges, T., Cannon, R., Colless, M., Collins, C., Couch, W., Cross, N. J. G., Dalton, G., Eke, V. R., De Propris, R., Driver, S. P., Efstathiou, G., Ellis, R. S., Glazebrook, K., Jackson, C., Jenkins, A., Lahav, O., Lewis, I., Lumsden, S., Maddox, S., Madgwick, D., Peterson, B. A., Sutherland, W., & Taylor, K. 2005, MNRAS, 362, 505
- Couchman, H. M. P. & Rees, M. J. 1986, MNRAS, 221, 53
- Dapp, W. B. & Basu, S. 2010, A&A, 521, L56
- Dapp, W. B., Basu, S., & Kunz, M. W. 2012, A&A, 541, A35
- Davis, M., Efstathiou, G., Frenk, C. S., & White, S. D. M. 1985, ApJ, 292, 371
- Dicke, R. H., Peebles, P. J. E., Roll, P. G., & Wilkinson, D. T. 1965, ApJ, 142, 414
- Frieman, J. A., Turner, M. S., & Huterer, D. 2008, ARA&A, 46, 385
- Goodman, A. A., Benson, P. J., Fuller, G. A., & Myers, P. C. 1993, ApJ, 406, 528
- Hartmann, L. 2009, *Accretion Processes in Star Formation* (Cambridge University Press)
- Hennebelle, P. & Fromang, S. 2008, A&A, 477, 9
- Hinshaw, G., Larson, D., Komatsu, E., Spergel, D. N., Bennett, C. L., Dunkley, J., Nolta, M. R., Halpern, M., Hill, R. S., Odegard, N., Page, L., Smith, K. M., Weiland, J. L., Gold, B., Jarosik, N., Kogut, A., Limon, M., Meyer, S. S., Tucker, G. S., Wollack, E., & Wright, E. L. 2013, ApJS, 208, 19
- Hosokawa, T., Omukai, K., Yoshida, N., & Yorke, H. W. 2011, Science, 334, 1250
- Hubble, E. 1929, PNAS, 15, 168
- Jeans, J. H. 1902, Royal Society of London Philosophical Transactions Series A, 199, 1
- Lada, C. J. 2006, ApJL, 640, L63
- Larson, R. B. 1969, MNRAS, 145, 271
- . 1985, MNRAS, 214, 379
- . 2003, Reports on Progress in Physics, 66, 1651

- Lemaître, A. G. 1931, *Nature*, 128, 704
- Lin, D. N. C. & Papaloizou, J. 1980, *MNRAS*, 191, 37
- Lodato, G. 2008, *NAR*, 52, 21
- Loeb, A. 2010, *How Did the First Stars and Galaxies Form* (Princeton University Press)
- Lynden-Bell, D. & Pringle, J. E. 1974, *MNRAS*, 168, 603
- McCaughrean, M. J. & O'Dell, C. R. 1996, *AJ*, 111, 1977
- Mellon, R. R. & Li, Z.-Y. 2008, *ApJ*, 681, 1356
- Miralda-Escudé, J. 2003, *Science*, 300, 1904
- Myers, P. C. & Benson, P. J. 1983, *ApJ*, 266, 309
- Nakano, T., Nishi, R., & Umebayashi, T. 2002, *ApJ*, 573, 199
- Omukai, K. & Nishi, R. 1998, *ApJ*, 508, 141
- Omukai, K., Tsuribe, T., Schneider, R., & Ferrara, A. 2005, *ApJ*, 626, 627
- Penston, M. V. 1969, *MNRAS*, 144, 425
- Penzias, A. A. & Wilson, R. W. 1965, *ApJ*, 142, 419
- Perlmutter, S., Aldering, G., della Valle, M., Deustua, S., Ellis, R. S., Fabbro, S., Fruchter, A., Goldhaber, G., Groom, D. E., Hook, I. M., Kim, A. G., Kim, M. Y., Knop, R. A., Lidman, C., McMahon, R. G., Nugent, P., Pain, R., Panagia, N., Pennypacker, C. R., Ruiz-Lapuente, P., Schaefer, B., & Walton, N. 1998, *Nature*, 391, 51
- Pudritz, R. E. & Silk, J. 1989, *ApJ*, 342, 650
- Rice, W. K. M., Armitage, P. J., Bate, M. R., & Bonnell, I. A. 2003, *MNRAS*, 339, 1025
- Riess, A. G., Filippenko, A. V., Challis, P., Clocchiatti, A., Diercks, A., Garnavich, P. M., Gilliland, R. L., Hogan, C. J., Jha, S., Kirshner, R. P., Leibundgut, B., Phillips, M. M., Reiss, D., Schmidt, B. P., Schommer, R. A., Smith, R. C., Spyromilio, J., Stubbs, C., Suntzeff, N. B., & Tonry, J. 1998, *AJ*, 116, 1009

- Riess, A. G., Strolger, L.-G., Tonry, J., Casertano, S., Ferguson, H. C., Mobasher, B., Challis, P., Filippenko, A. V., Jha, S., Li, W., Chornock, R., Kirshner, R. P., Leibundgut, B., Dickinson, M., Livio, M., Giavalisco, M., Steidel, C. C., Benítez, T., & Tsvetanov, Z. 2004, *ApJ*, 607, 665
- Shakura, N. I. & Sunyaev, R. A. 1973, *A&A*, 24, 337
- Shu, F. H. 1977, *ApJ*, 214, 488
- Springel, V., White, S. D. M., Jenkins, A., Frenk, C. S., Yoshida, N., Gao, L., Navarro, J., Thacker, R., Croton, D., Helly, J., Peacock, J. A., Cole, S., Thomas, P., Couchman, H., Evrard, A., Colberg, J., & Pearce, F. 2005, *Nature*, 435, 629
- Stone, J. M. & Balbus, S. A. 1996, *ApJ*, 464, 364
- Terebey, S., Shu, F. H., & Cassen, P. 1984, *ApJ*, 286, 529
- Tozzi, P., Madau, P., Meiksin, A., & Rees, M. J. 2000, *ApJ*, 528, 597
- Turner, M. S. & Widrow, L. M. 1988, *Phys. Rev. D*, 37, 2743
- Vorobyov, E. I. & Basu, S. 2006, *ApJ*, 650, 956
- . 2010, *ApJ*, 719, 1896
- Yoshida, N., Omukai, K., & Hernquist, L. 2008, *Science*, 321, 669

Chapter 2

The Role of Angular Momentum Transport in Establishing the Accretion Rate–Protostellar Mass Correlation

A version of this chapter has been submitted for publication to New Astronomy.

2.1 Introduction

Protostellar disks are a ubiquitous outcome of the rotating collapse of dense molecular cloud cores in the standard paradigm of low-mass star formation (e.g., Terebey et al., 1984; Shu et al., 1987). Their existence has been confirmed around young stellar objects across a broad range in mass—from objects in the brown dwarf regime, to those with masses of up to $2\text{--}3 M_{\odot}$ (e.g., Beckwith et al., 1990; Andrews & Williams, 2005)—as well as in a wide variety of star forming environments (e.g., Lada & Wilking, 1984; O’Dell & Wen, 1994; McCaughrean & O’Dell, 1996).

Numerical simulations of collapsing cloud cores reveal that disks can form within $\sim 10^4$ yr from the onset of core collapse (Yorke et al., 1993; Hueso & Guillot, 2005). These early so-called Class 0 systems are difficult to study observationally as they are still embedded within their progenitor cloud cores (André et al., 1993). Numerical simulations (e.g., Vorobyov & Basu, 2005b, 2006, 2010) suggest that the earliest periods (~ 0.5 Myr) of disk formation are rather tumultuous, as infall from the parent cloud core induces gravitational instability–driven mass accretion. Depletion of the gas reservoir by this mechanism then gives way to a much more quiescent period of accretion in which gravitational torques act to transport mass inward while transporting angular momentum outward (Gammie, 2001; Lodato & Rice, 2004;

Vorobyov & Basu, 2007). Indeed, the subsequent Class I and II phases are respectively marked by a decline in the rate of accretion from the surrounding natal environment, and its eventual cessation (Vorobyov & Basu, 2005a). Hence, it is during the Class II phase, once the central star is optically visible, that the disk properties are most easily amenable to observational investigation.

One result to emerge from observational studies of young stellar objects and their disks is the correlation between protostellar mass M_* and the inferred accretion rate \dot{M} from the disk, for which the power law exponent is typically estimated to be $\beta \sim 1.5\text{--}2.0$ (e.g., Muzerolle et al., 2005; Herczeg & Hillenbrand, 2008; Rigliaco et al., 2011). Although this correlation appears to hold across multiple orders of magnitude in both M_* and \dot{M} , fitting the accretion rates of brown dwarfs and T Tauri stars together may be misleading. In the brown dwarf regime, as well as for low mass T Tauri stars (i.e., those objects with mass $M_* < 0.2 M_\odot$), a least squares fit yields $\beta = 2.3 \pm 0.6$. For intermediate and upper mass T Tauri stars ($M_* > 0.2 M_\odot$), the equivalent fit yields a value for β of 1.3 ± 0.3 ; suggestive that different physical mechanisms may be responsible for accretion across the sequence of protostellar masses (Vorobyov & Basu, 2008).

Studies by Alexander & Armitage (2006) and Hartmann et al. (2006) have sought to explain the $\dot{M}\text{--}M_*$ scaling in the context of viscous models for the disk evolution, wherein the turbulent viscosity has ad hoc spatial dependence of the form $\nu \propto r^\xi$. Dullemond et al. (2006) link the disk evolution to the properties of the parent cloud core, providing a self-consistent basis for the results of their study. However, their models require that the ratio of rotational to gravitational energy be uniform across all cloud core masses. Rice & Armitage (2009) have even attempted to (weakly) incorporate the additional effects of magnetic fields (in high temperature regions of the disk) in quasi-steady state models, but were also unable to fully account for the observed correlation.

In this paper we present a study of the quasi-steady state evolution of viscous circumstellar disks surrounding young stellar objects, following the cessation of mass accretion onto the protostar-disk system (definitively Class II objects). These disks inherit initial conditions roughly consistent with the results of numerical simulations of the earlier burst phase (e.g., Vorobyov & Basu, 2005b, 2006, 2010), and undergo diffusive evolution wherein angular momentum redistribution is driven by self-gravity, which we parameterize in terms of an effective kinematic viscosity (following Lin & Pringle, 1987). We add to this a simplified argument for angular momentum conservation that correlates disk size with protostellar mass at the start of our simulations. With these assumptions, we are able to reproduce many features of the observed correlation between \dot{M} and M_* for young protostellar systems.

Ultimately we seek to characterize the global behavior of the mass transport within the disk

through the action of gravitational torques, in the same spirit as the models of e.g., Armitage et al. (2001) and Zhu et al. (2009, 2010). Other accretion mechanisms may be necessary in the innermost sub-AU regions of the disk, possibly introducing short-term time variability. The above studies typically invoke the magnetorotational instability (Balbus & Hawley, 1991) as the transport mechanism in the hot inner disk, however it is worthwhile to keep in mind that the region 0.1–1.0 AU from the star is generally thought to be the outflow driving zone (e.g., Garcia et al., 2001; Krasnopolsky et al., 2003) from which significant amounts of angular momentum and mass are carried away from the disk.

2.2 Disk Model

We construct a model for the temporal evolution of self-gravitating, axisymmetric thin disks on a radial grid with logarithmic spacing, and consisting of $N = 256$ annular elements. Discretization of the radial grid allows us to write the relevant partial differential equations as sets of ordinary differential equations, with one equation for each coordinate position in r . The spatial derivatives are approximated using second-order accurate central differencing. Integration of the system through time is handled using a variable order Adams-Bashforth-Moulton solver (e.g., Shampine, 1994).

2.2.1 Viscous Evolution of an Axisymmetric Thin Disk

Combining together the fluid equations for mass and momentum conservation yields a diffusion-like equation that governs the temporal evolution of the disk surface mass density $\Sigma(r, t)$ (e.g., Lynden-Bell & Pringle, 1974; Pringle, 1981):

$$\frac{\partial \Sigma}{\partial t} = -\frac{1}{r} \frac{\partial}{\partial r} \left[\left(\frac{\partial}{\partial r} r^2 \Omega \right)^{-1} \frac{\partial}{\partial r} \left(\nu r^3 \Sigma \frac{\partial \Omega}{\partial r} \right) \right], \quad (2.1)$$

where $\Omega(r, t)$ is the disk angular frequency (obtained assuming centrifugal balance), and ν is the effective kinematic viscosity (detailed in Section 2.2.2).

A precise determination of Ω requires a thorough accounting of the contribution to the gravitational potential made by the disk itself, which can be calculated explicitly using the elliptic integral of the first kind (e.g., Binney & Tremaine, 2008). However, the central point-mass dominates the system's gravitational potential, with the contribution from the disk increasing Ω only slightly. For the sake of computational convenience we thus adopt a simplified proce-

dure by approximating the total gravitating mass at a radius r to be

$$M(r, t) = M_*(t) + 2\pi \int_{r_{\text{in}}}^r \Sigma r' dr', \quad (2.2)$$

in which r_{in} denotes the innermost radius of the simulation domain (and the assumed disk inner edge).

The action of (2.1) is to transport material within the disk to ever smaller radii, while a small fraction of disk material is simultaneously transported to larger radii, thereby preserving the system's total angular momentum. For these simulations, the disk edge r_{edge} is always $\ll r_{\text{out}}$, the computational domain's outer boundary. Thus, material that exits the simulation can only do so through r_{in} . We impose a free inflow boundary condition there, and any material crossing r_{in} is assumed to be accreted onto the central protostar, which we model as a point mass.

2.2.2 Viscosity

Temporal evolution of the disk is governed by the viscous stresses acting on the disk material. These stresses are typically subsumed into a dimensionless parameter α that characterizes the efficiency of angular momentum transport. Shakura & Sunyaev (1973) developed the most commonly invoked prescription of this kind, proposing a turbulent kinematic viscosity of the form

$$\nu = \alpha v \ell, \quad (2.3)$$

which is the product of the turbulent velocity v and the size ℓ of the largest eddies in the turbulent pattern. As turbulence is quickly dissipated by shocks in a highly supersonic flow, the turbulent velocity is often taken to be roughly equal to the local sound speed of the disk medium, c_s . An upper limit to the size of the largest eddies that form can similarly be argued to be roughly equal to the disk half-thickness H ; hence

$$\nu = \alpha \frac{c_s^2}{\Omega}, \quad (2.4)$$

where we have used $H = c_s/\Omega$, and imposed that the disk be everywhere in vertical hydrostatic equilibrium. Taken together, these arguments imply that α should be less than unity. Determinations based on measurements of the accretion rates from disks surrounding young stellar objects in the Taurus complex suggest that $\alpha \sim 10^{-2}$ (Hartmann et al., 1998). However, if and why α should be spatially uniform and constant in time remains unclear.

Balbus & Hawley (1991) have demonstrated that a disk governed largely by hydrodynamic turbulence can be made unstable if the disk is threaded by a magnetic field (cf., Klahr & Bodenheimer, 2003; Johnson & Gammie, 2005, regarding the stability of purely hydrodynamic disks). Even in the presence of an initially weak field, simulations show that the nonlinear outcome of the magnetorotational instability (MRI) can amplify and sustain the degree of turbulence required for vigorous angular momentum transport (Brandenburg et al., 1995; Hawley et al., 1996). When used as a comparator against observations, these parameterizations suggest a value for α in the range of 10^{-3} – 0.5 (Stone et al., 2000, and references therein). However, MRI requires that the disk be sufficiently ionized for any present magnetic field to remain sufficiently coupled to the disk material (Fromang et al., 2002). Hence, the low ionization fractions present in the cold and dusty disks that typically surround young stars may reduce—or eliminate entirely—the effectiveness of MRI-induced angular momentum transport (Fleming & Stone, 2003).

Gravitational torques represent an alternative source for angular momentum transport in such cold and/or massive disks. Using self-consistent cooling, Boley et al. (2006) showed that an α prescription based on the gravitational instability agrees with the Gammie (2001) description very well, which assumes that the viscous heating is locally balanced by the cooling. Cossins et al. (2009) have also used smoothed particle hydrodynamics to show that these disks often possess tightly wound spiral arms that can be approximated with a local treatment. Here we consider a perturbation in an otherwise axisymmetric thin disk, which has the form of an annulus of width Δr and increased local mass Δm (e.g., the formation of a spiral arm). The growth condition for a perturbation depends on whether its self-gravity is greater than the tidal acceleration acting on it. That is,

$$\frac{G\Delta m}{\Delta r^2} \sim \pi G\Sigma > \frac{GM_*}{r^2} \frac{\Delta r}{r}. \quad (2.5)$$

A natural length scale thus emerges, in excess of which perturbations of this nature are stabilized by their rotation,

$$\Delta r \sim \pi G\Sigma \left(\frac{GM_*}{r^3} \right)^{-1} = \frac{\pi G\Sigma}{\Omega^2}. \quad (2.6)$$

Furthermore, with the assumption of vertical hydrostatic equilibrium, the disk self-gravity is supported by gas pressure in the vertical direction. This additional constraint implies Δr must be at least larger than the disk half-thickness H ,

$$\Delta r \geq H = \frac{c_s}{\Omega}. \quad (2.7)$$

Toomre (1964) originally formulated these arguments, summarizing the instability criterion as:

$$Q \equiv \frac{c_s \Omega}{\pi G \Sigma} < 1. \quad (2.8)$$

This condition can additionally be rephrased in terms of the disk mass. Multiplying equation (2.8) by the square of the disk outer radius, r_{out}^2 , and then approximating the disk mass as $M_{\text{disk}} \sim \pi r_{\text{out}}^2 \Sigma$, Toomre's Q criterion implies

$$\frac{M_{\text{disk}}}{M_*} > \frac{H}{r}. \quad (2.9)$$

From this statement one can conclude that provided the disk is thin, even a relatively low-mass disk will exhibit the effects of self-gravity. Disks of this variety may not be uncommon, possibly forming during the earliest stages of star formation (e.g., Eisner & Carpenter, 2006). The importance of self-gravity in providing an effective way of redistributing angular momentum at the earliest stages of star formation has been recently recognized (Vorobyov & Basu, 2005b; Hartmann et al., 2006; Vorobyov & Basu, 2006).

Lin & Pringle (1987) noted that gravitational torques could be parameterized as an effective kinematic viscosity, constructed dimensionally using the length scales arising from Toomre's analysis: the maximum size of the region over which angular momentum is transferred being roughly $G\Sigma/\Omega^2$, together with a time-scale of approximately Ω^{-1} , produces an effective kinematic viscosity of the form

$$\nu \sim \left(\frac{G\Sigma}{\Omega^2} \right)^2 \frac{1}{\Omega^{-1}} \sim Q^{-2} \frac{c_s^2}{\Omega}. \quad (2.10)$$

This is clearly analogous to the standard α prescription of Shakura & Sunyaev (1973) with $\alpha = Q^{-2}$ (see equation (2.4)). Additionally, by using equation (2.8) we can also write

$$\nu = r^6 \Sigma^2 \Omega / M^2. \quad (2.11)$$

Hence, a convenient feature of parameterizing the gravitational torques via equation (2.11) is that we need not explicitly evaluate the energy equation during the disk evolution. This allows us to study the evolution of the disk while circumventing the complex issues related to the disk thermodynamics. Nevertheless, to validate the consistency of our results with existing 1D simulation work (e.g., Armitage et al., 2001; Rice & Armitage, 2009) as well as higher dimensional models, such as the 2+1D models of Vorobyov & Basu (2006, 2010), we do follow the temperature evolution of the disk implicitly.

In calculating the temperature of the disk we assume it evolves isothermally up to some

critical density Σ_{crit} , and in a polytropic manner thereafter. The critical surface mass density at which this transition occurs is $\Sigma_{\text{crit}} = 36.2 \text{ g cm}^{-2}$, and corresponds to a critical volume density of $n_{\text{crit}} \sim 10^{11} \text{ cm}^{-3}$ for a gas disk in vertical hydrostatic equilibrium at $T = 10 \text{ K}$ (Larson, 2003). Matching the isothermal and non-isothermal regimes, the effective vertically integrated gas pressure as a function of surface mass density can therefore be expressed as (Vorobyov & Basu, 2006)

$$P = c_{s,0}^2 \Sigma + c_{s,0}^2 \Sigma_{\text{crit}} \left(\frac{\Sigma}{\Sigma_{\text{crit}}} \right)^\gamma. \quad (2.12)$$

Here, $c_{s,0}$ is the sound speed corresponding to a medium of predominantly molecular hydrogen (with an admixture of helium) that is isothermal with $T = 10 \text{ K}$. For the ratio of the specific heats we used $\gamma = 5/3$.

The gas temperature, via the ideal gas equation of state $P = \Sigma k_B T / \mu m_p$, is then simply

$$T = \frac{c_{s,0}^2 \mu m_p}{k_B} \left[1 + \left(\frac{\Sigma}{\Sigma_{\text{crit}}} \right)^{\gamma-1} \right], \quad (2.13)$$

where μ is the mean molecular mass (which we take to be 2.36), m_p is the proton mass, and k_B is Boltzmann's constant.

Angular momentum transport by gravitational instability (or more appropriately, gravitational torques, as being described herein) has been shown to remain effective in the regime of $Q \gtrsim 1$ (Vorobyov & Basu, 2006, 2007, 2009a,b). In their 2006 study specifically, it was found that radial profiles of the Toomre Q parameter were both near-uniform and noticeably larger during periods of quiescence in the mass accretion rate, and never falling below 2.5–3.0 during this phase. Although the persistence of gravitational instabilities is not usually expected for these values of Q , their 2+1D simulations revealed that weak spiral structures formed early on in the formation of the disk were then sustained by a swing amplification mechanism (Vorobyov & Basu, 2007). In fact, strong observational evidence for spiral structure has actually been found in several-million year old disks such as HD 100546 (Grady et al., 2001), AB Aurigae (Fukagawa et al., 2004), and HD 135344B (Muto et al., 2012), all in support of this conjecture.

2.3 Results

We investigate the temporal evolution of more than 200 initial protostar-disk configurations. The parameter space of our models include initial protostellar masses of $0.2 M_\odot \leq M_* \leq 3.0 M_\odot$, corresponding to the range of intermediate- to upper-mass T Tauri stars. This range is divided into intervals of $0.1 M_\odot$ up to $1.1 M_\odot$, and intervals of $0.2 M_\odot$ thereafter. Each protostar harbors a disk that extends from $r_{\text{in}} = 10^{-1} \text{ AU}$ to an initial size r_{edge} that is $\ll r_{\text{out}} =$

10^4 AU, ensuring that the simulation’s outer boundary has no influence on the disk evolution. We note that since we model the late-time quiescent evolution of the disk, the time $t = 0$ in our simulations represents the state of a disk that is already $\gtrsim 10^5$ yr old (e.g., see Figure 1 in Vorobyov & Basu, 2007). Our simulations end after an additional 2×10^6 yr, congruent with observational estimates of disk lifetimes in the post-embedded phase (see Williams & Cieza, 2011, and references therein).

2.3.1 Initial Conditions

We presume that each protostar-disk system is formed as a result of the collapse of a rotating prestellar core. Numerical simulations of this process (e.g., Vorobyov & Basu, 2006, 2010; Vorobyov, 2011) show that a disk formed in this manner undergoes an initial burst mode of accretion driven by gravitational instabilities. At the end of this phase, the disk settles into a more quiescent phase, which we model in this paper, and is characterized by a disk roughly 100 AU in radius. We follow the numerical results of Vorobyov & Basu (2007, 2008) and adopt a prescription weakly correlating the disk mass (at $t = 0$) with the host protostar’s mass, $M_{\text{disk}} \propto M_*^{0.3}$. This produces disk mass fractions in the range of 5% at the low mass end, to $\sim 14\%$ for the highest mass stars in our study. Though this mass fraction is larger than what is typically reported for disks of the ages we are studying, there is significant uncertainty in the disk masses estimated from dust emission (e.g., Andrews & Williams, 2005). Dust grain growth to sizes $\gtrsim 1$ mm, for example, decrease the millimeter wavelength opacity allowing for substantially higher disk masses (e.g., D’Alessio et al., 2001; Williams & Cieza, 2011)

Between r_{in} and r_{edge} the local surface mass density within the disk scales as $\Sigma \propto r^{-3/2}$, and is exponentially tapered thereafter. This is consistent with theoretical estimates for the minimum-mass solar nebula (Hayashi, 1981), and the extrapolated radial profiles of observably resolved disks (e.g., Hartmann et al., 1998). For completeness we have also investigated the evolution of disks with two alternative initial profiles: $\Sigma \propto r^{-1}$ and $\propto r^{-2}$. However, the action of (2.1) and (2.10) readjusts the surface mass density distribution of the disk to be $\propto r^{-3/2}$ within $\sim 10^5$ yr, rendering the initial distinction inconsequential for the subsequent evolution. Evolution toward $Q \approx 1$ in an environment with near Keplerian rotation and weak temperature variation will invariably lead to a profile $\Sigma \propto r^{-3/2}$, as can be seen from equation (2.8).

We estimate the scaling of the initial disk radial extent r_{edge} with central object mass M_* as follows. A parcel of material initially located at a cylindrical radius r that possesses a specific angular momentum j and that falls in from the outermost mass shell of the cloud core, can be expected to land in the plane of the disk at $r_{\text{edge}} = j^2/GM_*$. Here, we have used a rough equality of core mass M and final central object mass M_* . For a rotating and collapsing cloud

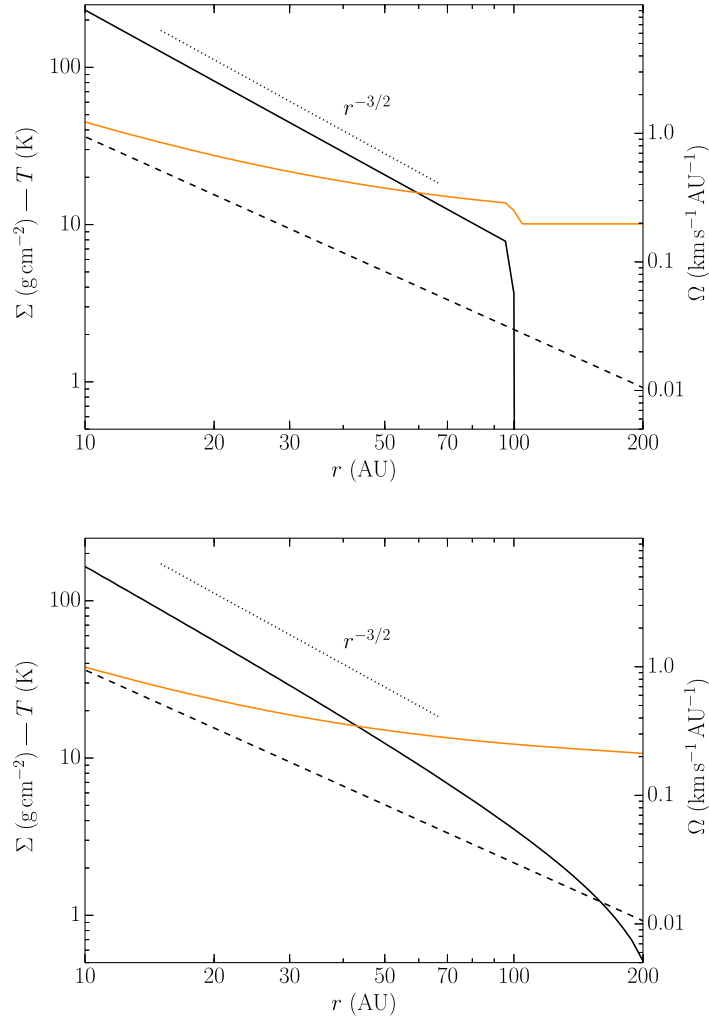


Figure 2.1: Snapshots of several disk characteristics at the beginning of the simulation (i.e., $t = 0$; top), and at the simulation’s end $t = 2 \times 10^6$ yr (bottom). The protostar’s initial mass is $1.0 M_{\odot}$ at $t = 0$; its associated disk contains $0.1 M_{\odot}$, and extends to $r_{\text{edge}} = 100$ AU. Shown are radial profiles of surface density Σ (solid black lines), angular velocity Ω (dashed black lines), and temperature T (solid orange lines). The correlation between surface mass density with radius as $\Sigma \propto r^{-3/2}$ is also shown to guide the eye (dotted black line).

core we expect surface mass density and rotation profiles $\Sigma \propto r^{-1}$ and $\Omega \propto r^{-1}$, respectively (Basu, 1997). In this case, $j = \Omega r^2 \propto r$ and $M \propto r$, so that $j \propto M$. We therefore expect disk sizes to directly correlate with protostellar mass approximately as

$$r_{\text{edge}} \propto M_*, \quad (2.14)$$

where we use the empirically motivated scale that $M_* = 1 M_\odot$ corresponds to $r_{\text{edge}} = 100 \text{ AU}$. We use this relation as a proxy for determining disk sizes in our models at $t = 0$.

In Figure 2.1 we present snapshots of the radial profiles of the disk surface mass density Σ (solid black lines), angular velocity Ω (dashed black lines), and temperature T (solid orange lines) at times $t = 0$ (top) and $2 \times 10^6 \text{ yr}$ (bottom). As the overall surface density declines with time, the disk edge moves steadily outward. Most of the mass redistribution occurs within this first 10^6 yr , during which time the disk size increases to $\sim 250 \text{ AU}$. Over a subsequent 10^6 yr the disk size increases by only another $\sim 50 \text{ AU}$. This late-time quiescent evolutionary phase is also characterized by values of Q of order unity throughout the disk. Such behavior is consistent with that seen in more robust 2D simulations of disk evolution such as those performed by Vorobyov & Basu (2006, 2010).

2.3.2 Mass Accretion Rates

The instantaneous mass accretion rate onto the protostar is calculated from the change in the total disk mass between time steps, as mass loss from the disk occurs only through the inner boundary of the simulation domain (being that r_{edge} is always $\ll r_{\text{out}}$). Figure 2.2 illustrates the time evolution of mass accretion rates between 10^4 and $2 \times 10^6 \text{ yr}$ for protostars with initial masses of $0.2 M_\odot \leq M_* \leq 3.0 M_\odot$.

The mass accretion rates onto the star are relatively constant at all masses during the first $\sim 10^5 \text{ yr}$ as the disks approach a quasi-steady state, characterized by the radial mass accretion rate throughout the disk being uniform. The range in \dot{M} between the least and most massive systems spans more than three orders of magnitude during this time: the $0.2 M_\odot$ protostar accretes material from its disk at a rate of several times $10^{-10} M_\odot \text{ yr}^{-1}$; the $3.0 M_\odot$ protostar, at a rate of a few times $10^{-7} M_\odot \text{ yr}^{-1}$.

Once a disk has settled into a quasi-steady state however, \dot{M} begins to decline as $t^{-6/5}$ (as found by Lin & Pringle, 1987). Transition into this regime is a direct consequence of the parameterization of the effective kinematic viscosity in terms of Toomre’s Q criterion—specifically the strong dependence of ν on Σ in equation (2.11). We find that the length of time preceding the transition scales approximately as $M_*^{-1/2}$. This causes the range of accretion rates spanned by systems with different initial masses to decrease with time.

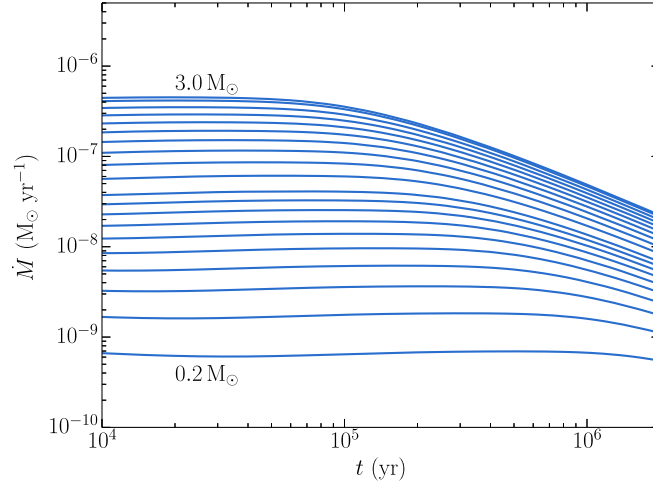


Figure 2.2: Temporal evolution of mass accretion rates in disks evolved with Q based viscosity for 21 protostars with initial masses with $0.2 M_{\odot} \leq M_* \leq 3.0 M_{\odot}$. The accretion rate for each protostar-disk system is initially relatively constant. Once the system settles into a quasi-steady state, the accretion rate declines as $t^{-6/5}$ (Lin & Pringle, 1987). The length of time any one system requires to reach the quasi-steady state scales roughly as $M_*^{-1/2}$. As a result, the order of magnitude difference in \dot{M} between the least and most massive systems decreases with time.

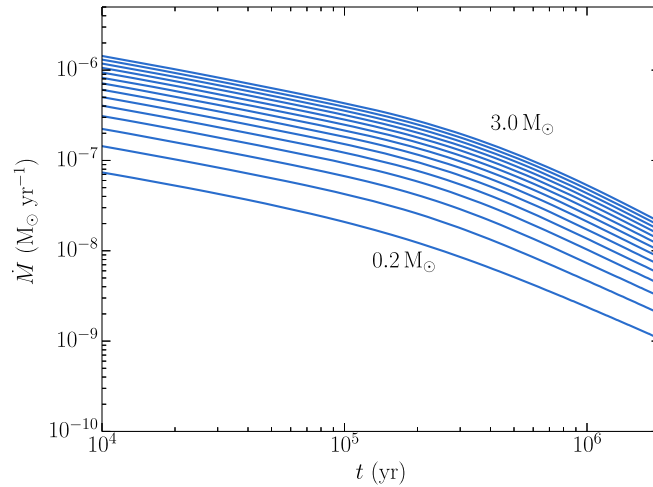


Figure 2.3: Temporal evolution of mass accretion rates in disks evolved with α viscosity for 21 protostars with initial masses with $0.2 M_{\odot} \leq M_* \leq 3.0 M_{\odot}$. The standard α parameterization (e.g., Shakura & Sunyaev, 1973) is used with $\alpha = 10^{-2}$. There is an approximately one order of magnitude difference in \dot{M} between the least and most massive protostar-disk systems. The constant value of this range of \dot{M} on a logarithmic scale is in sharp contrast to the decrease in range seen in disks whose viscosity is described by gravitational torques.

For contrast, in Figure 2.3 we provide an example of the analogous evolution of \dot{M} for disks in which the effective kinematic viscosity is described by the spatio-temporally constant classical α parameterization of equation (2.4) (Shakura & Sunyaev, 1973). We take α to have a fiduciary value of 10^{-2} in these models, consistent with estimates inferred from fitting disk similarity solutions to statistically significant samples of disk observations spanning different ages (e.g., Andrews et al., 2009). The disks modeled in this fashion exhibit a steady decline in their mass accretion rates with time, irrespective of the mass of the system. It is clear that for these objects there is little change in the range of mass accretion rates spanned by the least and most massive protostar-disk systems. This makes it difficult for α models to reproduce the steepness of the observed $\dot{M}-M_*$ correlation.

2.3.3 $\dot{M} - M_*$ Correlation

For the regime of intermediate to upper mass T Tauri stars ($M_* > 0.2 M_\odot$), the exponent of the power law correlation β , between mass accretion rate \dot{M} and protostellar mass M_* , can be taken to be approximately 1.3 (e.g., Muzerolle et al., 2005; Herczeg & Hillenbrand, 2008). In Figure 2.4 we present mass accretion rates from more than 200 individual simulations, which reflect the evolution of protostars with masses of $0.2 M_\odot \leq M_* \leq 3.0 M_\odot$, and their disks, over 2×10^6 yr. Although material is being accreted from the disk and onto the protostar in these simulations, the change in M_* with time is negligible compared to the order of magnitude changes in \dot{M} over the same period. A single simulation thus produces a seemingly vertical evolutionary track within the figure. For clarity, we plot only those values of \dot{M} at every 1,000th time step from the individual simulations. Variations in the initial disk size— r_{edge} , as determined through equation (2.14)—cause protostar-disk systems with the same initial mass to follow slightly different evolutionary trajectories. The open circles are observational measurements of \dot{M} for protostars in the same mass range as those of our simulation, from the compilation of Muzerolle et al. (2005). A least squares fit to this data produces $\beta = 1.3 \pm 0.3$. A least squares fit to the simulation data yields $\beta = 1.7$, in reasonable agreement with that estimated from observations.

Instead of a least squares fit, if we were to consider isochrones connecting together systems of different mass at the same age in Figure 2.4, we would see that β decreases as a function of protostellar age. This is most apparent in the difference in the slope of the lines that form the upper and lower envelope bounding the simulation data at $t = 0$ and 2×10^6 yr, respectively. Note that only a handful of the observational measurements fall outside of this envelope. The most significant outliers are the particularly high accreters found at the lowest masses. However, we suspect these objects are likely younger than those represented in our simulations,

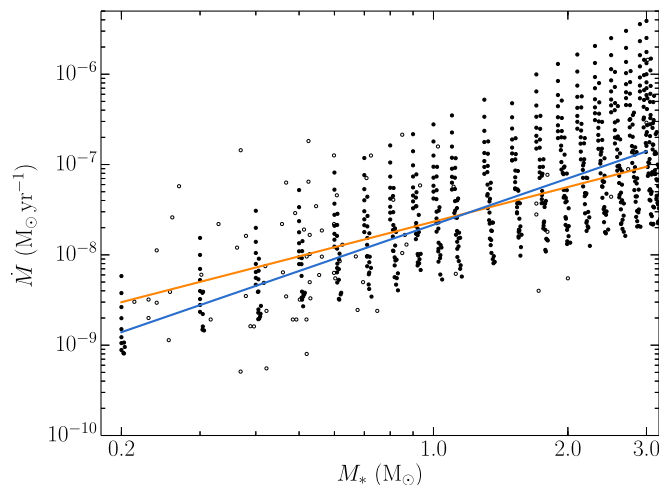


Figure 2.4: Mass accretion rates \dot{M} versus protostellar mass M_* . Open circles are observational measurements of objects with mass $\geq 0.1 M_{\odot}$ from Muzerolle et al. (2005, and references therein). We evolve more than two hundred different initial protostar-disk configurations over 2×10^6 yr. Filled circles are the mass accretion rates for these systems at every 1,000th time step. The orange line is the least squares fit to the observed mass accretion rates, and produces a $\beta = 1.3 \pm 0.3$. The blue line is the equivalent fit to the values of \dot{M} from our simulations, and produces a $\beta = 1.7$.

and still enshrouded by the material of their natal environment. Infall from their surroundings can induce disk instability and fragmentation. The resulting burst mode of accretion (e.g., Vorobyov & Basu, 2006, 2010) is known to dominate the quiescent mode of accretion (modeled here) at early times.

For a more limited sampling of the \dot{M} – M_* parameter space than above, different values of β can be measured. To explore this possibility we randomly sample the spectrum of \dot{M} – M_* results from our simulations using an initial mass function (IMF) of the form proposed by Chabrier (2005). Initial protostellar masses are acquired from the Chabrier IMF. From these we determine a disk mass $M_{\text{disk}} \propto M_*^{0.3}$ (as in Section 4.3.2) and size r_{edge} (equation 2.14) at time $t = 0$ for each model. We then uniformly sample each model’s temporal history in order to determine a specific value of \dot{M} . After 100 such “measurements” we are then able to estimate a value of β . Figure 2.5 presents a histogram summarizing the value of β from 10,000 such samplings. The average value of the exponent of the power law correlation in \dot{M} – M_* is $\beta = 1.4$, with a standard deviation of ~ 0.1 . This places the value of β as determined from our simulations well within the error bounds of the observationally determined value.

In Figure 2.6 we present one example of this sampling procedure for which the simulation data produces a typical value for the power law exponent of $\beta = 1.4 \pm 0.1$. In Figure 2.7

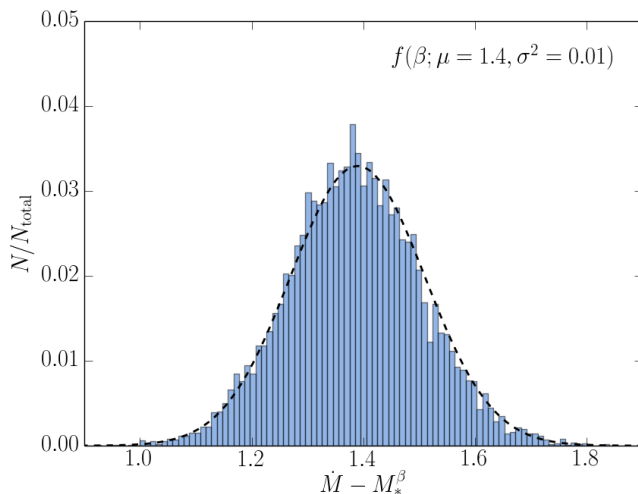


Figure 2.5: A histogram of the slopes β for the correlation between mass accretion rate and protostellar mass, $\dot{M} - M_*^\beta$, for 10,000 samples generated by method described in the text. The distribution of slopes is reasonably well fit by a Gaussian curve with mean $\mu = 1.4$ and variance $\sigma^2 = 0.01$ (dashed black line).

we also present the number distributions of protostellar masses, and of mass accretion rates, for the observational measurements and the randomly selected simulation points. By visual inspection, the observational measurements and the sample drawn from the simulations are in general agreement. However, we can quantify this agreement statistically, as well as across repeated samples, to evaluate the likelihood with which our model is capable of reproducing the observed correlation.

For each of the 10,000 samplings represented in Figure 2.5, we construct the corresponding number distributions by mass and mass accretion rate, as in Figure 2.7. We then perform a two-sample Kolmogorov-Smirnov test to evaluate the null-hypothesis that the number distributions by mass and mass accretion rate between the observed and our randomly generated samples have been drawn from the same underlying distributions. Figure 2.8 presents two histograms that summarize the p values resulting from this test, where the p value is an estimate of the probability that the two distributions are representative of a singular underlying sample; considered unlikely for $p < 0.05 \sim 2\sigma$. In general, we find p to be sufficiently large such that the null-hypothesis cannot be strictly ruled out. However, in roughly half of our randomly generated samples, we are unable to reproduce the magnitude spread in mass accretion rates that exists among observational measurements. As we discussed earlier, this is likely the result of younger objects than those represented in our simulations, in which infall from the surrounding environment is likely to dominate the accretion mode.

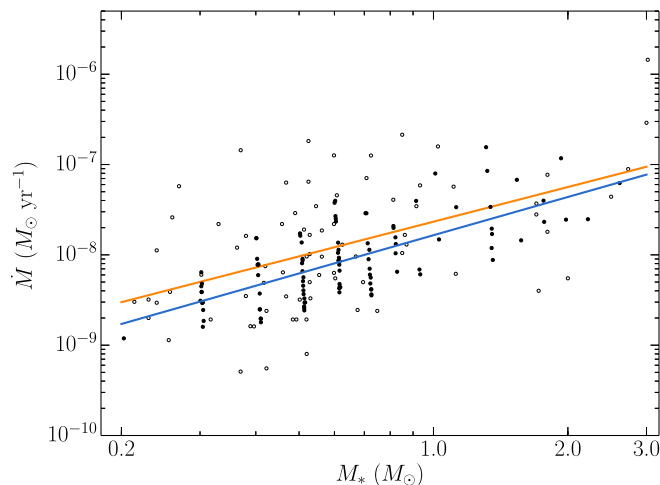


Figure 2.6: We highlight one example of a plot of $\dot{M}-M_*$ generated by the selection criterion discussed in the text. For reference, the open circles are the observational measurements of T Tauri stars in the mass range of $0.2 M_{\odot} < M_* < 3.0 M_{\odot}$, from Muzerolle et al. (2005, and references therein). The orange line is the least squares fit to the observational data, and yields a value for the power law exponent of $\beta = 1.3 \pm 0.3$. The filled circles are the data obtained from our simulations, and the blue line is the least squares fit to these points, yielding $\beta = 1.4 \pm 0.1$.

2.4 Summary & Discussion

In this paper, we have shown that the observed power law correlation between mass accretion rate \dot{M} and protostellar mass M_* can be explained within the framework of gravitational–torque–driven transport. We parameterize the effects of the gravitational torques as an effective kinematic viscosity using Toomre’s Q criterion (Toomre, 1964), noting that this prescription resembles but also differs from the classical α model of Shakura & Sunyaev (1973).

We carry out more than 200 individual simulations of protostellar disks in order to examine the time evolution of their mass accretion rates in the $\dot{M} - M_*$ plane. The rates associated with a particular protostellar mass agree with those inferred from observational studies of T Tauri disks across a broad spectrum of protostellar masses. The observed scatter in \dot{M} arises naturally as a result of the temporal evolution of the protostar-disk system through this plane. We are able to use a simple statistical argument, resampling our simulations onto the initial mass function of Chabrier (2005), to show that even with limited sampling, our simulation results are sufficiently robust so as to be able to reproduce the observed correlation.

The initial disk masses presented in this paper are somewhat greater than is often reported in the literature (perhaps by a factor of ~ 10 , e.g., Andrews & Williams, 2005). However, current estimates for disk masses based on dust emission may have been systematically underestimated

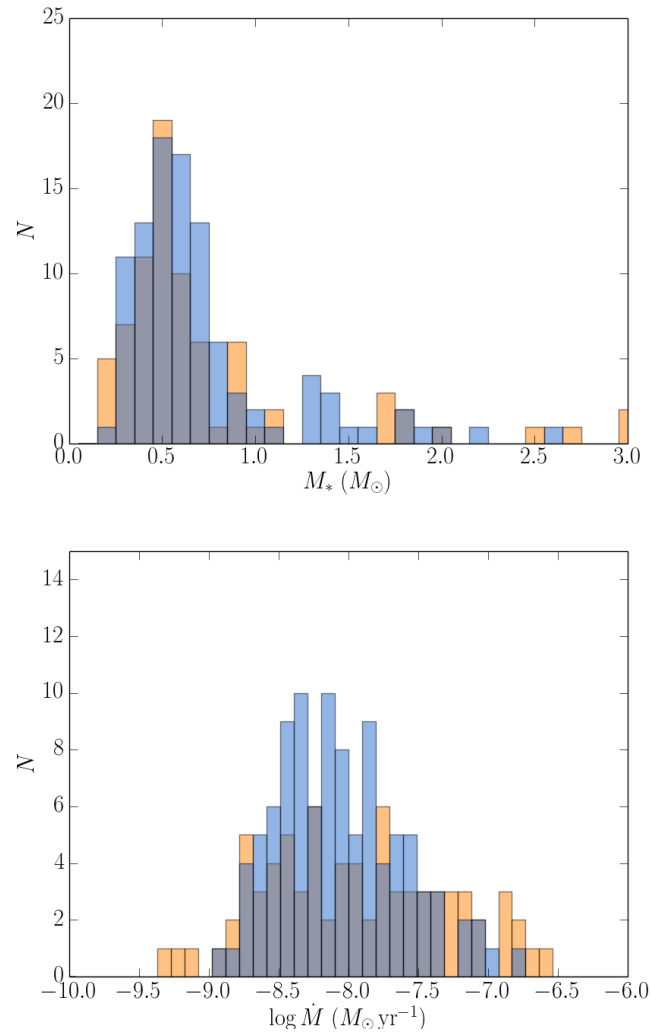


Figure 2.7: Histograms of the number distributions by protostellar mass M_* (top), and by mass accretion rate \dot{M} (bottom), of both the observational measurements (orange) and simulation data (blue), gray regions indicating overlap, as they appear in Figure 2.6. A Kolmogorov-Smirnov two-sample test, comparing the number distributions of the observational measurements to their corresponding simulation counterparts, produces a p value of roughly 0.10 in each case. The randomly selected simulation data is thus statistically indistinguishable from the observational measurements.

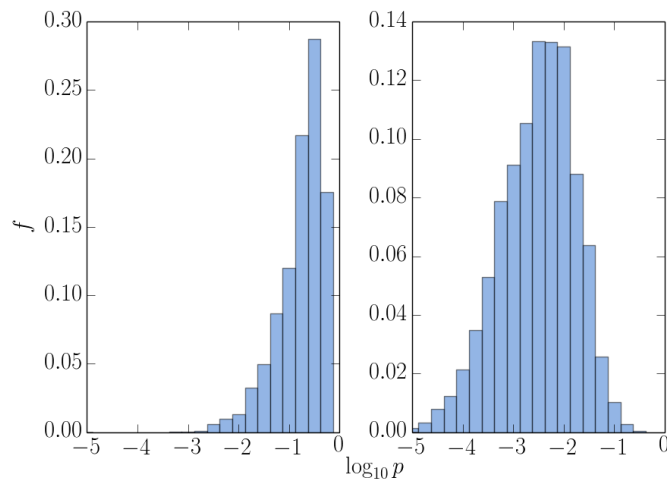


Figure 2.8: Logarithm of the p values from Kolmogorov-Smirnov two-sample tests comparing the number distributions by mass (left), and by mass accretion (right), between the observed measurements and those from simulations.

(Hartmann et al., 2006). Nevertheless, as the efficacy of our transport mechanism is dependent on disk mass, it is possible that additional physics may be required at late times to remove the remaining disk material within observed disk lifetimes (Hernández et al., 2008).

As Figure 2.2 shows, \dot{M} in our model is initially a mass dependent product of the earlier burst phase, and then gradually evolves from a shallow time-dependence to a steeper one that is consistent with self-similar evolution. Transition between these distinct accretion regimes is mass dependent, with objects of greater mass making the transition at earlier times. These elements are an important factor of our model that allow us to fit to the observed $\dot{M} - M_*$ relation.

In a recent paper, Ercolano et al. (2014) offer a physically different model explanation. In their view, \dot{M} is initially mass independent, and declines in a self-similar manner with a somewhat different power law index than in our model, due to the use of an α -viscosity. Mass accretion is then quenched when a model wind mass loss rate (that depends on the X-ray luminosity of the protostar) equals the mass accretion rate. The physical view here is that the observed mass-dependent X-ray luminosity sets the $\dot{M} - M_*$ relation by reducing the accretion rate when it drops to the level of the wind mass loss rate. Mathematically however, both models depend partially upon a bimodal mass accretion rate history. It is only the physical explanation of the two phases, and the specific mathematical shape of their curves, that differ. The observed correlation in $\dot{M} - M_*$ may therefore be fit by a variety of models that have common mathematical elements, but differ substantially enough in their physics that they will hopefully lead to interesting observational comparator tests in the future.

Bibliography

- Alexander, R. D. & Armitage, P. J. 2006, *ApJL*, 639, L83
- André, P., Ward-Thompson, D., & Barsony, M. 1993, *ApJ*, 406, 122
- Andrews, S. M. & Williams, J. P. 2005, *ApJ*, 631, 1134
- Andrews, S. M., Wilner, D. J., Hughes, A. M., Qi, C., & Dullemond, C. P. 2009, *ApJ*, 700, 1502
- Armitage, P. J., Livio, M., & Pringle, J. E. 2001, *MNRAS*, 324, 705
- Balbus, S. A. & Hawley, J. F. 1991, *ApJ*, 376, 214
- Basu, S. 1997, *ApJ*, 485, 240
- Beckwith, S. V. W., Sargent, A. I., Chini, R. S., & Guesten, R. 1990, *ApJ*, 99, 924
- Binney, J. & Tremaine, S. 2008, *Galactic Dynamics* (Princeton University Press)
- Boley, A. C., Mejía, A. C., Durisen, R. H., Cai, K., Pickett, M. K., & D'Alessio, P. 2006, *ApJ*, 651, 517
- Brandenburg, A., Nordlund, A., Stein, R. F., & Torkelsson, U. 1995, *ApJ*, 446, 741
- Chabrier, G. 2005, in *The Initial Mass Function 50 Years Later*, ed. E. Corbelli, F. Palla, & H. Zinnecker, 41
- Cossins, P., Lodato, G., & Clarke, C. J. 2009, *MNRAS*, 393, 1157
- D'Alessio, P., Calvet, N., & Hartmann, L. 2001, *ApJ*, 553, 321
- Dullemond, C. P., Natta, A., & Testi, L. 2006, *ApJL*, 645, L69
- Eisner, J. A. & Carpenter, J. M. 2006, *ApJ*, 641, 1162
- Ercolano, B., Mayr, D., Owen, J. E., Rosotti, G., & Manara, C. F. 2014, *MNRAS*, 439, 256

- Fleming, T. & Stone, J. M. 2003, *ApJ*, 585, 908
- Fromang, S., Terquem, C., & Balbus, S. A. 2002, *MNRAS*, 329, 18
- Fukagawa, M., Hayashi, M., Tamura, M., Itoh, Y., Hayashi, S. S., Oasa, Y., Takeuchi, T., Morino, J.-i., Murakawa, K., Oya, S., Yamashita, T., Suto, H., Mayama, S., Naoi, T., Ishii, M., Pyo, T.-S., Nishikawa, T., Takato, N., Usuda, T., Ando, H., Iye, M., Miyama, S. M., & Kaifu, N. 2004, *ApJL*, 605, L53
- Gammie, C. F. 2001, *ApJ*, 553, 174
- Garcia, P. J. V., Cabrit, S., Ferreira, J., & Binette, L. 2001, *A&A*, 377, 609
- Grady, C. A., Polomski, E. F., Henning, T., Stecklum, B., Woodgate, B. E., Telesco, C. M., Piña, R. K., Gull, T. R., Boggess, A., Bowers, C. W., Bruhweiler, F. C., Clampin, M., Danks, A. C., Green, R. F., Heap, S. R., Hutchings, J. B., Jenkins, E. B., Joseph, C., Kaiser, M. E., Kimble, R. A., Kraemer, S., Lindler, D., Linsky, J. L., Maran, S. P., Moos, H. W., Plait, P., Roesler, F., Timothy, J. G., & Weistrop, D. 2001, *AJ*, 122, 3396
- Hartmann, L., Calvet, N., Gullbring, E., & D'Alessio, P. 1998, *ApJ*, 495, 385
- Hartmann, L., D'Alessio, P., Calvet, N., & Muzerolle, J. 2006, *ApJ*, 648, 484
- Hawley, J. F., Gammie, C. F., & Balbus, S. A. 1996, *ApJ*, 464, 690
- Hayashi, C. 1981, *Progress of Theoretical Physics Supplement*, 70, 35
- Herczeg, G. J. & Hillenbrand, L. A. 2008, *ApJ*, 681, 594
- Hernández, J., Hartmann, L., Calvet, N., Jeffries, R. D., Gutermuth, R., Muzerolle, J., & Stauffer, J. 2008, *ApJ*, 686, 1195
- Hueso, R. & Guillot, T. 2005, *A&A*, 442, 703
- Johnson, B. M. & Gammie, C. F. 2005, *ApJ*, 635, 149
- Klahr, H. H. & Bodenheimer, P. 2003, *ApJ*, 582, 869
- Krasnopolsky, R., Li, Z.-Y., & Blandford, R. D. 2003, *ApJ*, 595, 631
- Lada, C. J. & Wilking, B. A. 1984, *ApJ*, 287, 610
- Larson, R. B. 2003, *Reports on Progress in Physics*, 66, 1651

- Lin, D. N. C. & Pringle, J. E. 1987, MNRAS, 225, 607
- Lodato, G. & Rice, W. K. M. 2004, MNRAS, 351, 630
- Lynden-Bell, D. & Pringle, J. E. 1974, MNRAS, 168, 603
- McCaughrean, M. J. & O'Dell, C. R. 1996, AJ, 111, 1977
- Muto, T., Grady, C. A., Hashimoto, J., Fukagawa, M., Hornbeck, J. B., Sitko, M., Russell, R., Werren, C., Curé, M., Currie, T., Ohashi, N., Okamoto, Y., Momose, M., Honda, M., Inutsuka, S., Takeuchi, T., Dong, R., Abe, L., Brandner, W., Brandt, T., Carson, J., Egner, S., Feldt, M., Fukue, T., Goto, M., Guyon, O., Hayano, Y., Hayashi, M., Hayashi, S., Henning, T., Hodapp, K. W., Ishii, M., Iye, M., Janson, M., Kandori, R., Knapp, G. R., Kudo, T., Kusakabe, N., Kuzuhara, M., Matsuo, T., Mayama, S., McElwain, M. W., Miyama, S., Morino, J.-I., Moro-Martin, A., Nishimura, T., Pyo, T.-S., Serabyn, E., Suto, H., Suzuki, R., Takami, M., Takato, N., Terada, H., Thalmann, C., Tomono, D., Turner, E. L., Watanabe, M., Wisniewski, J. P., Yamada, T., Takami, H., Usuda, T., & Tamura, M. 2012, ApJL, 748, L22
- Muzerolle, J., Luhman, K. L., Briceño, C., Hartmann, L., & Calvet, N. 2005, ApJ, 625, 906
- O'Dell, C. R. & Wen, Z. 1994, ApJ, 436, 194
- Pringle, J. E. 1981, ARA&A, 19, 137
- Rice, W. K. M. & Armitage, P. J. 2009, MNRAS, 396, 2228
- Rigliaco, E., Natta, A., Randich, S., Testi, L., & Biazzo, K. 2011, A&A, 525, A47
- Shakura, N. I. & Sunyaev, R. A. 1973, A&A, 24, 337
- Shampine, L. E. 1994, Numerical Solution of Ordinary Differential Equations (Chapman & Hall)
- Shu, F. H., Adams, F. C., & Lizano, S. 1987, ARA&A, 25, 23
- Stone, J. M., Gammie, C. F., Balbus, S. A., & Hawley, J. F. 2000, in Protostars and Planets IV, ed. Mannings, V. and Boss, A. P. and Russell, S. S. (University of Arizona Press)
- Terebey, S., Shu, F. H., & Cassen, P. 1984, ApJ, 286, 529
- Toomre, A. 1964, ApJ, 139, 1217
- Vorobyov, E. I. 2011, ApJ, 729, 146

Vorobyov, E. I. & Basu, S. 2005a, MNRAS, 360, 675

—. 2005b, ApJL, 633, L137

—. 2006, ApJ, 650, 956

—. 2007, MNRAS, 381, 1009

—. 2008, ApJL, 676, L139

—. 2009a, MNRAS, 393, 822

—. 2009b, ApJ, 703, 922

—. 2010, ApJ, 719, 1896

Williams, J. P. & Cieza, L. A. 2011, ARA&A, 49, 67

Yorke, H. W., Bodenheimer, P., & Laughlin, G. 1993, ApJ, 411, 274

Zhu, Z., Hartmann, L., Gammie, C., & McKinney, J. C. 2009, ApJ, 701, 620

Zhu, Z., Hartmann, L., Gammie, C. F., Book, L. G., Simon, J. B., & Engelhard, E. 2010, ApJ, 713, 1134

Chapter 3

The Burst Mode of Accretion in Primordial Star Formation

A version of this chapter has been published in the Astrophysical Journal as Vorobyov, E. I., DeSouza, A. L., and Basu, S. 2012, ApJ, 768, 131.

3.1 Introduction

Cosmological-scale simulations of collapsing primordial clouds in the early universe have been used to suggest that the first luminous objects in the universe were stars with masses of $M \gtrsim 100 M_{\odot}$ that formed in relative isolation (e.g., Abel et al., 2000; Bromm & Loeb, 2004; Yoshida et al., 2008). However, the above numerical simulations were effectively based on a scenario of monolithic quasi-spherical collapse of cloud cores. Angular momentum, disk formation, and fragmentation have added greater depth to this picture, replacing it with one in which the collapsing primordial cores of the early universe produce rich structure in the inner regions where disks emerge.

Although protostellar disks are a ubiquitous outcome of the present-day star formation process, the importance of these structures to the evolution of the first stars has begun to be understood only recently. Saigo et al. (2004) and Machida et al. (2008) have demonstrated that disk-like structures are expected to form from primordial cores with a wide range of initial rotation rates, and can fragment to yield binary pairs of first stars. Clark et al. (2011a) were able to follow the collapse of primordial clouds to protostellar densities and found vigorous gravitational fragmentation in primordial disks leading to the formation of tightly bound multiple stellar systems. Using smoothed particle hydrodynamics simulations combined with the sink particle technique, Smith et al. (2012a,b) studied the importance of accretion luminosity

on disk fragmentation and the effect of protostellar accretion on the structure and evolution of protostars. Greif et al. (2012) most recently performed high-resolution, three-dimensional hydrodynamic simulations using a Lagrangian moving mesh and found rapid migration and merging of secondary fragments with the primary protostar.

The general picture to emerge from these simulations is that protostellar accretion may be a highly variable process fueled by disk gravitational instability and fragmentation, in a similar manner to present-day star formation (Vorobyov & Basu, 2006, 2010; Machida et al., 2011). However, a major problem of high-resolution three-dimensional studies has been the difficulty of following the evolution of primordial protostellar disks for longer than a few thousand years. In this study we present gas hydrodynamics simulations of collapsing primordial cores into a disk formation phase using the thin-disk approximation. We adopt a barotropic equation of state derived by Omukai et al. (2005) for the primordial chemical composition of gas. The benefit of this type of formulation is that we are able to study the fragmentation, evolution and subsequent accretion of protostellar mass clumps formed within the disk, while simultaneously maintaining resolution of the extended remnant parent cloud core over many orbital periods and model realizations.

The structure of this article is as follows. We briefly describe the numerical simulations in Section 2, including the modifications that have been made pertaining to the primordial star-forming environment. In Section 3 we present characteristics of the temporal evolution of our reference model, starting from the prestellar phase, and ending when the mass of the protostar has reached $45 M_{\odot}$. Section 3 also includes an analysis of the protostellar accretion luminosity expected to arise from the burst mode of accretion that is unique to our model of primordial star formation. Finally, in Section 4 we extend our discussion and draw conclusions from these results.

3.2 Model Description

Our model and method of solution update the model presented in Vorobyov & Basu (2005a, 2006), with appropriate modifications for star and disk formation in the early universe. We follow the evolution of gravitationally unstable primordial cores from the isolated pre-stellar stage into the protostar and disk formation stage and terminate our simulations once about 30% of the initial mass reservoir has been accreted onto the protostar plus disk system. Once the disk is formed, it occupies the innermost region of our numerical grid, while the infalling envelope—the remnant of the parent core—occupies the outer extent. The dynamics of both the disk and envelope are followed self-consistently on one global numerical grid space, which ensures correct mass infall rates onto the disk. This is an important prerequisite for study-

ing gravitational instability and fragmentation in young protostellar disks at all epochs (e.g., Vorobyov & Basu, 2006, 2010; Machida et al., 2010; Kratter et al., 2010).

We introduce a sink cell at $r_{\text{sc}} = 6.0$ AU and impose a free inflow inner boundary condition. In the early pre-stellar phase of evolution, we monitor the mass accretion rate through the sink cell and introduce a central point-mass object (representing the forming star) when the mass accretion rate reaches a peak value (see Figure 3.9 for details). In the subsequent evolution, approximately 95% of the accreted material lands directly onto the star, while the rest is maintained in the sink cell in order to keep its density equal to the mean density of the gas in the innermost 1 – 2 AU of the actual numerical grid. The sink cell is otherwise dynamically inactive. It contributes only to the total gravitational potential, so that a smooth transition in column density is maintained from the numerical grid, into the sink cell, and to the protostellar surface.

We solve the mass and momentum transport equations, written in the thin-disk approximation as:

$$\frac{\partial \Sigma}{\partial t} + \nabla \cdot (\Sigma \mathbf{v}) = 0, \quad (3.1)$$

$$\frac{\partial}{\partial t} (\Sigma \mathbf{v}) + \nabla \cdot (\Sigma \mathbf{v} \otimes \mathbf{v}) = -\nabla \mathcal{P} + \Sigma \mathbf{g}, \quad (3.2)$$

where Σ is the surface mass density, $\mathcal{P} = \int_{-H}^H P dz$ is the vertically integrated form of the gas pressure P , H is the radially and azimuthally varying vertical scale height determined in each computational cell using an assumption of local hydrostatic equilibrium (Vorobyov & Basu, 2009), $\mathbf{v} = v_r \hat{\mathbf{r}} + v_\phi \hat{\boldsymbol{\phi}}$ is the velocity in the disk plane, $\mathbf{g} = g_r \hat{\mathbf{r}} + g_\phi \hat{\boldsymbol{\phi}}$ is the gravitational acceleration in the disk plane, and $\nabla = \hat{\mathbf{r}} \partial / \partial r + \hat{\boldsymbol{\phi}} r^{-1} \partial / \partial \phi$ is the gradient along the planar coordinates of the disk. The planar components of the divergence of the symmetric dyadic $\Sigma \mathbf{v} \otimes \mathbf{v}$ are found in Vorobyov & Basu (2010). The thin-disk approximation is an excellent means of studying the evolution over many orbital periods and across a wide parameter space.

The gravitational acceleration \mathbf{g} includes contributions from the central point-mass star (once formed), from material in the sink cell ($r < r_{\text{sc}}$), and from the self-gravity of the circumstellar disk and envelope. The gravitational potential of the circumstellar disk and envelope is found by solving the Poisson integral

$$\Phi(r, \phi) = -G \int_{r_{\text{sc}}}^{r_{\text{out}}} r' dr' \int_0^{2\pi} \frac{\Sigma d\phi'}{\sqrt{r'^2 + r^2 - 2rr' \cos(\phi' - \phi)}}, \quad (3.3)$$

where r_{out} is the radial position of the outer computational boundary, or equivalently, the initial radius of a pre-stellar core. This integral is calculated using a fast Fourier transform technique which applies the two-dimensional Fourier convolution theorem for polar coordinates with a

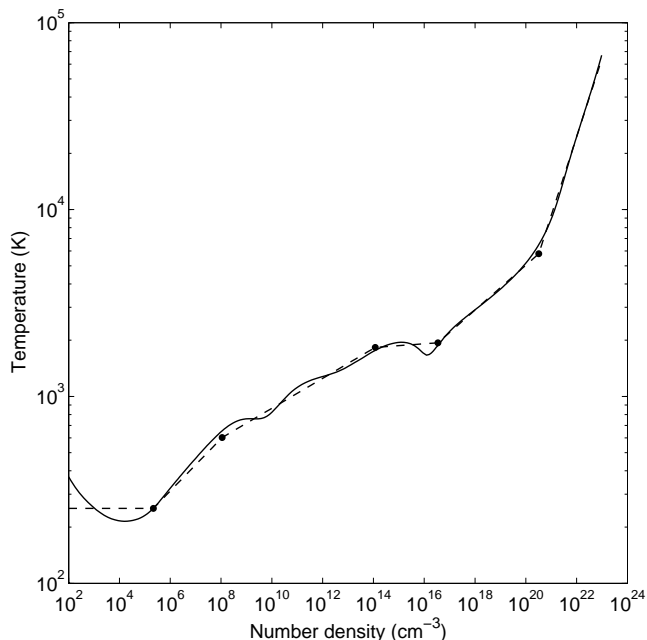


Figure 3.1: Temperature evolution of zero-metallicity gas derived from the one-zone calculations of Omukai et al. (2005, solid line), and the piecewise polytropic fit employed within the simulations discussed herein (dashed line); the filled circles mark the critical turning points of the fit specified in Table 3.1.

logarithmically-spaced radial grid (see Binney & Tremaine, 1987, Section 2.8).

Equations (4.2) and (4.3) are closed with a barotropic equation of state, based on the 1D core collapse simulations of Omukai et al. (2005) that included the detailed chemical and thermal processes of the collapsing gas. Figure 3.1 shows the gas temperature versus density relation from Omukai et al. (2005) for zero metallicity (solid line) and our piecewise fit (dashed line), with the transition points denoted by filled circles. This piecewise polytropic form can be expressed as follows

$$\mathcal{P}_k = c_s^2 \rho^{\gamma_k} \prod_{i=1}^{k-1} \rho_{c,i}^{\gamma_i - \gamma_{i+1}}, \quad \text{for } \rho_{c,k-1} \leq \rho < \rho_{c,k}, \quad (3.4)$$

where $c_s = \sqrt{\mathcal{R}T/\mu}$ is the initial isothermal sound speed, T is the initial gas temperature, \mathcal{R} is the universal gas constant, and $\mu = 2.27$ is the mean molecular weight of the primordial gas¹. The value of the index k distinguishes the six individual components of the piecewise form. We note that when $k = 1$ the product term is unity, and the pressure reduces to $P_1 = c_s^2 \rho^{\gamma_1}$. As

¹True for gas with volume density higher than 10^{10} cm^{-3} . As a rule, our model disks are characterized by volume densities higher than this value, except perhaps in the very outer parts at $r > 300 - 400 \text{ AU}$.

Table 3.1: Parameters of the Barotropic Relation

k	γ_i	$\rho_{c,i}$ (g cm ⁻³)	$n_{c,i}$ (cm ⁻³)
1	1.00	8.20×10^{-19}	2.16×10^5
2	1.14	4.19×10^{-16}	1.10×10^8
3	1.08	4.50×10^{-10}	1.18×10^{14}
4	1.01	1.32×10^{-7}	3.47×10^{16}
5	1.12	1.23×10^{-3}	3.24×10^{20}
6	1.42	—	—

our simulations evolve the effective surface mass density of the gas, the corresponding form of the barotropic relation used in the code is

$$\mathcal{P}_k = c_s^2 \Sigma^{\gamma_k} \prod_{i=1}^{k-1} \Sigma_{c,i}^{\gamma_i - \gamma_{i+1}}, \quad \text{for } \Sigma_{c,k-1} \leq \Sigma < \Sigma_{c,k}, \quad (3.5)$$

where the transition surface and volume mass density are related to one another through the instantaneous local scale height H at each point in the disk via $\rho_{c,i} = \Sigma_{c,i}/2H$. The transition points k , the associated mass and number volume densities at which these transitions occur, $\rho_{c,i}$ and $n_{c,i}$, and the value of the various associated polytrope indices are given in Table 3.1. Note that $\Sigma_{c,0}$ and $\Sigma_{c,6}$ in equation (3.5) are formally equal to zero and infinity, respectively.

The initial gas surface density Σ and angular velocity Ω profiles for the primordial cores are similar to those that have been considered in the context of present-day star formation (Vorobyov & Basu, 2006, 2010)

$$\Sigma = \frac{r_0 \Sigma_0}{\sqrt{r^2 + r_0^2}}, \quad (3.6)$$

$$\Omega = 2\Omega_0 \left(\frac{r_0}{r}\right)^2 \left[\sqrt{1 + \left(\frac{r}{r_0}\right)^2} - 1 \right]. \quad (3.7)$$

The radial profile of Σ is an integrated form of a Bonnor-Ebert sphere (Dapp & Basu, 2009), while that of Ω is the expected differential rotation profile to accompany (3.6) for a core contracting from near-uniform initial conditions (Basu, 1997). The parameters Ω_0 , Σ_0 , and r_0 , are the central angular velocity, central gas surface density, and the radius of a central near-

Table 3.2: Model Parameters

Model	Σ_0 (g cm^{-2})	Ω_0 ($\text{km s}^{-1} \text{pc}^{-1}$)	r_0 (pc)	M_c (M_\odot)	β (10^{-3})	T (K)
<i>ref.</i>	0.26	0.75	0.4	176	2.76	250
<i>1</i>	0.26	0.375	0.4	176	0.69	250
<i>2</i>	0.5	0.75	0.29	179	1.97	350

constant-density plateau, respectively. The latter is proportional to the Jeans length and is defined as

$$r_0 = \frac{\sqrt{A}c_s^2}{\pi G \Sigma_0}. \quad (3.8)$$

The parameter A determines the level of gravitational domination in the initial state. It is set to 1.5 for all models considered herein, and the initial gas temperature is set to 250 K (unless otherwise stated). We note that we have previously shown that the qualitative features of the protostellar accretion and disk evolution are weakly sensitive to the specific profiles adopted for the initial prestellar core (Vorobyov & Basu, 2009; Basu & Vorobyov, 2012).

To set up a model prestellar core using these initial conditions, the values of Σ_0 and Ω_0 need to be specified. The former is determined by r_0 by assuming a constant ratio of the core radius r_{out} to the radius of the central plateau r_0 : $r_{\text{out}}/r_0 = 6$. All model cores therefore possess a similarly truncated form. The parameter r_0 is chosen so as to form cores with mass on the order of $200 M_\odot$. This value is typical for primordial collapsing starless cores, as found in the numerical hydrodynamics simulations of Yoshida et al. (2006).

The central angular velocity Ω_0 of our model cores are characterized by the dimensionless parameter $\eta \equiv \Omega_0^2 r_0^2 / c_s^2$ (Basu, 1997), which is related to the ratio $\beta = E_{\text{rot}}/|\Phi|$ of rotational to gravitational energy by $\beta \approx 0.9\eta$. The value of the central angular velocity Ω_0 is then calculated by choosing a value of β appropriate for primordial cores with spin parameter $\alpha = \sqrt{\beta} \approx 0.05$ (O’Shea & Norman, 2007). Table 3.2 shows a list of parameters for the models presented in this study.

All models are run on a polar coordinate grid with 512×512 spatial zones. The inner and outer boundary conditions are set to allow for free outflow from the computational domain. The radial points are logarithmically spaced, allowing for better numerical resolution of the inner grid, where the disk forms and evolves. In the reference model, the innermost cell outside the central sink has a radius of 0.11 AU and the radial and azimuthal resolution are about 1.9 AU

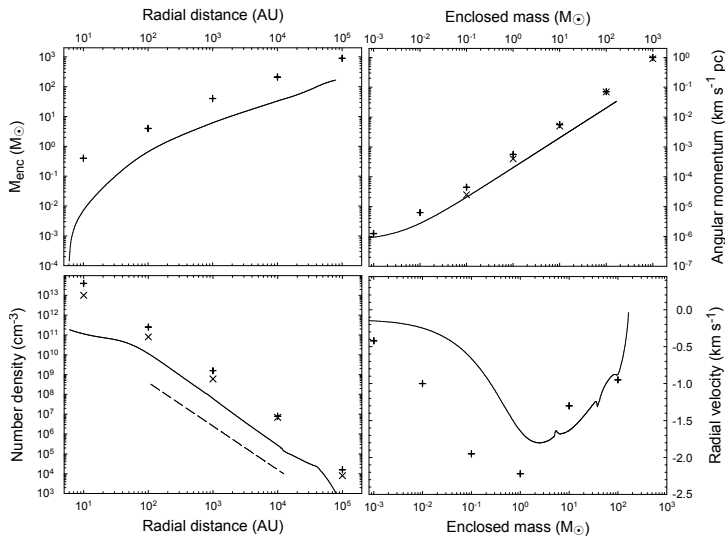


Figure 3.2: Comparison of the core properties in the reference model with those found using numerical hydrodynamics simulations of collapsing primordial mini-halos. The solid lines present the radial profiles of the enclosed mass (top-left panel) and gas volume density (bottom-left panel), and also the specific angular momentum and radial velocity vs. enclosed mass (top-right and bottom-right panels, respectively). The plus signs and crosses are the corresponding data taken from Clark et al. (2011a) and Yoshida et al. (2006), respectively. The dashed line shows the $r^{-2.2}$ profile, typical for the volume density in collapsing mini-halos.

at a radius of 100 AU. This resolution is sufficient to fulfill the Truelove criterion, which states that the local Jeans length must be resolved by at least four numerical cells (Truelove et al., 1998).

Indeed, the Jeans length of a thin self-gravitating disk can be written as

$$\lambda_J = \frac{c_s^2}{G\Sigma_0}. \quad (3.9)$$

For a surface density of $\Sigma_0 \approx 500 - 1000 \text{ g cm}^{-2}$ and temperature $T \approx 1.0 - 1.5 \times 10^3 \text{ K}$, typical for our disks at $r \approx 100 \text{ AU}$ (see Figures 3.1 and 3.7), the corresponding Jeans length varies between $\lambda_J \approx 35 - 90 \text{ AU}$ and is resolved by roughly 17-45 grid zones in each direction (r, ϕ).

Finally, we want to emphasize that we do not resort to the use of sink particles of any sort except for the central sink cell. The fragments studied in this paper are fully self-gravitating protostellar embryos supported against gravity by pressure and rotation.

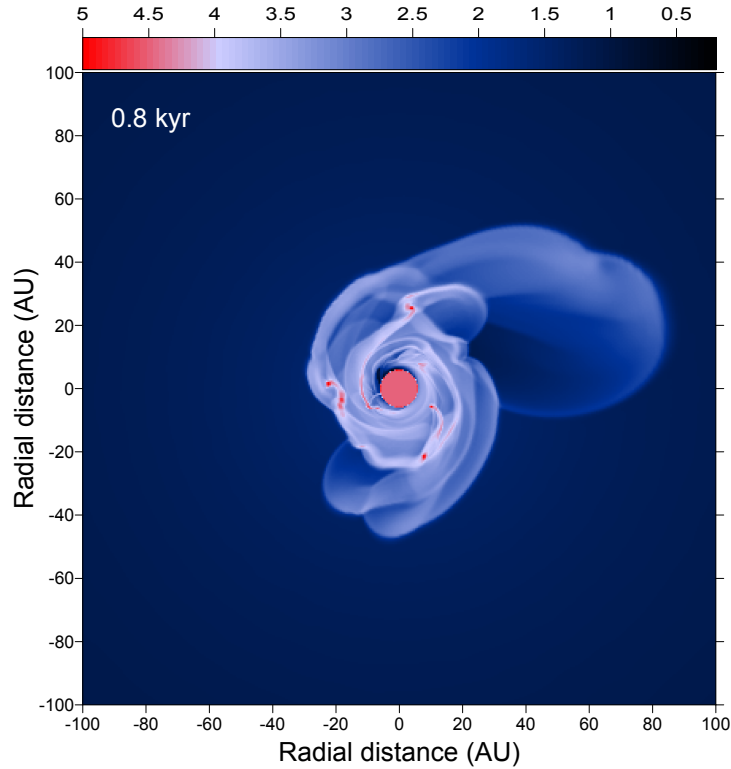


Figure 3.3: Gas surface density map in the reference model showing the disk when its age is just 800 yr. The scale bar is in $\log g \text{ cm}^{-2}$. Multiple fragments are already evident in the disk at this early time.

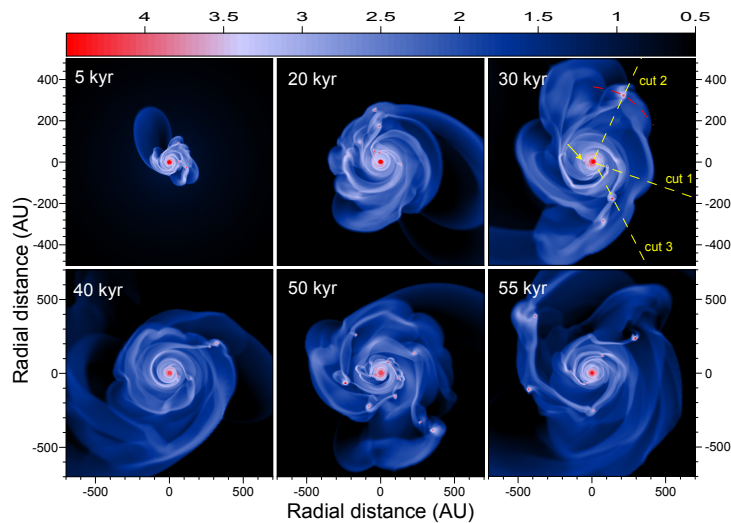


Figure 3.4: Gas surface density maps of the circumstellar disk in the reference model. The time elapsed since the formation of the central star is indicated in each panel. The scale bar is logarithmic in $g \text{ cm}^{-2}$. The yellow dashed lines indicate radial cuts passing through several fragments that are used to calculate the radial gas surface density profiles in Figure 3.7. The red dashed curve illustrates an azimuthal cut used to calculate the gravitational torques acting on a fragment in Fig. 3.7, and the arrow points to fragment F4 in Figure 3.8.

3.3 Results

In this section we consider the time evolution of our reference model (see Table 3.2), starting from the prestellar phase and ending once the mass of the central star reaches $45 M_{\odot}$. Beyond this mass, the effect of stellar irradiation may strongly affect our results (Hosokawa et al., 2011).

3.3.1 Cloud Core at the Onset of the Formation of the Central Protostar

We start by comparing the properties of our collapsing core in the reference model just prior to the formation of the central star to those derived using three-dimensional numerical hydrodynamics simulations of collapsing primordial mini-halos. The solid lines in Figure 3.2 show the enclosed mass M_{enc} versus radial distance r (top-left panel), the gas volume density n versus r (bottom-left panel), the specific angular momentum L versus M_{enc} (top-right panel), and the radial velocity v_r vs. M_{enc} (bottom-right panel). The volume density was retrieved from the gas surface density Σ and the vertical scale height H using the relation $n = \Sigma / (2H\mu m_p)$. We compare our model profiles with those of Clark et al. (2011a) (plus signs) and Yoshida et al. (2006) (crosses). The form of the core in the reference model is similar to those derived using 3D simulations. For instance, the density profile follows closely the usual $r^{-2.2}$ form (shown by the dashed line to guide the eye). A steeper falloff in the core outer regions is caused by a finite core boundary (Vorobyov & Basu, 2005b). However, notable differences are seen in the actual values of n , M_{enc} , v_r , and L . For instance, the gas density in our model is about a factor of several lower than that of Yoshida et al. (2006) and about an order of magnitude lower than that of Clark et al. (2011a). This is primarily caused by the fact that these authors considered more massive cores than we did in our study. This is evident from the top-left panel showing the enclosed mass as a function of radius. The specific angular momentum in our model is a factor of several smaller than that of Clark et al. (2011a) but is approaching that of Yoshida et al. (2006) in the inner region. We could have reconciled the numerically derived profiles by considering cores with a higher initial positive density perturbation A and/or higher angular momentum. This, however, would not alter our main results because such cores would produce more massive and extended disks, whose properties would favor gravitational fragmentation even more (e.g. Vorobyov & Basu, 2006, 2010).

3.3.2 Formation and Evolution of a Primordial Disk

The disk in the reference model starts to form at about $t = 1.0$ kyr after the formation of the central protostar. This delay between the formation of the protostar and the disk could

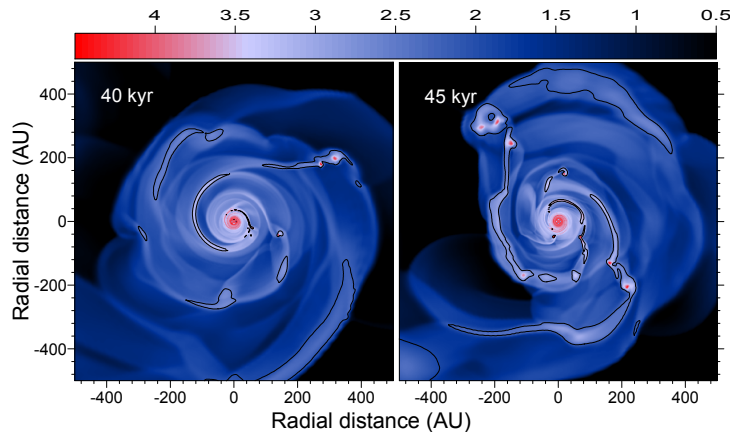


Figure 3.5: Gas surface density maps for the reference model shown at $t = 40$ kyr (left-hand panel) and $t = 45$ kyr (right-hand panel) after the formation of the central star. The contour lines delineate regions in which the Toomre Q -parameter is lower than unity. The scale bar is in $\log \text{g cm}^{-2}$.

have been even shorter had the sink cell radius been smaller than 6 AU. The first episodes of fragmentation occurred about 300 – 400 yr after the formation of the disk. Figure 3.3 shows the gas surface density (in $\log \text{g cm}^{-2}$) in the inner 200×200 AU box when the disk age is only 800 yr. The red circle in the coordinate center represents the sink cell. Several fragments have already formed by this time. This fragmentation timescale is longer than that found by Clark et al. (2011a) and Greif et al. (2011), who used sink cells with a smaller radius of 1.5 AU, but is comparable to the fragmentation timescale found by Smith et al. (2012a), who used larger sink cells (20 AU). We note that our core is initially of lower density and angular momentum than in those studies, which may act to increase the disk fragmentation timescale in our simulations.

Figure 3.4 presents a series of images of the gas surface density ($\log \text{g cm}^{-2}$) for the inner 1000 AU^2 . The time elapsed since the formation of the central star is indicated in each panel. We note that the whole computational domain extends to roughly 80000 AU (exactly, 0.4 pc) but that we focus on the innermost regions where the disk forms around the central protostar. The number of fragments present in the disk varies with time, indicating that they are not long lived, either migrating onto the star or being dispersed. In both cases, gravitational torques from spiral arms and/or other fragments are responsible. However, new fragmentation episodes take place because the disk is constantly supplied with material from the parent core. Most of the fragments form in the intermediate and outer disk regions, in agreement with numerical models of disk evolution in the present-day universe (e.g., Stamatellos & Whitworth, 2008; Clarke, 2009).

The recurrent character of disk fragmentation is evident in Figure 3.6 in which we plot

²The top row has a spatial scale of 1000×1000 AU, while the bottom row has a scale of 1400×1400 AU.

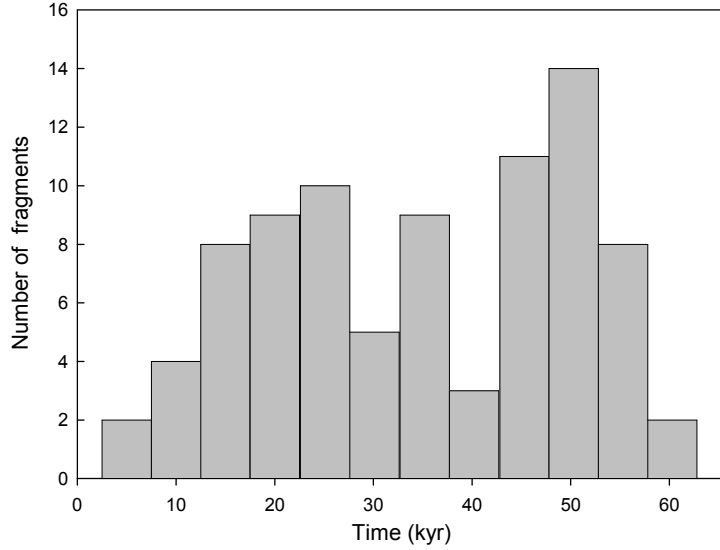


Figure 3.6: Number of fragments in the disk at a given time, as seen in the reference model.

the number of fragments N_f present in the disk with time. N_f increases steadily to 10 by $t = 25$ kyr, and then suddenly decreases by $t = 30$ Myr to $N_f = 5$, suggesting that half of the fragments have migrated or been dispersed in just 5 kyr. This is followed by a period of intense fragmentation followed by another rapid depletion during the subsequent 10 kyr. During the most vigorous episode of disk fragmentation the number of fragments in the disk peaks at $N_f = 14$ at $t = 50$ kyr. This fragmentation burst is followed by a deep minimum when the number of fragments drops to just $N_f = 2$. It is important to note that N_f never drops to zero, suggesting that some of the fragments may not migrate inward but instead stay at quasi-stable wide orbits or even migrate outward as also found in recent studies by Clark et al. (2011a) and Greif et al. (2011).

The consecutive increases and declines in the number of fragments suggests that the disk approaches a limit cycle during which periods of vigorous disk fragmentation are followed by periods of relatively weak (to no) fragmentation. This limit cycle behavior is possible if the typical migration time scale of the fragments is shorter than the characteristic time required for disk loading of material infalling from the collapsing parent core. The disk therefore loses mass (via inward migration of the fragments onto the star) faster than it can be replenished via accretion from the parent core. Following significant mass loss, the disk stays relatively dormant until sufficient mass is accumulated to trigger another burst of fragmentation.

For a mass infall rate onto the disk of $\dot{M}_{\text{disk}} \approx 10^{-3} M_{\odot} \text{ yr}^{-1}$ and disk mass $M_{\text{disk}} \approx 10 M_{\odot}$ (see Figure 3.9), the characteristic timescale for disk mass loading is

$$t_{\text{load}} = \frac{M_{\text{disk}}}{\dot{M}_{\text{disk}}} \approx 10 \text{ kyr}. \quad (3.10)$$

The migration timescale t_m estimated for fragments in the reference model lies in the range of $10^3 - 7 \times 10^4$ yr, with most fragments having migration times of just a few thousand years (see Table 3.3 and equation [3.13]). Hence, the mean migration time is indeed shorter than the characteristic mass loading time. It is worth noting that t_{load} is in approximate agreement with the temporal variability of 5 – 15 kyr over which peaks in the distribution of fragment numbers occur in Figure 3.6.

To illustrate the effect of gravitational fragmentation, regions in which the Toomre Q -parameter fall below unity are plotted in Figure 3.5 (traced in black). The Q -parameter is defined as $c_s \Omega / \pi G \Sigma$. Evidently, all fragments are characterized by $Q < 1$. In addition, some parts of the spiral arms are also characterized by $Q < 1$ but do not yet show signs of fragmentation. Indeed, the number of fragments at $t = 40$ kyr (right-hand panel) is greater than at $t = 45$ kyr (left-hand panel), indicating that new episodes of disk fragmentation took place during the intervening period. We note that the Q -parameter in the innermost 50 AU is greater than unity, which explains the stability of this region to gravitational fragmentation.

The left-hand column of Figure 3.7 presents the gas surface density distributions calculated along the radial cuts shown schematically by yellow dashed lines in the upper-left panel of Figure 3.4 ($t = 30$ kyr). Each cut has an angular width of 15° , and is centered on the peak density of the fragment and its surrounding mini-disk. The gas surface density is averaged over the grid zones that are overlaid by the cut and have the same radial distance. The top, middle and bottom rows correspond to cuts 1, 2, and 3, respectively. The positions of the fragments are indicated by arrows. The characteristic $r^{-1.5}$ slope is shown as a dotted line for convenience. Evidently, the radial profile of the gas surface density scales as $\Sigma \propto r^{-1.5}$, which is typical for self-gravitating disks in present-day star formation (e.g., Vorobyov & Basu, 2007, 2009). The typical gas volume density averaged over the azimuthal angle is a few $\times 10^{14}$ cm^{-3} at $r = 10$ AU and it drops to about a few $\times 10^{11}$ cm^{-3} beyond 100 AU. These values are in reasonable agreement with three-dimensional numerical hydrodynamics simulations of disk formation around primordial protostars (Clark et al., 2011a).

The right-hand side column in Figure 3.7 presents the gas surface density distributions (solid lines) and normalized gravitational torques (dashed lines) calculated along the azimuthal cuts passing through each of the fragments. One such cut is shown by the red dashed curve in the upper-right panel of Figure 3.4 for illustration. The width of the cuts is 10 grid zones, which, depending on the radial position, translates into a radial width of 15 – 55 AU. The gravitational torque is calculated as $\tau = -m \partial \Phi / \partial \phi$, where m is the gas mass in the cell at coordinate (r, ϕ) . The gas surface density and integrated torque are averaged over the grid zones that are overlaid by the cut and have the same radial distance.

Figure 3.7 shows that the gas surface density in fragments is higher by about two orders

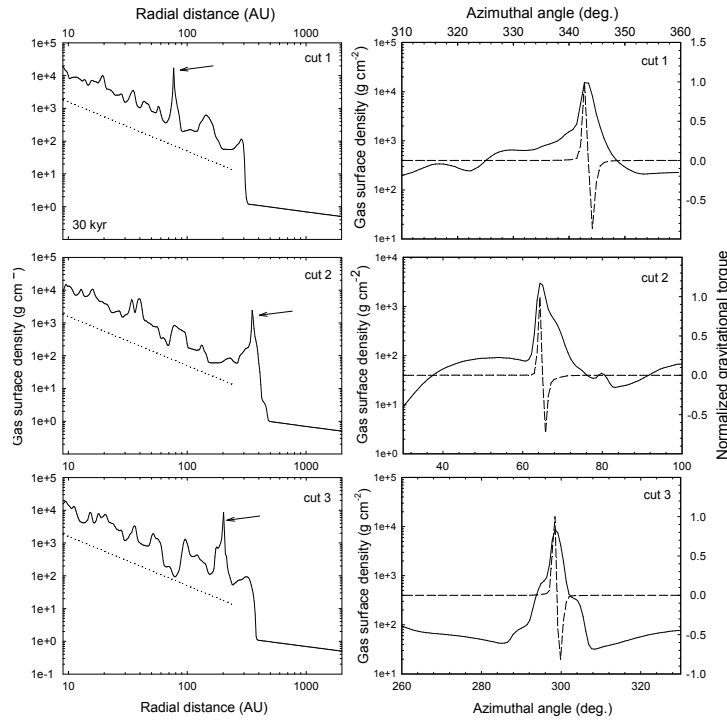


Figure 3.7: **Left column:** Radial gas surface density profiles calculated along the radial cuts passing through several individual fragments shown in Figure 3.4 by yellow dashed lines. The number of the corresponding cut is indicated in each panel. Arrows point to the radial position of the fragments. The dotted lines show an $r^{-1.5}$ radial profile for comparison. **Right column:** The azimuthal profiles of the gas surface density (solid lines) and normalized gravitational torque (dashed lines) calculated along the azimuthal cuts passing through the same fragments. One of these cuts is shown schematically in Figure 3.4 by the red dashed curve.

of magnitude as compared to local disk values. The behavior of the normalized gravitational torque is interesting in that it exhibits a steep rise to a maximum positive value on the leading part of the fragment (greater azimuthal angles) and a deep drop to a minimum negative value on the trailing part (smaller azimuthal angles). The absolute value of τ is several orders of magnitude lower everywhere else. This specific form of τ in profile is caused by tidal forces acting on the fragment from the rest of the disk and, in particular, from the spiral arms within which the fragments are usually nested. The trailing part of the arm (with respect to the fragment) exerts a negative gravitational torque and pulls the fragment back, while the leading part of the arm exerts a positive torque and pulls the fragment forward in the direction of rotation. The resulting tidal force tends to shear apart the fragment, but the fragment's own self-gravity prevents it from dispersing.

To calculate the properties of the fragments, we designed an algorithm that located the fragments in the disk and calculated their mass M_f , maximum surface density Σ_{\max} , physical and Hill radii, R_f and R_H , mass within the Hill radius M_H , radial distance of the fragment r_f ,

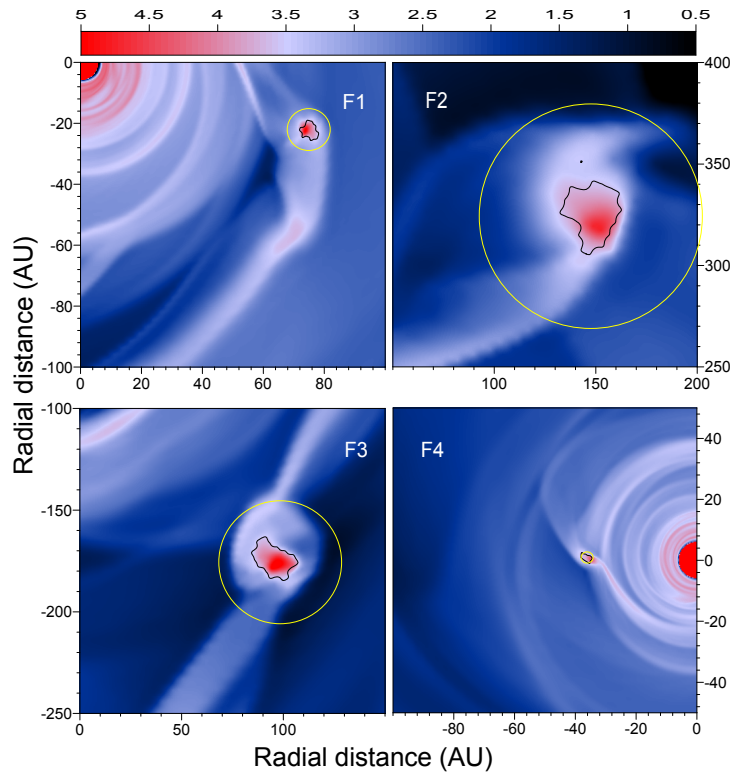


Figure 3.8: Zoom-in images of four typical fragments present in the disk at $t = 30$ kyr in Figure 3.4. Fragments F1-F3 are named after the radial cuts that pass through the corresponding fragments, while fragment F4 is indicated by the arrow. The black contour lines delineate the fragments as determined by our fragment-tracking algorithm, while the yellow line outlines the Hill radius. The scale bar is in $\log \text{g cm}^{-2}$.

and the integrated gravitational torque acting on the fragments τ_f . In particular, the Hill radius is

$$R_H = r \left(\frac{M_f}{3(M_f + M_*)} \right)^{1/3}, \quad (3.11)$$

where M_* and M_f are the masses of the star and fragment, respectively. The radius of the fragment R_f is calculated from the known area occupied by the fragment, assuming a circular shape. Additional details of the tracking algorithm are described in the Appendix.

Figure 3.8 presents zoomed-in gas surface density maps of four typical fragments. Fragments F1-F3 are named for the radial cuts denoted by the yellow dashed lines passing through the corresponding fragments in Figure 3.4. Fragment F4 is marked in Figure 3.4 by the arrow. Fragment positions, as determined by our fragment-tracking algorithm, are outlined in black, and their properties listed in Table 3.3.

All of the individual fragment radii R_f are smaller than their respective Hill radii R_H (see Figure 3.8), indicating that the fragments are gravitationally bound objects. Fragment masses

M_f lie in the range $0.02 - 0.38 M_\odot$. As the mass located within the Hill radius M_H is always greater than M_f , the excess material can be interpreted as a minidisk. The presence of minidisks is most evident around fragments F1-F3 in Figure 3.8. Fragment F4 is interesting in that its radius is nearly equal to the Hill radius, which is a manifestation of tidal stripping; it is also the least massive of the four fragments. In general, the closer the fragment is located to the central protostar, the smaller its radius and mass.

The orbital dynamics of the fragments depends on the sign of the integrated gravitational torque acting on them. As indicated from the data in Table 3.3, all of the fragments in Figure 3.8 migrate inward. We note that occasional outward migration of the fragments as a result of N-body-like gravitational scattering was also found in our models. The migration time scale can be estimated as follows. A (small) change in the angular momentum of a fragment (mass M_f) on a Keplerian orbit, due to a (small) change in the orbital distance of the fragment dr_f can be written as $dL = \frac{1}{2}M_f v_f dr_f$, where $v_f = (GM_*/r_f)^{1/2}$. The migration velocity of the fragment is then

$$v_m = \frac{dr_f}{dt} = \frac{2 \frac{dL}{dt}}{M_f v_f}. \quad (3.12)$$

Noticing that $dL/dt = \mathcal{T}$, where the latter quantity is calculated as the sum of all individual gravitational torques τ acting on the fragment, the characteristic migration time is

$$t_m = \frac{r_f}{v_m} = \frac{L}{2\mathcal{T}}. \quad (3.13)$$

The estimated migration time scale from each fragment is listed in Table 3.3. Fragment F4 and F2 have the shortest/longest migration time scales, of 10^3 yr and 7×10^4 yr, respectively. We note that these values are instantaneous migration time scales, and that their migration patterns may change as more envelope material accretes on to the disk. Nevertheless, these migration time scales indicate that most of the fragments that are seen in the disk at $t = 30$ kyr will eventually have migrated onto the forming protostar by the end of our simulations, at $t = 55$ kyr. The number of fragments in Figure 3.4 does not steadily decline in time because subsequent generations of disk fragmentation continue to be fuelled by mass loading from the infalling envelope (e.g., at $t = 50$ kyr).

Ultimately, fragments that survive tidal stripping and/or shearing will pass through the inner boundary of the simulation, after which the evolution may branch into one of two possibilities. If the fragment survives tidal stripping and shearing, it may settle into a close orbit and form a low-mass companion close to the central star. Alternatively, the fragment may merge with or be tidally destroyed by the central star, releasing its gravitational energy in the form of a strong luminosity outburst. The latter possibility has been suggested by the recent numerical

Table 3.3: Fragment Characteristics

Fragment	M_f (M_\odot)	M_H (M_\odot)	R_f (AU)	R_H (AU)	Σ_{\max} (g cm^{-2})	T_{\max} (K)	r_f (AU)	τ_f ($\text{g cm}^2 \text{s}^{-2}$)	t_m (yr)
F1	0.08	0.1	3.5	7.3	1.3×10^5	1890	77	-13.2	4.1×10^3
F2	0.38	0.54	23.0	56.1	1.7×10^4	1800	352	-3.0	7×10^4
F3	0.35	0.46	12.0	31.1	6.2×10^4	1860	202	-11.4	1.3×10^4
F4	0.02	0.02	1.83	2.0	3.0×10^4	1840	35	-2.9	10^3

Torque τ_f is in factors of 8.6×10^{40} .

hydrodynamics simulation of Greif et al. (2012). We consider this phenomenon in more detail below.

3.3.3 Accretion and Luminosity Bursts

Temporal evolution of the mass accretion rate in the reference model is shown in the top panel of Figure 3.9, from the disk onto the protostar (solid line), together with the smoothly varying accretion rate of material from the envelope onto the disk at 3000 AU (dashed line). The formation of the protostar is marked by the sharp peak in the mass accretion rate; we fix this point as $t = 0$ and count time forward from here. The protostar then accretes material from the immediate surrounding envelope at the rate of a few times $10^{-3} M_\odot \text{ yr}^{-1}$, growing to $6.0 M_\odot$ within approximately 2 kyr. At this point the accretion is temporarily halted by the formation of a quasi-Keplerian disk.

Accretion quickly resumes as the disk grows in mass and the influence of gravitational torques acting within the disk continues to redistribute matter and angular momentum. We calculate the mean accretion rate in 1000 year intervals following the formation of the quasi-Keplerian disk, finding \dot{M} to decline steadily from approximately 10^{-3} to $10^{-4} M_\odot \text{ yr}^{-1}$ over the course of the simulation. However, this smoothed background of accretion is punctuated by significant burst events during which clumps of typically $\sim 0.03 M_\odot$ in size are accreted on time scales of less than 100 yr (e.g., fragment F4 in Figure 3.8). A select few individual burst events involve the accretion of clumps of $\sim 1.0 M_\odot$. This results in effective mass accretion rates of $\sim 10^{-1} M_\odot \text{ yr}^{-1}$, with the most extreme rates as high as $1.0 M_\odot \text{ yr}^{-1}$. Such large fluctuations in the accretion rate are the characteristic signature of gravitationally-induced fragmentation

within the disk, and subsequent accretion of the fragments onto the protostar.

The cumulative effect of these two disparate modes of accretion are summarized by the mass growth curves in the middle panel of Figure 3.9. The protostar mass (solid line) grows rapidly over ~ 5 kyr during an initial phase of smooth accretion, continuing to increase steadily thereafter. However, the burst mode of accretion is also evident through abrupt increases in mass, of a few M_\odot at a time. These increases are typically followed by plateaus during which the mass of the protostar changes very little while the disk equilibrates back into a quasi-Keplerian state. Each burst event is also mirrored by a corresponding decrease in the total disk mass (dashed line). Overall however, the disk mass continues to increase due to the accretion of material from the remnant parent cloud core.

An object's luminosity during the early stages of protostellar evolution can be effectively characterized by the accretion luminosity alone. This is estimated by the dissipation of kinetic energy from infalling disk material landing on the protostellar surface:

$$L_{\text{acc}} = \frac{GM_*\dot{M}}{2R_*}, \quad (3.14)$$

where M_* is the mass of the protostar, \dot{M} is the accretion rate from the disk, and R_* is the protostellar radius. To determine R_* in the absence of a detailed model for the stellar interior, we adopt the evolutionary model of Omukai & Palla (2003), and following Smith et al. (2012a), employ simple power-law approximations for the protostar radius during each phase of its evolution.

Following the initial collapse of the cloud core, Stahler et al. (1986) showed that the protostellar radius grows according to a mixed power-law of the form $R_* \propto M_*^{0.27} \dot{M}_{-3}^{0.41}$; for notational convenience we use \dot{M}_{-3} to denote the ratio of the actual mass accretion rate \dot{M} to the fiducial value of $10^{-3} M_\odot \text{yr}^{-1}$ (Omukai & Palla, 2003). However, this growth is exacerbated once the internal temperature of the protostar rises sufficiently to drive a wave of luminosity outward from the core. The result is a sudden and rapid expansion of the stellar surface. Once this wave reaches the surface of the star itself, the interior is able to relax, and the protostar begins Kelvin-Helmholtz contraction toward the main-sequence. The following power-law relations therefore approximate the evolution of R_* through these distinct phases, as well as the transitions between them (Smith et al., 2012a):

$$R_* = \begin{cases} 26 M_*^{0.27} \dot{M}_{-3}^{0.41}, & M_* \leq M_1 \\ A_1 M_*^3, & M_1 \leq M_* \leq M_2 \\ A_2 M_*^{-2}, & M_2 \leq M_* \text{ \& } R_* < R_{\text{ms}} \end{cases}. \quad (3.15)$$

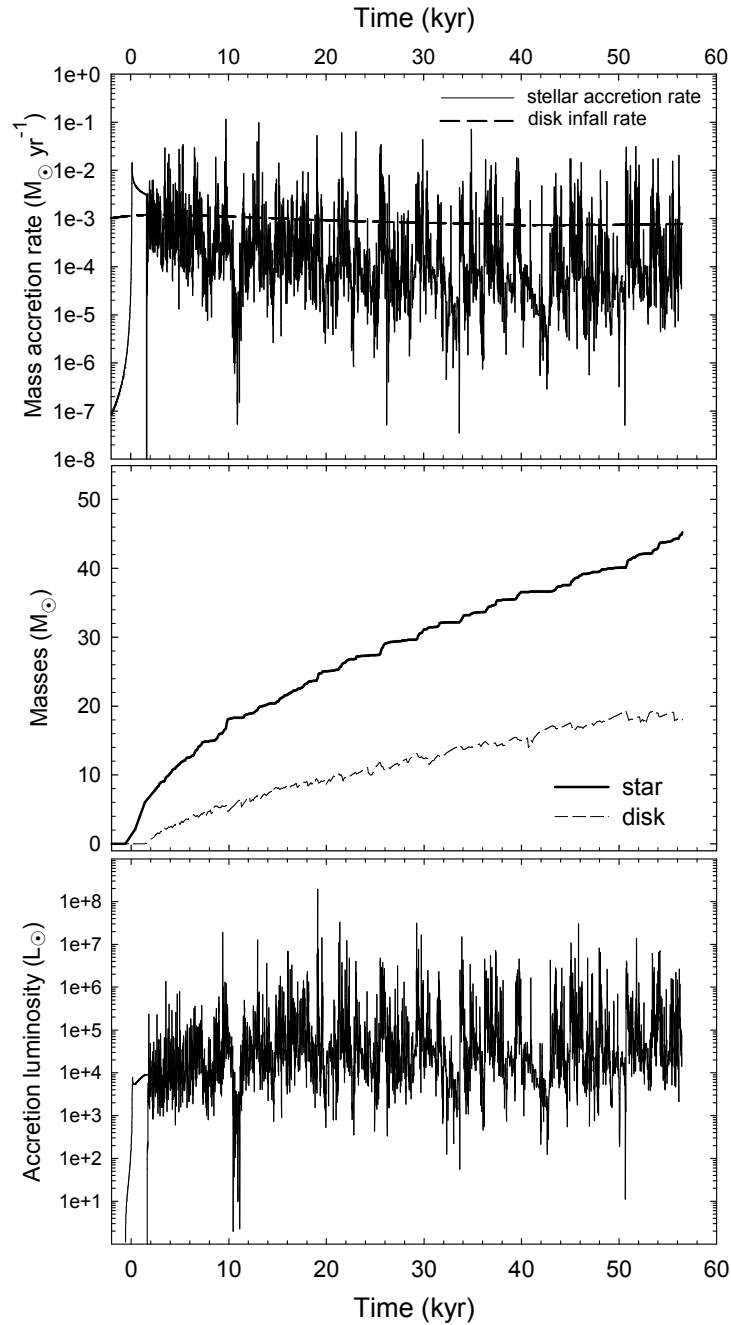


Figure 3.9: **Top:** Mass accretion rates, from the disk onto the central protostar (solid), and from the remnant cloud core onto the disk at 3000 AU (dashed). **Middle:** Temporal evolution of the masses of the protostar and its disk. Punctuated increases in the protostar mass, associated with burst events, correspond to the momentary decreases in disk mass. **Bottom:** Accretion luminosity associated with the mass accretion rate onto the protostar.

The constants A_1 and A_2 are matching conditions that ensure the functional form of R_* remains smoothly varying during the transitions.

The mass parameter M_1 marks the transition between the adiabatic phase of growth and the arrival of the luminosity wave at the protostellar surface; M_2 , the transition between the luminosity wave driven expansion and subsequent Kelvin-Helmholtz contraction. M_1 and M_2 are fixed by the instantaneous mass accretion rate as the protostar transitions between phases, and are defined as

$$\begin{aligned} M_1 &= 5\dot{M}_3^{0.27}, \\ M_2 &= 7\dot{M}_3^{0.27}. \end{aligned} \tag{3.16}$$

Although this model was originally developed under the assumption of a constant mass accretion rate, evolution of the interior can be assumed to occur roughly adiabatically due to the long cooling time of the protostellar interior. As a result, significant rapid variability in R_* is not expected while the Kelvin-Helmholtz time scale is much longer than the accretion time scale.

The bolometric accretion luminosity L_{acc} for our reference model is presented in the bottom panel of Figure 3.9. L_{acc} reaches a value on the order of $10^4 L_\odot$ almost immediately at the time the protostar is formed, and continuing to vary slowly about this level over the course of the simulation, typical for protostars of primordial composition (e.g., Smith et al., 2012b). After the disk is formed at $t = 2$ kyr, the accretion luminosity demonstrates a highly variable pattern of behavior with high-intensity bursts (up to $10^7 L_\odot$) superimposed on the lower baseline value ($\sim 10^4 L_\odot$). This highly variable luminosity may have important consequences for the disk evolution, but more accurate numerical simulations taking into account the heating/cooling balance are needed to assess this effect.

Spiral arms are formed when the destabilizing effects of self-gravity become comparable to, or dominate over, the stabilizing effects of pressure and shear. If the Toomre Q -parameter within the arm drops below unity, sections of the arm may collapse to form bound fragments. The accretion bursts occur when these fragments are driven onto the protostar by the gravitational torques of the spiral arms and/or other fragments. The temporal evolution of Q and the integrated torque \mathcal{T} can be used to illustrate this phenomenon, with Q serving as an approximate stability criterion, and \mathcal{T} roughly expressing the efficiency of angular momentum and mass redistribution by spiral inhomogeneities within the disk (Vorobyov & Basu, 2006). As we are interested in the global properties of the disk (instead of their local variations), we calculate an approximate global value of $Q = \tilde{c}_s \Omega / (\pi G \Sigma)$, averaging \tilde{c}_s , Ω , and Σ over all of the computational grid zones of the inner 500 AU region within which the disk is localized. The quantity $\tilde{c}_s = (dP/d\Sigma)^{1/2}$ is the effective sound speed.

Figure 3.10 presents the mass accretion rate onto the protostar (in black) and the integrated

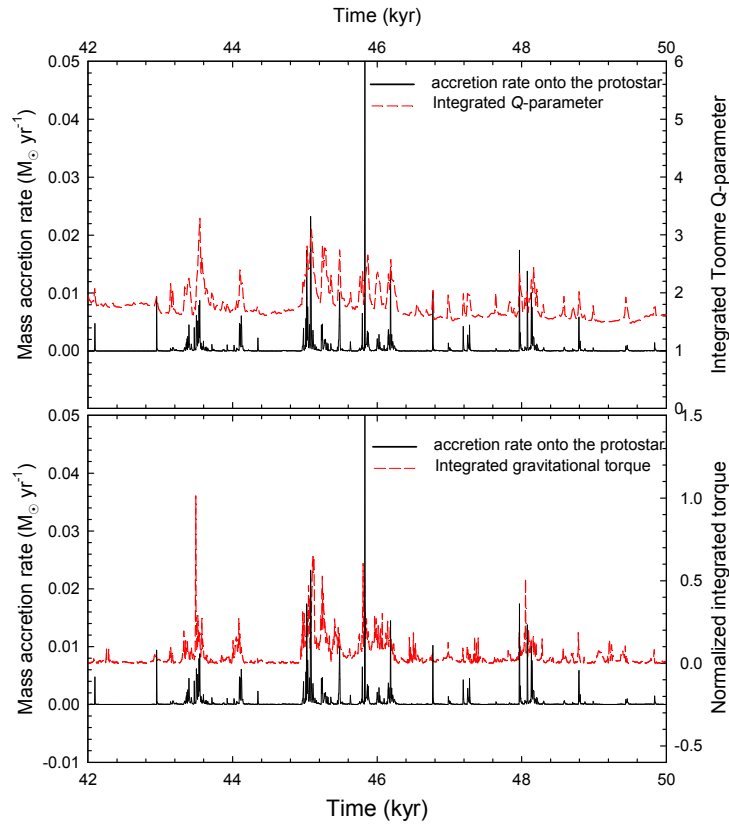


Figure 3.10: **Top:** Mass accretion rate onto the protostar (black solid line) and the global Toomre Q -parameter (red dashed line) versus time elapsed since the formation of the protostar. **Bottom:** Mass accretion rate onto the protostar (black solid line) and the integrated gravitational torque by absolute value (red dashed line) versus time. See text for an explanation of the interdependence between these quantities.

gravitational torque normalized to a local maximum value (in red) as a function of the time elapsed since the formation of the protostar from our reference model. We focus on a short period of the evolution in order to make the interdependence between the bursts, integrated torque, and Q -parameter clearly visible. For the same reason, we also plot the mass accretion rate on a linear scale here. The red line shows that Q is smallest just before a burst, and its value rises sharply afterward, reflecting a transient decrease in the disk mass caused by fragments passing through the inner computational boundary. The integrated torque grows before each burst, reaching a maximum value at the moment of the burst itself due to strong gravitational interaction between spiral arms and fragments as the latter are torqued onto the protostar. After the burst, the integrated torque returns to a marginal value. We note that the Q -parameter in Figure 3.10 does not explicitly drop below unity—a typical value for gravitational fragmentation—because of the averaging over the entire disk; local values of Q (Figure 3.4) do drop below unity in the densest parts of the spiral arms and in the fragments.

3.3.4 Parameter space study

We next consider two additional models with the purpose of exploring the robustness of the accretion and luminosity burst phenomena. We choose primordial cores with a lower initial angular momentum (Model 1) and another with a higher initial temperature (Model 2) than in our reference model. These choices are motivated by numerical studies of the burst phenomenon in present-day star formation that have shown both the number and intensity of such bursts to diminish with decreasing angular momentum and increasing temperature of the parent core (Vorobyov & Basu, 2010). The specific parameters of each model are listed in Table 3.2.

Figure 3.11 presents the mass accretion rates (top row), disk and stellar masses (middle row), and accretion luminosity (bottom row) for Model 1 (left column) and Model 2 (right column). We terminate the simulations when the mass of the central objects reaches $45 M_{\odot}$. Although the burst phenomenon is still occurrent, the strength of the accretion and luminosity bursts is somewhat lowered in comparison with our reference model. Though some of the luminosity bursts exceed $10^7 L_{\odot}$ in the reference model, in Models 1 and 2 most of the bursts stay between $10^6 - 10^7 L_{\odot}$.

The apparent decline in the strength of the bursts in Model 1 is caused by a notable decrease in the corresponding disk mass as compared to the reference model. Model 1 is characterized by a factor of four smaller ratio of the rotational to gravitational energy β than in the reference model, which leads to a delayed formation of the disk and overall lower disk mass. Low mass disks are less prone to gravitational fragmentation than their high mass counterparts, and the masses of their fragments are correspondingly lower. The solid line in the middle-left panel

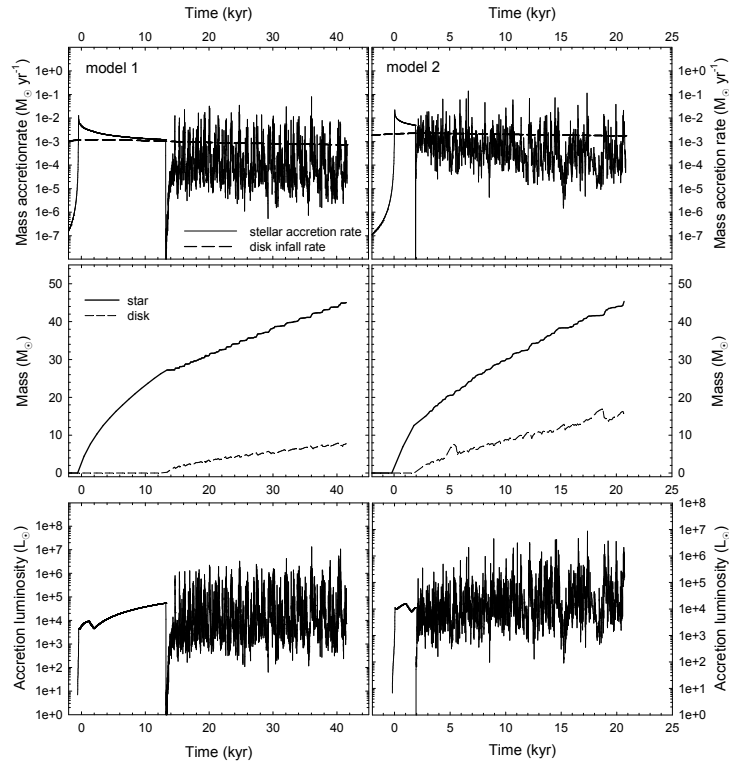


Figure 3.11: Mass accretion rates (top row), disk and stellar masses (middle row), and accretion luminosity (bottom row) versus time elapsed after the formation of the protostar for Model 1 (left column) and Model 2 (right column). The solid lines in the top row show the mass accretion rate onto the protostar, while the dashed lines yield the mass infall rate at 3000 AU. The solid and dashed lines in the middle row are the masses of the protostar and the disk, respectively.

in Figure 3.11 indicates that the typical mass of the accreted fragments in Model 1 does not exceed $1.0 M_{\odot}$, whereas in the reference model the fragments are of a few solar masses by the time they are accreted onto the protostar. This explains the somewhat weaker strength of the bursts in Model 1.

Model 2 has a higher initial temperature ($T = 350$ K) and hence a higher disk temperature (because of the adopted polytropic equation of state) than the reference model ($T = 250$ K). For instance, the gas temperature at $r = 100$ AU in model 2 at $t = 30$ kyr is approximately 1500 K, while in the reference model it is ≈ 1100 K. The contrast becomes stronger closer to the protostar. High temperature disks are also less prone to gravitational fragmentation because they have a higher Toomre Q -parameter than their low temperature counterparts. This effect is somewhat offset by a higher mass infall rate onto the disk as indicated by the dashed lines in Figure 3.11. As a result, the variations in accretion and luminosity in Model 2 are of smaller amplitude than in the reference model, but the burst phenomenon is still well pronounced. We also ran a model with a factor of 1.5 smaller initial core mass than that of the reference model but similar β , which yielded essentially similar results to those of Model 1. Obviously, models with increased β and/or M_c that would yield an even more intense profile of bursts are not considered here. We conclude that the accretion and luminosity bursts are a robust phenomenon, which is expected to occur for a range of initial primordial core masses, angular momenta and temperatures.

3.4 Discussion

Our parameter study successfully demonstrates the robustness of the burst accretion phenomenon across a wide range of configurations in mass, rotation rates, and temperatures. We find the formation of a quasi-Keplerian disk to be the outcome of the gravitational collapse of primordial prestellar cores. The disk expands quickly in radial extent to several hundred AU within just a few kyr of the formation of the central protostar. In agreement with Clark et al. (2011a), as has been found in studies of present day star formation (e.g., Vorobyov & Basu, 2007), we find that the disk exhibits a near-constant Toomre Q parameter ~ 1 . Figure 3.11 demonstrates that this is not only true initially, but holds over a substantial tract of time, ~ 80 kyr.

Studies of mass accretion during primordial star formation have focused primarily on the smooth accretion of material onto the protostar, reminiscent of Larson-Penston type analytic solutions (e.g., Omukai & Palla, 2003). Recently, Smith et al. (2012a) studied the multiplicity of fragmentation events in somewhat larger cloud cores. They found the accretion rates varied due to the motions of the protostellar fragments through regions of alternately high- and low-density gas within the natal environment, with initial accretion rates of $10^{-2} M_{\odot} \text{ yr}^{-1}$ that then

declined to $10^{-3} M_{\odot} \text{ yr}^{-1}$; in approximate agreement with analytic solutions. Indeed, we find similar mass accretion rates onto the disk of $\sim 10^{-3} M_{\odot} \text{ yr}^{-1}$. However, this source of infalling material is responsible for the mass loading of the disk and its subsequent fragmentation (Section 3.3.1), which is the ultimate origin of the variability in the actual rate of accretion onto the protostar.

The burst mode of accretion thus represents an entirely novel mechanism in contrast to either the classical analytic scenario of monolithic accretion, or that due to the motion of individual protostellar fragments. The resupply of material infalling onto the disk at large radii establishes a pattern of recurrent gravitational-instability-driven fragmentation, as has been seen in models of present-day disk evolution (e.g., Vorobyov & Basu, 2006). In analogue studies by Smith et al. (2012b) it has been noted that the number of fragmentation events actually increases steadily in time. We find a similar steady increase initially (Figure 3.7). However, SPH implementations may be limited in their ability to resolve small-scale torques that may act to shear objects apart, and long-term temporal resolution is required to resolve the variability and seeming periodicity in the rate of fragment formation observed in the simulations presented herein.

The large-amplitude variations in the mass accretion rates are also responsible for giving rise to a correspondingly large-amplitude time varying accretion luminosity (Figure 3.8). Although the accretion luminosity associated with primordial star formation is often regarded as only a mild heating source (McKee & Tan, 2008; Hosokawa et al., 2011), the nature of episodic accretion suggests that the accretion luminosity itself may exceed prior estimates by a factor of between 10 - 100 times. This may raise the profile of the heating rate due to accretion to be comparable to that from gas compression. However, our polytropic modeling of the gas thermodynamics is the primary caveat limiting our ability to analyze the complete effect of this heating mechanism on the disk's evolution. The robustness of our simulation results, with respect to higher disk temperatures however, suggest that this mechanism may be self-regulating, with increased heating due to bursts stymieing fragmentation, allowing the disk to cool, and in-turn increasing again the fragmentation likelihood.

Although most fragments are torqued inward and onto the central protostar, contributing to the luminosity bursts, several alternative fates also exist. Fragments capable of settling into stable orbits may evolve in conjunction with their hosts to form binary-pairs of first stars (e.g., Machida et al., 2008). In fact, Suda et al. (2004) has shown that the abundance patterns of at least two hyper metal-poor ($[\text{Fe}/\text{H}] < -5$) stars (Frebel et al., 2005; Caffau et al., 2011) can be explained by a unique history of mass transfer onto a first-generation low-mass binary star.

Finally, we note that several of the fragments (F2 for example, in Figures 3.4 and 3.8) are seen being ejected to substantially larger orbits as a result of N-body-like interactions.

Recent studies by Clark et al. (2011a) and Greif et al. (2011) noted similar dynamically chaotic interactions between fragments formed in those simulations. Although these fragments are most often sheared apart in the outer disk, we posit that a low-mass fragment—that is itself self-gravitating—may be ejected from the protostellar embryo as seen in simulations of present-day star formation (Basu & Vorobyov, 2012). This raises the tantalizingly possibility of a heretofore unseen population of low-mass primordial stars that may have survived into the present-day.

3.5 Model Caveats

The thin-disk approximation. The applicability of the thin-disk approximation in our models is discussed in the Appendix. Here, we want to stress three additional points. First, the aspect ratio A of the disk scale height Z to radial distance r strongly depend on the disk-to-star mass ratio ξ and consequently on the initial conditions in the primordial cores. Massive cores with high angular momentum are expected to form massive disks soon after the formation of the protostar. These disks can be characterized by high $\xi \simeq 1.0$ and, consequently, by high $A \simeq 1.0$ (Clark et al., 2011a). Our models have $\xi < 0.5$, which allows us to use the thin-disk limit. Second, the disk structure is quite irregular and the thin-disk approximation may break locally, even though it is fulfilled globally. And finally, full three-dimensional numerical simulations of present-day star formation (e.g. Machida et al., 2011) confirmed robustness of the burst phenomenon originally discovered using the thin-disk simulations (Vorobyov & Basu, 2005a, 2006). Three-dimensional simulations of primordial star formation already showed quick inward migration of the fragments on short timescales (Greif et al., 2012) and we await confirmation of the repetitive nature of the burst phenomenon on long timescales.

Barotropic equation of state. In the present study, we approximated the thermal balance of the gas using a barotropic equation of state. During the collapse of a cloud core the major heating source comes from compression and the barotropic approximation is justified. However, once star formation is underway, radiative cooling and stellar irradiation may produce a range of temperatures that cannot be explained by a simple barotropic approximation (Clark et al., 2011b). Numerical simulations of fragmenting barotropic disks seem to yield more fragments than those that take into account a detailed thermal balance (e.g. Stamatellos & Whitworth, 2009). We note, however, that the burst phenomenon in the present-day star formation, originally discovered using a barotropic equation of state (Vorobyov & Basu, 2006), was later shown to exist when more detailed thermal physics calculations were taken into account (Vorobyov & Basu, 2010).

Stellar irradiation. A burgeoning protostar may start affecting its surroundings quite early

in the evolution. For the mean accretion rate of $10^{-3} M_{\odot} \text{ yr}^{-1}$, a characteristic upper limit in our models, stellar UV irradiation becomes notable at a mass of about $M_{*} = 15 M_{\odot}$ (Smith et al., 2012a; Hosokawa et al., 2011). However, the burst mode of accretion is already well underway by this time, as seen in our fiducial model (e.g., Figure 3.9). Our parameter space study also revealed that the burst mode of accretion is also largely insensitive to changes in temperature of the gas. Indeed, Hosokawa et al. (2011) showed that for a variety of rates, mass accretion onto the central protostar was only significantly affected beyond $\sim 40 M_{\odot}$. We therefore terminate our simulations once the mass of the protostar exceeds this value, and while the effects of the stellar radiation are still minimal. Numerical simulations taking into account a more detailed thermal balance are certainly needed to assess the effect(s) of stellar irradiation on the burst phenomenon more accurately.

3.6 Conclusions

We have investigated the gravitationally-induced collapse of prestellar cores having pristine primordial gas composition, using nonaxisymmetric hydrodynamics simulations in the thin-disk limit. The gas thermal chemistry is modeled with a barotropic relation adapted from Omukai & Palla (2003). We follow these simulations, in the absence of protostellar feedback, to the point at which UV ionizing irradiation from the central star would become important (while $M \lesssim 45 M_{\odot}$). Our main conclusions are as follows:

- Recurrent gravitational-instability–driven fragmentation and accretion of the fragments is an important mechanism through which protostars accumulate mass in the early universe. This mechanism is mediated by smooth mass infall from the surrounding envelope at $\dot{M} \approx 10^{-3} M_{\odot} \text{ yr}^{-1}$. As mass is loaded onto the disk, gravitational instability eventually induces fragments to form, and these are then driven onto the protostar—resulting in \dot{M} of up to $10^{-1} M_{\odot} \text{ yr}^{-1}$ —by gravitational torques acting within the disk.
- The burst mode of accretion is sensitive to variations in the initial conditions (mass, rotation rate, and temperature) of the parent core, with the strength of bursts decreasing for decreasing β —the ratio of the magnitudes of rotational to gravitational energy—and/or increasing disk temperature T .
- We have considered cloud core masses and rotation rates that are somewhat lower than those derived from the numerical hydrodynamics simulations of collapsing primordial mini-halos (e.g. Yoshida et al., 2006; Clark et al., 2011a). Even in this case however, the burst phenomenon could not be entirely suppressed, and is expected to be more vigorous

for other possible initial conditions. We conclude that the burst mode of accretion is likely a robust phenomenon in primordial star formation.

- Accretion luminosity produced by episodic mass accretion may contribute significantly to the heating of material in the immediate vicinity of the protostar, but numerical simulations taking into account the heating/cooling balance are needed to assess this effect.
- Not all fragments eventually migrate inward and onto the protostar; some of the fragments are seen being ejected to the outer regions of the disk, in line with previous studies by Clark et al. (2011a) and Greif et al. (2011). Given the implications for low-mass primordial star formation, the likelihood for survival of these fragments needs to be studied.

Bibliography

Abel, T., Bryan, G. L., & Norman, M. L. 2000, *ApJ*, 540, 39

Basu, S. 1997, *ApJ*, 485, 240

Basu, S. & Vorobyov, E. I. 2012, *ApJ*, 750, 30

Binney, J. & Tremaine, S. 1987, *Galactic Dynamics* (Princeton University Press)

Bromm, V. & Loeb, A. 2004, *Nature*, 9, 353

Caffau, E., Bonifacio, P., François, P., Sbordone, L., Monaco, L., Spite, M., Spite, F., Ludwig, H.-G., Cayrel, R., Zaggia, S., Hammer, F., Randich, S., Molaro, P., & Hill, V. 2011, *Nature*, 477, 67

Clark, P. C., Glover, S. C. O., Klessen, R. S., & Bromm, V. 2011a, *ApJ*, 727, 110

Clark, P. C., Glover, S. C. O., Smith, R. J., Greif, T. H., Klessen, R. S., & Bromm, V. 2011b, *Science*, 331, 1040

Clarke, C. J. 2009, *MNRAS*, 396, 1066

Dapp, W. B. & Basu, S. 2009, *MNRAS*, 395, 1092

Frebel, A., Aoki, W., Christlieb, N., Ando, H., Asplund, M., Barklem, P. S., Beers, T. C., Eriksson, K., Fechner, C., Fujimoto, M. Y., Honda, S., Kajino, T., Minezaki, T., Nomoto, K., Norris, J. E., Ryan, S. G., Takada-Hidai, M., Tsangarides, S., & Yoshii, Y. 2005, *Nature*, 434, 871

Greif, T. H., Bromm, V., Clark, P. C., Glover, S. C. O., Smith, R. J., Klessen, R. S., Yoshida, N., & Springel, V. 2012, *MNRAS*, 3229

Greif, T. H., Springel, V., White, S. D. M., Glover, S. C. O., Clark, P. C., Smith, R. J., Klessen, R. S., & Bromm, V. 2011, *ApJ*, 737, 75

- Hosokawa, T., Omukai, K., Yoshida, N., & Yorke, H. W. 2011, *Science*, 334, 1250
- Kratter, K. M., Matzner, C. D., Krumholz, M. R., & Klein, R. I. 2010, *ApJ*, 708, 1585
- Machida, M. N., Inutsuka, S.-i., & Matsumoto, T. 2010, *ApJ*, 724, 1006
- . 2011, *ApJ*, 729, 42
- Machida, M. N., Omukai, K., Matsumoto, T., & Inutsuka, S.-i. 2008, *ApJ*, 677, 813
- McKee, C. F. & Tan, J. C. 2008, *ApJ*, 681, 771
- Omukai, K. & Palla, F. 2003, *ApJ*, 589, 677
- Omukai, K., Tsuribe, T., Schneider, R., & Ferrara, A. 2005, *ApJ*, 626, 627
- O'Shea, B. W. & Norman, M. L. 2007, *ApJ*, 654, 66
- Saigo, K., Matsumoto, T., & Umemura, M. 2004, *ApJL*, 615, L65
- Smith, R. J., Hosokawa, T., Omukai, K., Glover, S. C. O., & Klessen, R. S. 2012a, *MNRAS*, 3212
- . 2012b, *MNRAS*, 424, 457
- Stahler, S. W., Palla, F., & Salpeter, E. E. 1986, *ApJ*, 302, 590
- Stamatellos, D. & Whitworth, A. P. 2008, *A&A*, 480, 879
- . 2009, *MNRAS*, 400, 1563
- Suda, T., Aikawa, M., Machida, M. N., Fujimoto, M. Y., & Iben, Jr., I. 2004, *ApJ*, 611, 476
- Truelove, J. K., Klein, R. I., McKee, C. F., Holliman, II, J. H., Howell, L. H., Greenough, J. A., & Woods, D. T. 1998, *ApJ*, 495, 821
- Vorobyov, E. I. & Basu, S. 2005a, *MNRAS*, 360, 675
- . 2005b, *ApJL*, 633, L137
- . 2006, *ApJ*, 650, 956
- . 2007, *MNRAS*, 381, 1009
- . 2009, *MNRAS*, 393, 822

—. 2010, *ApJ*, 719, 1896

Yoshida, N., Omukai, K., & Hernquist, L. 2008, *Science*, 321, 669

Yoshida, N., Omukai, K., Hernquist, L., & Abel, T. 2006, *ApJ*, 652, 6

Chapter 4

The Luminosity of Population III Star Clusters

A version of this chapter has been submitted for publication to Monthly Notices of the Royal Astronomical Society.

4.1 Introduction

In the primordial constituency of the early universe, the formation of the first stars marked the end of the cosmological “dark ages” and the transition from a simple homogeneous universe to one rich with structure. These first stars (known as Population III stars) were responsible for producing the ultraviolet radiation that began the reionization of the universe (e.g., Tumlinson & Shull, 2000), and their supernovae were responsible for enriching the intergalactic medium with the first heavy elements (e.g., Miralda-Escudé & Rees, 1997; Gnedin & Ostriker, 1997; Ferrara et al., 2000).

Cosmological-scale simulations that follow both the dark matter and baryonic components of the early universe have yielded the consensus opinion that Population III stars formed in dark matter halos with masses of approximately $10^6 M_{\odot}$. These $3\sigma+$ perturbations over the background dark matter density field virialized by redshifts of $z \sim 20 - 50$ (Tegmark et al., 1997; Abel et al., 2002; Bromm et al., 2002). With few exceptions (e.g., Turk et al., 2009), these simulations suggest that the gas pooling into the halos underwent a quasi-hydrostatic contraction until they had sufficient mass to trigger runaway gravitational collapse (Abel et al., 2002; Bromm et al., 2002; Bromm & Loeb, 2004; Yoshida et al., 2006; O’Shea & Norman, 2007; Yoshida et al., 2008). These studies established the standard paradigm that the progenitor cloud cores of the first stars were most likely to have been massive and formed in relative

isolation.

In contrast, it is well understood (theoretically as well as observationally) that most star formation in the present-day universe arises from the fragmentation of molecular clouds, resulting in a multiplicity of young stellar objects being formed in close proximity to each other (e.g., Carpenter et al., 1997; Hillenbrand, 1997; Lada & Lada, 2003). Motivated by this, several recent studies have explored the fragmentary nature of primordial gas in the early universe, and have been able to resolve fragmentation in the disk-like environments surrounding the first protostars, thus challenging the standard paradigm (Stacy et al., 2010; Clark et al., 2011; Greif et al., 2011; Vorobyov et al., 2013, hereafter VDB 2013).

Clearly some ambiguity remains regarding the initial conditions and the formation mechanism(s) of the first stars. Observations will be required to accurately distinguish between the many existing theories of Population III star formation and evolution. In fact, the detection of primordial star clusters and galaxies in the early universe has already been defined as a major goal for next generation telescopes (e.g., Windhorst et al., 2006). Bromm et al. (2001) were among the first to investigate the spectral energy distribution of primordial stars theoretically. Later studies have expanded on their results to show that isolated Population III stars are likely to be too faint for detection by instruments such as the forthcoming James Webb Space Telescope, even when their fluxes are enhanced via chance gravitational lensing (Rydberg et al., 2013). Several authors have also turned their attention toward the potential of observing clusters, dwarf galaxies, and massive galaxies that contain Population III stars that may have formed at lower redshifts (i.e., $z < 10$) due to inhomogeneous metal enrichment of the intergalactic medium following the first supernovae (e.g., Ciardi & Ferrara, 2001; Scannapieco et al., 2003; Tornatore et al., 2007; Johnson, 2010; Safranek-Shrader et al., 2014).

In this paper we propose a scenario for the formation of a cluster of Population III stars. We argue that the gas pooling into the dark matter halos in which the first stars formed is subject to the Jeans criterion analogously to the fragmentation of giant molecular clouds in the present-day universe. As a result, these halos were capable of producing small clusters of first stars. Using nonaxisymmetric numerical hydrodynamics simulations, we study the gravitational-instability-driven fragmentation and accretion in the collapsing protostellar environment. The resulting burst mode of accretion is even more prominent in a Population III environment than in present-day star formation, as shown by VDB 2013. We use the calculations for individual cluster members to compile the frequency, magnitude, and luminosity of burst events for each cluster as a whole. We find that a simultaneity of accretion events can produce bursts of luminosity that are several orders of magnitude greater than the mean cluster luminosity.

The structure of this paper is as follows. In Section 2 we describe how gas that settles into

the host dark matter halos is subject to the Jeans fragmentation criterion, allowing for the formation of a cluster of first stars. In Section 3 we describe our numerical simulations (as well as our selections for the initial conditions) for the formation of each protostar, and calculate the luminosity for each of these cluster members. In Section 4 we discuss the implications of having a multiplicity of protostars simultaneously experiencing bursts of accretion, and calculate the effect this has on the luminosity of the cluster. We also discuss the implications of this phenomenon for future observational programs. Finally, in Section 5 we conclude with a brief discussion of our results.

4.2 The Case for Population III Star Clusters

The first stars are thought to have formed in dark matter halos that have collapsed and virialized by redshifts of $z \sim 20 - 50$. Low density gas ($n \lesssim 1 \text{ cm}^{-3}$) collapsing out of the primordial milieu follows into the gravitational potential well established by the dark matter, heating up adiabatically until reaching a virial temperature typically on the order of a few times 1000 K, depending on the depth of the potential. The gas to dark matter mass fraction is roughly 10%, amounting to a gas mass of between 10^4 and $10^5 M_\odot$. Numerical simulations of this collapse reveal that the gas streaming into the dark matter halo already exhibits filamentary and knotty structure as a result of the underlying morphology once present in the dark matter itself (e.g., Bromm et al., 1999; Clark et al., 2008; Greif et al., 2011). Indeed, gravity is well known to enhance such anisotropic structure during collapse (e.g., Lin et al., 1965).

The formation of H_2 cools the gas efficiently (lowering the Jeans mass) to a temperature of a few times 100 K, allowing the gas density to increase to $n \sim 10^4 \text{ cm}^{-3}$. While the imprint of substructure exists within the gas morphology, the formation of H_2 is inefficient for cooling the gas below a temperature of a few times 100 K, inhibiting further collapse. Instead, these precursor imprints of fragmentation must next undergo a slow quasi-hydrostatic contraction as they accrete additional mass (e.g., Tegmark et al., 1997; Abel et al., 2002; Bromm et al., 2002). Runaway gravitational collapse is only then triggered when the mass of these “weak clumps” exceeds the local Jeans value at this scale, being (e.g., Clarke & Bromm, 2003)

$$M_J \simeq 400 M_\odot \left(\frac{T}{300 \text{ K}} \right)^{3/2} \left(\frac{n}{10^5 \text{ cm}^{-3}} \right)^{-1/2}. \quad (4.1)$$

For example, a halo with a gas mass of $10^5 M_{\text{Sun}}$ and a 10% star formation efficiency would form a weak cluster with $\simeq 20$ members. Though this sequence of events differs slightly from that of present-day star formation, the latter also envisions a multiplicity of approximately Jeans mass fragments that form in close proximity to produce a weak or strong cluster (e.g., in

Taurus and ρ Ophiucus; Onishi et al., 1998; Johnstone et al., 2000).

These resultant massive clumps, each containing roughly $400 M_{\odot}$ of gas, are the sites of first star formation within the halo. The dynamical state of a typical clump formed in this way—its mass, physical extent, temperature, and angular momentum—are all determined by the collapse process. The initial conditions for the further contraction of these clumps are therefore relatively well constrained (e.g., Yoshida et al., 2003, 2006).

Authors such as Abel et al. (1998) have estimated that the efficiency of this fragmentation—with which the gas pooling into the dark matter halo is assimilated into high-density clumps—could vary between as little as a few percent to nearly 50%. As the larger clumps tend to retain their individuality against dispersal and/or mergers, the final evolutionary state of the halo gas is expected to be a small cluster of isolated objects (e.g., Clark et al., 2008; Turk et al., 2009; Greif et al., 2012). However, owing to lingering ambiguities about the manner in which this occurs, we adopt the definition of a “cluster” as being any association of 2+ stars forming from independent gaseous clumps that result from the subfragmentation of primordially pristine gas that has pooled into a single dark matter halo. Additionally, we concern ourselves with only the formation period during which the cluster members have masses below $40 M_{\odot}$. This allows us to assume that the predominant gas fraction within the halo is not ionized by the star formation as the cluster evolution proceeds. In fact, such conditions represent the analogue of present-day so-called “embedded” clusters, in which more than 80% of the cluster members belong to the Class II/III evolutionary phases, and the mass function of the cluster is assumed to be no longer evolving (e.g., Gutermuth et al., 2009). We also assume that each clump is able to promptly form stars within ~ 1 Myr, or roughly the lifetime of the most massive individual stars (e.g., Bond et al., 1984).

4.3 Individual Cluster Members

The clumps that emerge from the fragmentation are relatively isolated. Competition for accretion between clumps (due to protostellar crowding) and effects arising from gravitational interactions are negligibly small (e.g., Turk et al., 2009; Hirano et al., 2014). We thus model the formation and evolution of each cluster member with its own unique simulation—the initial conditions of which stem from the arguments of the preceding section. Here we provide details about the the numerical aspects of our code, our specific choices of initial conditions, and investigate the long-term behavior exhibited in a fiducially constructed model.

4.3.1 Numerical Simulations

We carry out numerical simulations of the gravitationally induced collapse of the primordial gas in 2+1D, assuming a thin-disk geometry. Our code is a modified version of that presented in Vorobyov & Basu (2005, 2006). The hydrodynamic equations are solved using a finite difference scheme with a time-explicit operator-split solution, based on Stone & Norman (1992). A thorough description of our code is presented in VDB 2013.

The mass and momentum transport equations in the thin disk limit can be expressed as

$$\frac{\partial \Sigma}{\partial t} + \nabla \cdot (\Sigma \mathbf{v}) = 0, \quad (4.2)$$

$$\frac{\partial}{\partial t} (\Sigma \mathbf{v}) + \nabla \cdot (\Sigma \mathbf{v} \otimes \mathbf{v}) = -\nabla P + \Sigma \mathbf{g}, \quad (4.3)$$

in which Σ is the surface mass density, \mathbf{v} is the velocity of the disk material, P is the vertically integrated pressure (determined assuming the disk is in vertical hydrostatic equilibrium at all times), and ∇ is the planar gradient operator. The gravitational acceleration in the plane of the disk (\mathbf{g}) includes the contribution from the protostar (once formed), from material inside the sink cell, and from the self-gravity of the disk and surrounding cloud core. All vectoral terms and quantities are understood as having only \hat{r} and $\hat{\phi}$ components in this formulation.

In order that the environment of the collapsing core accurately reflect primordial conditions, equations (4.2) and (4.3) are closed with a barotropic relation that fits the 1D core collapse simulations of Omukai et al. (2005). These include the detailed chemical and thermal processes of the collapsing gas. Additional details of our model are provided in VDB 2013.

4.3.2 Initial Conditions

The initial conditions for the radial gas surface density Σ and angular velocity Ω profiles for primordial cores are taken to be very similar to those of present-day star forming cores (e.g., Omukai & Nishi, 1998; Vorobyov & Basu, 2006; Yoshida et al., 2008; Vorobyov & Basu, 2010),

$$\Sigma = \Sigma_0 \left(1 + \left(\frac{r}{r_0} \right)^2 \right)^{-1/2}, \quad (4.4)$$

$$\Omega = 2\Omega_0 \left(\frac{r_0}{r} \right)^2 \left(\sqrt{1 + \left(\frac{r}{r_0} \right)^2} - 1 \right). \quad (4.5)$$

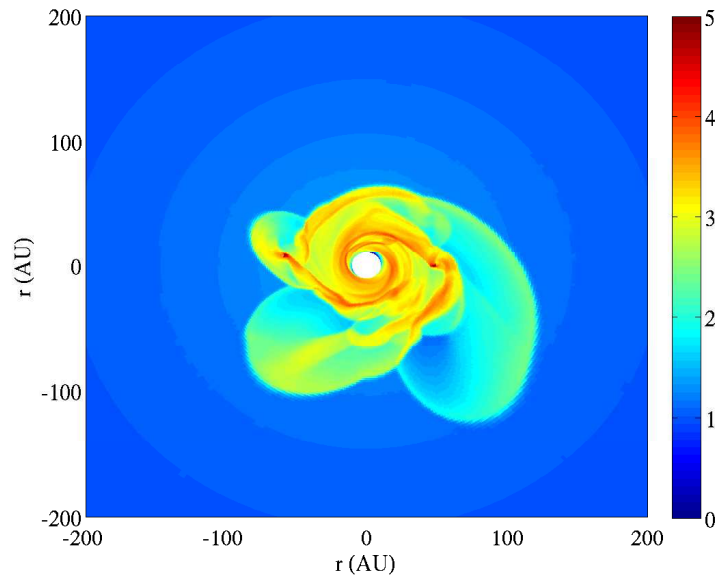


Figure 4.1: Projection of the disk surface mass density Σ in our fiducial model 1000 yr after the formation of the disk. The projected volume is 200 AU in radius, whereas the full simulation volume is 0.5 pc in radius. The white cutout region at the center of the projection is our sink cell. The colorbar is in units of $\log \text{g cm}^{-2}$. Two prominent fragments are visible on both the left and right side of the disk, at radii of ~ 70 and ~ 50 AU, respectively. The significant infall of material that continues to fall on to the disk from the surrounding cloud core is clearly visible as well.

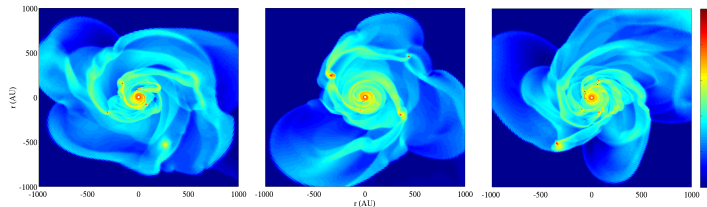


Figure 4.2: Projection of the disk surface mass density Σ within a 2000×2000 AU volume centered on the accreting protostar. The time in each frame is $t = 5, 10,$ and 15 kyr after formation of the protostar. **Left:** Some regions of the disk are Toomre-unstable, and several fragments can be identified at radii throughout the disk, between 10 and several hundred AU. **Center:** As these clumps are accreted onto the protostar or dispersed, the disk enters into a moderately quiescent period during which it is relatively stable against fragmentation. No fragments are present in the inner 300 AU of the disk. The three large fragments at radii beyond this are remnants from an earlier phase of fragmentation that had been raised to higher orbits. **Right:** Continued accretion from the parent cloud core builds up the mass of the disk, eventually triggering another period of vigorous fragmentation. The two fragments immediately to the left of the sink cell in this panel provide an example of how larger fragments can be sheared apart prior to being accreted through the sink cell, leading to intense and rapid variability in the accretion luminosity of the protostar.

The radial surface mass density profile Σ is that of an integrated Bonnor-Ebert sphere (Dapp & Basu, 2009), while the form of the initial angular velocity profile Ω corresponds to the differential rotation profile expected for a core collapsing out of a near-uniform initial surface density field (Basu, 1997).

We constrain Σ_0 by assuming a constant ratio of the radius of the outer computational boundary r_{out} to that of the centrally plateaued region r_0 : $r_{\text{out}}/r_0 \equiv 6$; so that each core has a similar initial form with $\Sigma_0 \approx 0.25 \text{ g cm}^{-2}$. The parameter r_{out} thus also determines the mass of the core, which for $r_{\text{out}} = 0.5 \text{ pc}$ is approximately $300 M_{\odot}$. These choices are constant for each of the cores simulated, and is consistent with the typical size and mass found from ab initio cosmological simulations of the collapse of primordial starless cores (e.g., Yoshida et al., 2006).

The angular momentum of the cloud core is parameterized by Ω_0 —as appears in equation (4.5)—and is related to the dimensionless parameter $\eta = (\Omega_0 r_0 / c_s)^2$ (Basu, 1997). η is related to the ratio of the rotational to gravitational energy of the cloud core, $\beta = E_{\text{rot}}/|E_g|$, with $\beta = 0.9\eta$. Finally, β relates to the so-called “spin parameter,” $\lambda = \sqrt{\beta}$, that is most often used to characterize the angular momentum of dark matter halos (and their associated gas) formed from cosmological initial conditions (e.g., Barnes & Efstathiou, 1987; Ryden, 1988). The spin parameters of each cloud core are lognormally distributed with mean $\bar{\lambda} = 0.05$ and variance $\sigma_{\lambda}^2 = 0.5$ (following Gardner, 2001; O’Shea & Norman, 2007).

Each model is run on a polar coordinate grid with 512×512 spatial grid zones in r and ϕ . The inner and outer boundary conditions allow for free outflow from the computational domain. Radial grid points are logarithmically distributed to allow for better numerical resolution toward the innermost region of the disk: the innermost cell outside of the sink region has a radius of approximately 0.1 AU and is 1.9 AU (both radially and azimuthally) at a radius of 100 AU.

Tan & McKee (2004) and Hosokawa et al. (2011) have shown that beyond $30 - 40 M_{\odot}$ the role of increasing stellar luminosity becomes critically important to understanding the subsequent evolution of these protostars, as the intensely ionizing radiation begins to inhibit H_2 formation, which is the primary coolant in the gas. We therefore terminate our simulations once the protostar reaches a mass of $40 M_{\odot}$.

4.3.3 Evolution of the Protostellar Disk

Our fiducial model is characterized as a clump of gas roughly 0.5 pc in radius, with a mass of $\sim 300 M_{\odot}$, and at a temperature of 300 K. The spin parameter λ of the clump is equal to the mean of the distribution, $\bar{\lambda} \simeq 0.05$. We follow for approximately 30 kyr the formation and evolution of the protostar and disk that results from the collapse of this object. We terminate our simulations at this point since the mass of the protostar is nearly $40 M_{\odot}$, beyond which stellar UV radiation becomes significant (Hosokawa et al., 2011). Numerical simulations that take into account a more detailed thermal balance are required to assess the effect of stellar irradiation on the burst phenomenon above this threshold. The collapsing cores we model compare well to those derived from 3D numerical simulations inside primordial mini-haloes (Clark et al., 2011; Yoshida et al., 2006). Differences are attributable to our cores being toward the lower end of the mass spectrum that has been studied by these authors.

A quasi-Keplerian disk forms around the protostar within ~ 3 kyr of the formation of the central protostar (in our fiducial model). The disk begins to fragment within a few hundred years after its formation. This timescale is somewhat longer than that found by Clark et al. (2011) and Greif et al. (2011), who used sink cells with smaller radii of 1.5 AU. However, this timescale is similar to that found by Smith et al. (2012a), who used sink cells with comparable radii of 20 AU (the central sink cell in our simulation being ~ 10 AU in radius). In Figure 4.1 we plot the disk surface mass density (in $\log g cm^{-2}$) for the inner 200 AU, 1000 years after the formation of the disk; a rich density structure exists in which several fragments are already clearly visible.

In Figure 4.2 we present three snapshots of the disk surface density inside of a 1000 AU radius and spanning 10 kyr of the disk evolution. While the left and right panels clearly de-

pict well defined condensations of gas that have fragmented out of the disk, the central panel presents an intermediary quiescent phase during which there is little to no fragmentation and the accretion of gas onto the protostar occurs relatively smoothly. The number of fragments within the disk clearly varies with time, as some fragments are tidally dispersed and others are accreted onto the central protostar; a result of the gravitational torques exerted by the fragments on each other and from larger spiral arm structures that form within the disk. Though accretion gradually drains the disk, new episodes of fragmentation are continually stimulated by the resupply of fresh gaseous material from the surrounding core envelope. It is also evident that most of the fragments are formed in the intermediate to outer disk region ($\gtrsim 50$ AU), which is consistent with the numerical simulations of disks around protostars in the present-day universe (e.g., Stamatellos & Whitworth, 2008; Clarke, 2009).

Those fragments that pass through the inner computational boundary are assumed to be readily accreted by the central protostar. Though this boundary is not the protostellar surface itself, we can use the temperature (or more appropriately, the sound speed) of the disk material along this boundary to estimate the instantaneous mass accretion rate onto the protostar as

$$\dot{M} \approx \frac{c_s^3}{G} \quad (4.6)$$

(Shu, 1977). In our fiducial model we find c_s is about 2.0 km s^{-1} . This corresponds to an instantaneous mass accretion rate of $\sim 10^{-3} M_\odot \text{ yr}^{-1}$. We note that this is just below the critical (Eddington) accretion rate of $\dot{M}_{\text{Edd}} \simeq 4.0 \times 10^{-3} M_\odot \text{ yr}^{-1}$ above which the corresponding radiation pressure alone is capable of halting the accretion flow entirely (Hosokawa & Omukai, 2009). This estimate matches the time averaged value of the mass accretion rate experienced by our model protostar (Figure 4.3), and is consistent with several other models of the runaway collapse of primordial gas as has been determined both analytically and from simulations (Omukai & Palla, 2003; Bromm & Loeb, 2004; Clark et al., 2011; Hosokawa et al., 2011; Smith et al., 2012b).

We present the complete mass accretion history for our fiducial model in the top panel of Figure 4.3. The formation of the protostar is marked by the sharp rise in the mass accretion rate, which we define as time $t = 0$. Following, material from the surrounding envelope of the progenitor cloud core continues to stream onto the protostar at a rate of a few times $10^{-3} M_\odot \text{ yr}^{-1}$. The mass of the protostar rapidly increases (within ~ 4 kyr) to approximately $15 M_\odot$ before the accretion flow is temporarily halted by the formation of a quasi-Keplerian disk.

The disk modulates the subsequent accretion of disk material onto the protostar, with gravitational torques redistributing the mass and angular momentum of the infalling cloud core

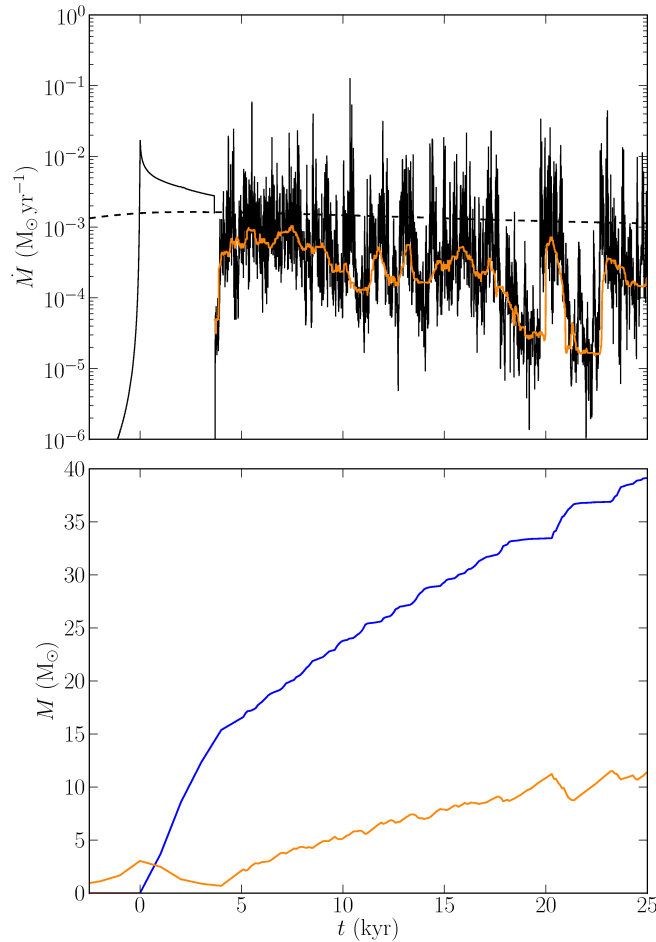


Figure 4.3: **Top:** Temporal evolution of mass accretion rates: from the cloud core onto the disk at 3000 AU (dashed black), and from the disk onto the protostar (solid black). The rectangular window time averaged mass accretion rate—the quiescent accretion rate—is in orange. **Bottom:** Growth of the protostellar (blue) and disk (orange) masses in time. The protostellar mass grows via punctuated equilibrium, while the episodic increases in the mass of the protostar are coincident with the episodes of decline in disk mass. Nevertheless, the disk mass increases with time owing to the continually replenishment of disk material from the surround core material.

material. In VDB 2013 we demonstrated that the disk self-gravity quickly induces the formation of spiral arms. Furthermore, sections of the disk in which the local value of Toomre’s Q falls below unity become subject to fragmentation (Toomre, 1964). These fragments are then torqued inward along ballistic trajectories before ultimately being accreted by the protostar, resulting in the episodic bursts of accretion (see Figure 4.3).

The cumulative effect of a quiescent mode of accretion that is punctuated by the episodic bursts is also evident in the curves of mass growth in the bottom panel of Figure 4.3. The protostellar mass (shown in blue) grows rapidly during the initial phase of smooth accretion (which lasts ~ 4 kyr). However, the burst mode of accretion comes to dominate the subsequent growth of the protostar as is evident by the abrupt increases in the protostellar mass, typically a few M_{\odot} at a time. These increases are typically followed by plateaus during which the mass of the protostar changes very little as the disk equilibrates back into a quasi-Keplerian state. Each burst event is mirrored by a corresponding decrease in the total disk mass (in orange). However, the overall mass of the disk actually continues to increase in time due to the steady accretion of material from the remnant of the progenitor cloud core (the dashed black line in the top panel of Figure 4.3).

Additional details of the effects of the gravitational torques on the disk, and the resulting recurrent character of the disk fragmentation, are discussed in VDB 2013. Here we focus on the signature of this behavior on the protostellar accretion luminosity.

4.3.4 Accretion Luminosity

A protostar’s luminosity is a product of competition between mass growth from accretion and radiative loss from the protostellar interior. However, it is not until the protostar begins contracting toward the main sequence that its internally generated luminosity L_* surpasses the accretion luminosity L_{acc} . During the earliest stages of its evolution, the source of a protostar’s luminosity is almost entirely from accretion, so that $L \approx L_{\text{acc}}$ (up to masses of $M_* \simeq 30-40 M_{\odot}$; Tan & McKee, 2004; Hosokawa et al., 2011). In VDB 2013 we showed that the large variability in accretion experienced by the protostar results in accretion luminosities several orders of magnitude greater than might otherwise be expected (compare Clark et al. 2011, Hosokawa et al. 2011, and Smith et al. 2012b to VDB 2013, for example).

We estimate the accretion luminosity assuming that any material landing on the surface of the protostar has its kinetic energy dissipated radiatively at a rate

$$L = \frac{GM_*\dot{M}}{2R_*}, \quad (4.7)$$

where R_* is the protostellar radius.

In the absence of a detailed model for the stellar interior we instead fit the evolutionary models of Omukai & Palla (2003) with a piecewise power-law approximation to the radial expansion of the protostellar surface as a function of the protostar mass. Following formation of the hydrostatic core, the protostellar radius is expected to grow according to a mixed power-law as $R_* \propto M_*^{0.27} \dot{M}_{-3}^{0.41}$; where \dot{M}_{-3} denotes the ratio of the actual instantaneous mass accretion rate \dot{M} to a value of $10^{-3} M_\odot \text{yr}^{-1}$ (Stahler et al., 1986; Omukai & Palla, 2003). Increasing temperature within the core drives a luminosity wave outward, causing a rapid expansion of the stellar surface. When this wave breaches the protostellar surface, the interior is able to relax and the protostar begins Kelvin-Helmholtz contraction toward the main-sequence.

The following relations approximate the evolution of R_* through its transitions through these phases (Smith et al., 2012a):

$$R_* = \begin{cases} 26 M_*^{0.27} \dot{M}_{-3}^{0.41}, & M_* \leq M_1 \\ A_1 M_*^3, & M_1 < M_* < M_2 \\ A_2 M_*^{-2}, & M_* \geq M_2 \text{ and } R_* < R_{\text{MS}} \end{cases}. \quad (4.8)$$

The constants A_1 and A_2 are matching conditions that ensure the functional form of R_* is smoothly varying between transitions. The mass parameter M_1 marks the transition between the adiabatic phase of growth and the arrival of the luminosity wave at the protostellar surface; M_2 , the transition between the luminosity wave driven expansion and subsequent Kelvin-Helmholtz contraction. M_1 and M_2 are fixed by the instantaneous mass accretion rate as the protostar transitions between phases, and are defined as

$$\begin{aligned} M_1 &= 5 \dot{M}_{-3}^{0.27}, \\ M_2 &= 7 \dot{M}_{-3}^{0.27}. \end{aligned} \quad (4.9)$$

Note that as the evolution of the protostellar interior occurs roughly adiabatically, due to the long cooling time therein, the variability in the accretion rate induced by the burst mode of accretion does not result in significant variability in the radius of the protostar.

The accretion luminosity calculated for our fiducial model is shown in Figure 4.4 (black). In overlay is the time averaged (i.e., quiescent) rate (L_q ; orange), and a demarcation $10\times$ greater than the quiescent rate (dashed orange). Accretion events during which L exceeds L_q by the factor of 10 are highlighted (dashed blue). Once the protostar is formed (designated as $t = 0$), L climbs very quickly to $\sim 10^4 L_\odot$. The luminosity remains at about this level during the period of smooth accretion until a disk is formed at $t \sim 4$ kyr. Although the mean rate remains at roughly $10^4 L_\odot$, the episodic nature of the subsequent vigorous accretion gives

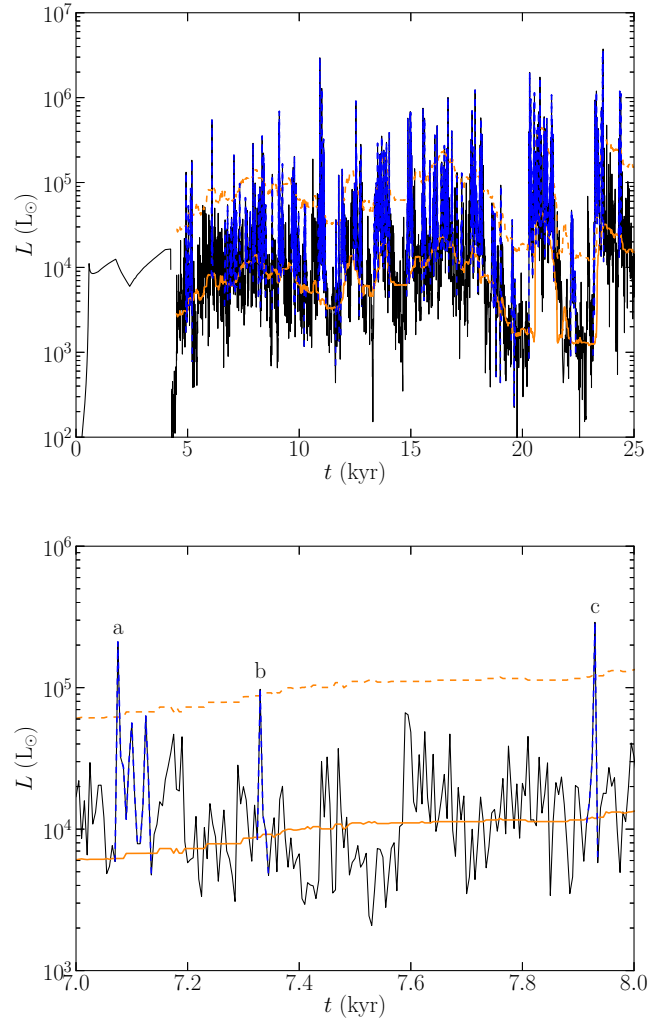


Figure 4.4: **Top:** Temporal evolution of the (accretion) luminosity from the protostar in our fiducial model (in black). In overlay is the time averaged quiescent rate (solid orange), and the $10\times L_q$ rate (dashed orange), with those accretion events whose peak luminosity exceeds this threshold highlighted in blue. **Bottom:** A zoom in on a 1 kyr window of the luminosity history for clarity. Accretion events in excess of $10\times L_q$ are clearly identified (labeled, a, b, and c, and highlighted in blue).

rise to significant variability, with some peaks reaching several times $10^6 L_{\odot}$ —two orders of magnitude greater than L_q . One might expect this large variability in luminosity caused by the individual burst events to affect the accretion flow via feedback from the enhanced radiation field. However, as the duration of the individual bursts are quite short (typically on the order of a few times 100 yr), we expect that they do not have any appreciable effect on the long-term growth of the protostar.

In the bottom panel of Figure 4.4 we focus on a 1 kyr window of our simulation in order to highlight our burst identification scheme. We calculate the effective mean accretion rate (the solid orange line) using a moving 1 kyr window. We omit luminosities within the window that are in excess of one standard deviation of the mean, then recalculate the mean again; repeating this procedure until a stable mean is found—which we then define as the quiescent luminous rate L_q . Burst events are ultimately attributable to the accretion of large individual fragments (with masses on the order of $0.1 - 1 M_{\odot}$) that form within the disk. However, these fragments are most often sheared apart into several smaller fragments, each of which is accreted by the protostar in rapid succession (VDB 2013). Hence, we include as part of a single burst event all points left- and rightward of the peak luminosity that are greater than the mean (and not only those points for which L is strictly $> 10 \times L_q$).

4.4 Clusters of Population III Protostars

As a first step to understanding the cluster luminosity in the burst scenario, we present in Figure 4.5 the (accretion) luminosity from an example cluster consisting of just two members that form within 5 kyr of each other. For simplicity within this example, the two cluster members differ only by the value of their spin-parameters λ assigned to their respective progenitor cloud cores, being $\lambda = 0.05$ and 0.065 respectively. The panels in the left-hand column present the luminosities of the individual cluster members (top- and middle-left) as well as the cumulative luminosity for the cluster as a whole (bottom-left). The histograms on the right-hand side present statistics of the fractional number distribution of burst events f_b concerning the frequency and duration of burst events, which we use as a metric for evaluating differences between the individual and cluster luminosities.

Initially the luminosity of the first cluster member to form defines the luminosity of the cluster as a whole. The second cluster member begins its evolution at $t \sim 5$ kyr (where time $t = 0$ marks the formation of the first cluster member). In the subsequent ~ 2 kyr, as the second cluster member is smoothly accreting material from its surroundings, its contribution to the total cluster luminosity increases. In fact, a significant amount of the variability in the luminosity of the first cluster member is suppressed during this period. During this time the

total cluster luminosity is consistently above $\sim 10^4 L_{\odot}$. By $t \sim 7$ kyr both cluster members harbor their own protostellar disks, and accretion onto each protostar is being driven by the action of gravitational torques in the massive disks surrounding each respective host—i.e., via the burst mode of accretion. Correspondingly, the cluster luminosity thereafter exhibits a significant amount of variability.

In the right-hand column of Figure 4.5 we present histograms of the duration of burst events exhibited by the individual cluster members, and for the cluster as a whole. The first cluster member to form exhibits a total of 73 burst events over the course of ~ 20.5 kyr—the span of time from when the disk forms to when the protostar reaches a mass of $\sim 40 M_{\odot}$ and the simulations are terminated. The mean burst duration is found to be ~ 96.3 yr. This amounts to approximately 7.0 kyr that are spent exclusively in the burst mode of accretion, with the remaining 13.5 kyr spent in quiescent phases.

The second cluster member to form naturally exhibits fewer burst events owing simply to the fact that it forms later. A total of 68 burst events are counted over the approximately 18.5 kyr during which material is actively accreting through its disk. The typical burst duration is found to be ~ 80.2 yr, for a total of ~ 5.5 kyr spent accreting via the burst mode, with the remaining roughly 13.0 kyr spent in quiescent phases.

From these durations we can conclude that the burst mode of accretion plays a significant role in the mass growth of Population III protostars. In both cases about 30% of each protostar’s individual accretion history is spent in the burst mode—that is to say that gravitational-instability–driven fragmentary accretion is responsible for one-third to one-half of the total accretion onto the first stars. This is actually a significantly higher proportion of time than has been observed in analogous simulations of present-day star formation, wherein the burst mode of accretion is thought to be responsible for only $\sim 10\%$ of a protostar’s accretion history (e.g., Vorobyov & Basu 2006, 2010; VDB 2013).

The number and frequency of the observed bursts is also affected by whether one considers each cluster member individually or simply considers the cumulative luminosity of the cluster as a whole. The first and second cluster member yield 73 and 68 burst events over 18.5 and 13.0 kyr, respectively—1 event roughly every 200 yr in both cases. The same analysis as we have performed for the individual cluster members, applied to the cluster as a whole, finds that the perceived number of burst events would be 74. This is fewer events than might be expected by a simple addition of the individual cluster members’ statistics.

The quiescent mode is clearly the dominant mode of accretion. Variations in the luminosity of any one cluster member below the quiescent rate are therefore obscured. The cluster luminosity is thus somewhat greater than might be suggested by simply summing together the individual cluster members’ quiescent luminosities. Hence, the number of burst events as

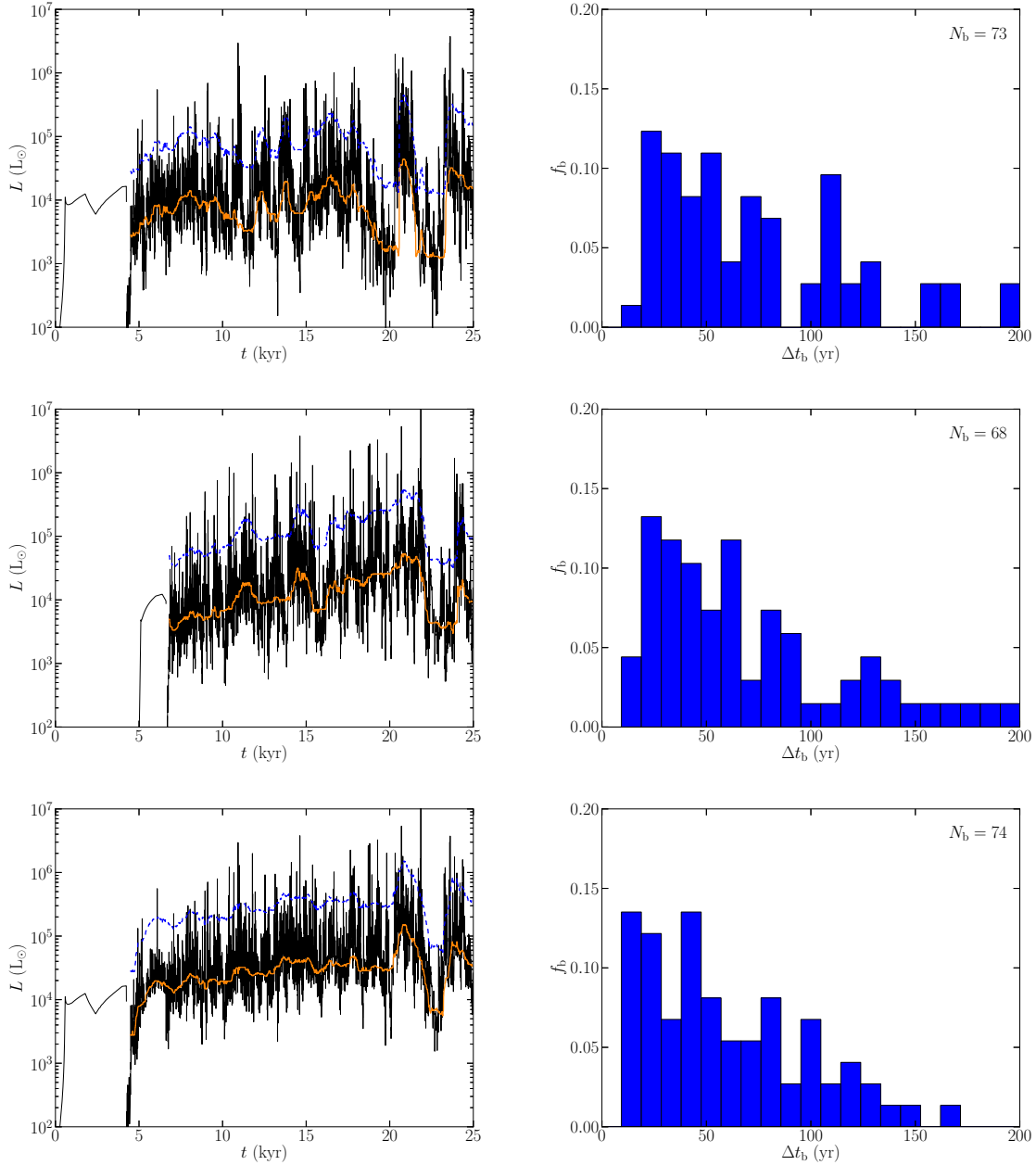


Figure 4.5: Accretion luminosity of the individual cluster members (top and middle panels) and from the cluster as a whole (bottom panel) in our example $N = 2$ member cluster. **Left:** Accretion luminosities L are plotted in black; the quiescent luminosity L_q is plotted in orange; the dashed blue line indicates a luminosity $10 \times L_q$. **Right:** Fractional number distributions (f_b) of burst durations (Δt_b) for the individual cluster members (top and middle), and for the cumulative cluster profile (bottom). The total number of identified bursts (N_b) is indicated in the upper-right of each panel. The approximate mean burst duration observed between the individual cluster members is 96.3 and 80.2 yr, for the respective individual cluster members. The mean burst duration, as extracted from the cumulative cluster luminosity profile, is ~ 72.0 years.

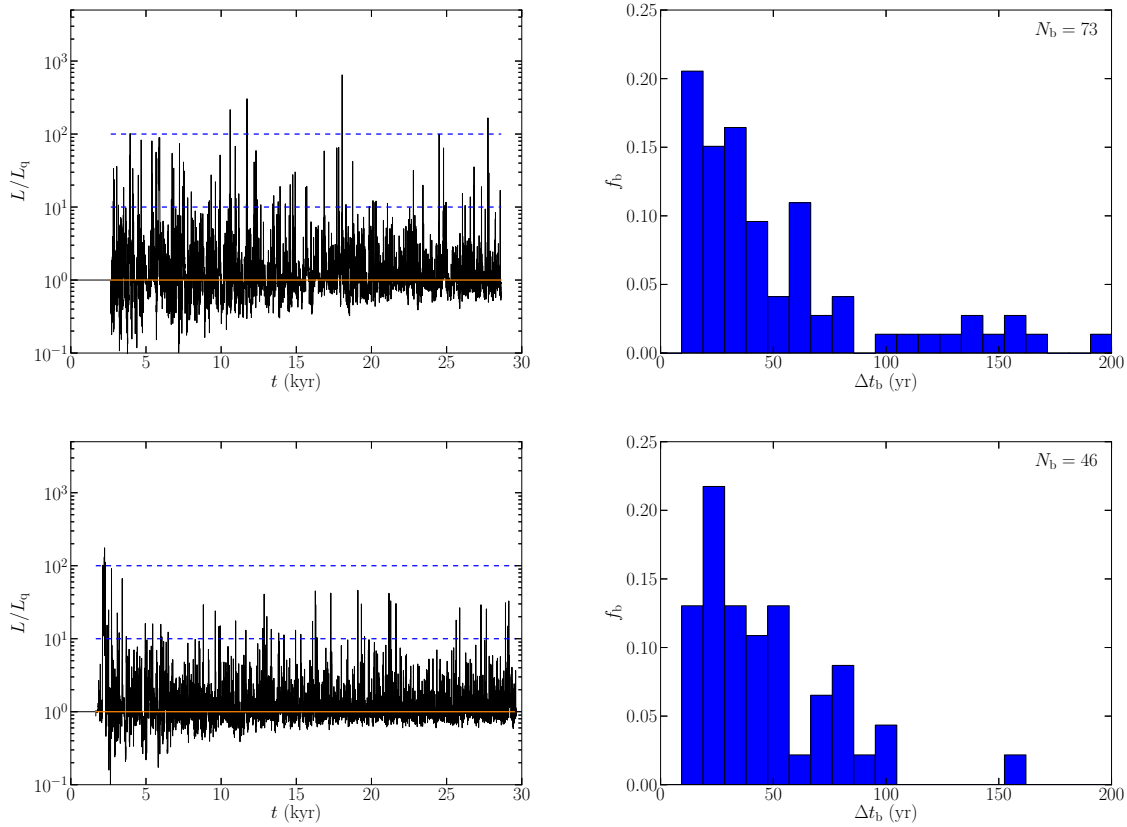


Figure 4.6: Normalized accretion luminosities (left column) and histograms of the fractional number distributions of burst durations (right column) for two additional clusters containing $N = 16$ (top), and 128 members (bottom). The dashed blue lines in each panel denote thresholds of 10 and $100\times$ the quiescent luminosity; all other lines and colors are as they appear in Figure 4.5. The normalized quiescent luminosity in each case corresponds to approximately 4×10^5 and $4 \times 10^6 L_\odot$, respectively. During the evolution of the $N = 16$ cluster a confluence of burst events at $t \approx 18$ kyr produce a particularly prominent luminous event that is $647\times$ more luminous than the cluster’s quiescent level. However, the competition between the increasing cluster quiescent luminosity L_q and the potential for such overlapping bursts is evident in the reduced magnitude of the fluctuations above L_q with increasing cluster size N . A peak is reached for $N \simeq 16$, and declines for larger N .

ascertained by examining the cluster luminosity is actually fewer than expected given the number of burst events clearly identifiable from the luminosities of the individual cluster members. Correspondingly, decreases in the cluster luminosity below a certain level of L become less likely as the number N of cluster members increases. Not only are there fewer perceived burst events, but the typical duration of the burst events is shorter, at ~ 72.0 yr, than that measured for the actual burst events occurring among the individual cluster members. This is because the quiescent cluster luminosity is greater than the quiescent luminosity of an individual cluster constituent.

In contrast, with an increasing number N of cluster members there is a distinct possibility that two or more cluster members simultaneously experience bursts. A superposition of individual increases in luminosity results in a particularly prominent increase in the cluster luminosity. In Figure 4.6 we present the normalized luminosities for two different clusters, having $N = 16$, and 128 members. Luminosities are plotted in black; quiescent cluster luminosities in orange; the dashed blue lines denote luminosity levels 10 and $100 \times L_q$. Figure 4.7 provides a summary of the time-averaged accretion luminosities from all of the clusters in this study, with $N \in \{2, 4, 8, 16, 32, 64, 128, 256, 1024\}$, for reference. As seen in Figure 4.5, with only two members, the amount of variability expressed in the cluster luminosity as a whole is comparable to that expressed by its individual members. Here, as the number N of cluster members increases, the variations in the luminosities of those constituent members will have a decreasing effect on the total cluster luminosity. Even qualitatively it is apparent in Figure 4.6 that the number of burst events in excess of a factor of $10 \times L_q$ declines with N . Figure 4.8 depicts the fractional duration of time that the $N = 16$ cluster spends at luminosities above the quiescent rate.

Figure 4.9 summarizes how these two effects compete with one other. The duration of time (as a fraction of the cluster's total star forming lifetime) that a cluster spends above a certain luminosity threshold is plotted as a function of cluster size, for $N \in \{2, 4, 8, 16, 32, 64, 128, 256, 1024\}$. The typical time frame for a burst is on the order of a few hundred years, and their frequency is largely stochastic. Therefore, the likelihood of the superposition for two or more protostars to simultaneously experience intense bursts of accretion, resulting in a massive burst, is quite low. Intuitively then, clusters with increasing numbers of members are more likely to experience such coincidences. However, each additional protostar in a cluster also contributes to increasing the mean. A balance between these effects is achieved in relatively small clusters, $N \simeq 16$, for which we find nearly 15% of the cluster's star forming period is spent at a luminosity level $10 \times$ greater than the mean rate, L_q .

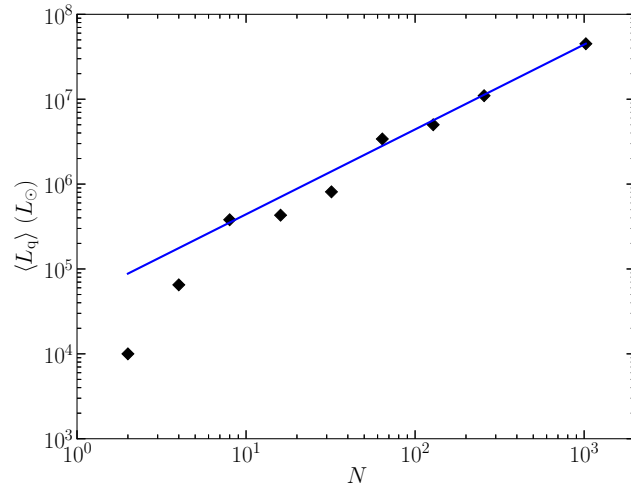


Figure 4.7: Diamond symbols denote the time-averaged quiescent luminosity $\langle L_q \rangle$ in clusters of size $N \in \{2, 4, 8, 16, 32, 64, 128, 256, 1024\}$ (from left to right). $\langle L_q \rangle$ increases linearly as a function of the number N of cluster members (note the log-log scaling on the axes).

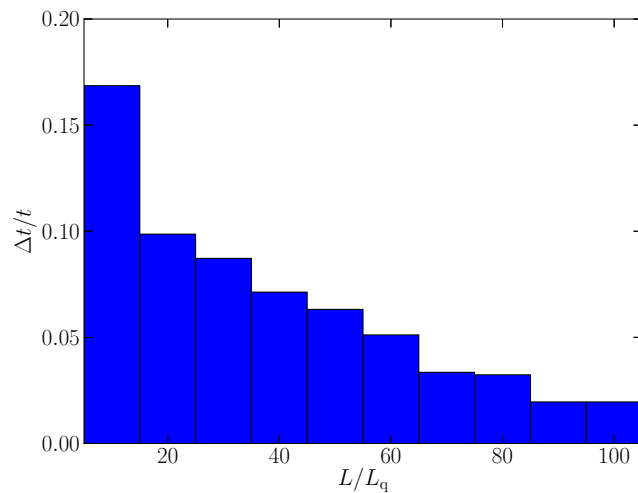


Figure 4.8: Histogram of the fractional duration of time $\Delta t/t$ that an $N = 16$ member cluster spends at an elevated luminosity, in factors of the quiescent luminous rate, as indicated along the horizontal axis. The cluster's star forming phase lasts ~ 26 kyr, about 16% of which is spent at luminosities $> 10 \times L_q$ and about 1% of which is spent at luminosities $> 100 \times L_q$. The cluster's time-averaged quiescent luminosity is approximately $4 \times 10^5 L_\odot$.

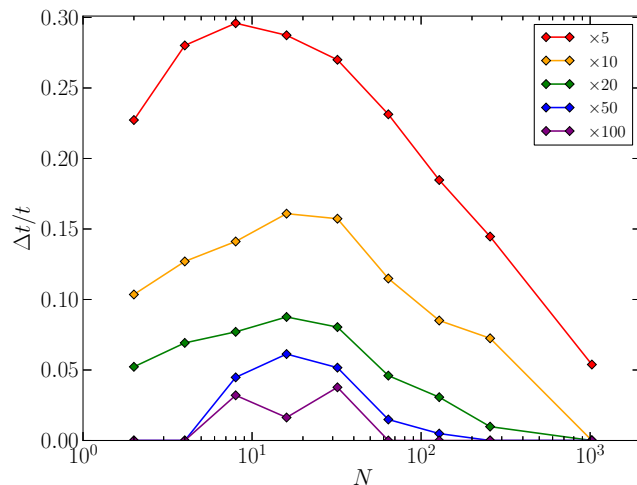


Figure 4.9: Each of the curves above traces the fractional duration of time (with respect to the total protostellar phase; $\Delta t/t$) that a cluster of a given size N spends at an elevated luminosity (in multiples of the cluster’s quiescent rate, i.e., L/L_q). The fractional duration of time that a cluster spends at an elevated luminosity ($L > L_q$) increases with increasing N , reaching a maximum at $N \simeq 16$. Larger clusters exhibit less and less variability above the mean quiescent rate $\langle L_q \rangle$.

4.5 Discussion & Conclusions

We have presented a scenario for the assembly of a cluster of first stars formed in the early universe. Primordial pristine gas pools inside dark matter halos of mass 10^5 to $10^6 M_\odot$ that have virialized and collapsed by redshift $z \sim 20 - 50$. The morphology of the dark matter, just before its virialization, imprints a pattern onto the initially smooth gas, establishing the loci of subsequent sub-fragmentation. In this context we find that the Jeans criterion provides a sufficient basis for understanding the subsequent fragmentation of the gas, which results in massive clumps on the order of 10^4 to $10^5 M_\odot$. This imprint is responsible for setting the dynamical parameters of the clump. The masses of these clumps as estimated in the Jeans analysis agree with the results of recent theoretical and computational work on the formation of the first stars (e.g., Yoshida et al., 2003, 2006; Hosokawa et al., 2011). We estimate that a typical dark matter halo with mass between 10^5 and $10^6 M_\odot$ to contain 10% by mass of gas, and roughly a further 10% of which actually goes into stars—that is, the progenitors of star formation are clumps with masses on the order of a few times $100 M_\odot$. This results in clusters containing tens of members (perhaps 10 – 50 protostars), though the specific numbers are difficult to estimate due to the ambiguity with which the dispersal and merger of clumps prior to their collapse occurs (e.g., Greif et al., 2011).

We employ numerical hydrodynamics simulations in the thin-disk limit to then investigate

the long-term evolution of these clumps. We model their collapse self-consistently into the formation of the protostar and its surrounding disk. The disk forms relatively quickly regardless of the initial conditions, within a few kyr of the formation of the protostar. The disk is centrifugally supported, but its mass lends it to being gravitationally unstable. We observe a rapid and episodic fragmentation of the disk during which fragments having between $0.1 - 1.0 M_{\odot}$ are formed at typical radii of ~ 50 AU. The fragments are torqued inward toward the central protostar where they are then accreted, resulting in massive bursts of luminosity that can exceed the mean rate by as much as two orders of magnitude, occasionally exceeding $10^6 L_{\odot}$ (as in Figure 4.5).

In the context of this formation scenario we analyze the luminosity profiles that are produced by a multiplicity of first stars that form approximately coevally within a young cluster. We assume that each cluster member forms independently and harbors its own disk that is subject to gravitationally induced episodic fragmentation and accretion (i.e., the burst mode of accretion). With increasing numbers of cluster members, the quiescent luminosity of the cluster steadily increases. However, increases in the number of cluster members also increase the probability that two or more members simultaneously experience a burst of accretion. In one cluster simulation we observe a particularly luminous accretion event that raises the cluster luminosity to nearly $1000\times$ its quiescent rate, to $2.48\times 10^8 L_{\odot}$ (Figure 4.6).

Competition between these two effects results in clusters of a certain size ($N \simeq 16$) spending a sizable fraction of their star forming life-time (roughly 15%) at luminosities $10\times$ greater than might otherwise be expected with smooth accretion (e.g., Smith et al., 2012a). Each additional object added to a cluster raises the mean/quiescent luminosity of the cluster, and this in turn tends to suppress the prominence of individual and multiple burst events in clusters in which $N \gtrsim 16$. Such moderately sized clusters are also the most easily manufactured, capable of being produced assuming even a relatively low star formation efficiency, and are of a number as has been counted in a variety of theoretical Population III star forming scenarios to date (e.g., Stacy et al., 2010; Clark et al., 2011; Greif et al., 2011).

The possible formation of clusters of Population III stars in the dark matter halos of the early universe provides a unique opportunity for observations. Rydberg et al. (2013) estimated the total luminosity from even the most upper mass estimates of Population III stars (i.e., those with masses $\sim 300 M_{\odot}$) and found that even these were likely too faint to be observed by next-generation telescopes such as the James Webb Space Telescope. The likelihood for such instruments to observe even lower mass Population III stars is thus highly improbable. However, as we have shown, clusters of even low mass Population III stars (as others have also indicated may exist: Bromm et al. 2003; Clark et al. 2008; and Greif et al. 2012), are capable of producing luminosities in excess of lone very massive Population III stars—for example

Bromm et al. (2001) estimate luminosities in the range $\simeq 10^6 - 10^7 L_{\odot}$ for Population III stars with masses in the range $100 - 500 M_{\odot}$, which is the same amount of luminosity produced by the most massive individual burst events observed in our simulations. The peak wavelength of emission from such events is also favorably situated observationally. For the most massive events (again, luminosities on the order of $10^6 L_{\odot}$), the peak wavelength of emission can be estimated to fall in the UV regime, around a few times 10 nm. Depending on the precise redshift of the emission ($\lambda_{\text{obs}} = \lambda_{\text{emit}}(1 + z)$), the peak wavelength of emission today is most likely to be observed at infrared wavelengths (assuming such cluster begin forming quickly at $z \sim 20$). Observational constraints on the early stages of reionization, from 21 cm observations by the Square Kilometer Array (e.g., Carilli et al., 2004) may actually provide indirect constraints on the density of such clusters in the plane of the sky. However, it will be in the next decade that next-generation telescopes may actually provide direct constraints on the Population III star formation taking place in the early universe; with clusters of Population III stars being some of the most luminous at that epoch.

Bibliography

- Abel, T., Anninos, P., Norman, M. L., & Zhang, Y. 1998, *ApJ*, 508, 518
- Abel, T., Bryan, G. L., & Norman, M. L. 2002, *Science*, 295, 93
- Barnes, J. & Efstathiou, G. 1987, *ApJ*, 319, 575
- Basu, S. 1997, *ApJ*, 485, 240
- Bond, J. R., Arnett, W. D., & Carr, B. J. 1984, *ApJ*, 280, 825
- Bromm, V., Coppi, P. S., & Larson, R. B. 1999, *ApJL*, 527, L5
- . 2002, *ApJ*, 564, 23
- Bromm, V., Kudritzki, R. P., & Loeb, A. 2001, *ApJ*, 552, 464
- Bromm, V. & Loeb, A. 2004, *Nature*, 9, 353
- Carilli, C. L., Furlanetto, S., Briggs, F., Jarvis, M., Rawlings, S., & Falcke, H. 2004, *New Astron. Rev.*, 48, 1029
- Carpenter, J. M., Meyer, M. R., Dougados, C., Strom, S. E., & Hillenbrand, L. A. 1997, *AJ*, 114, 198
- Ciardi, B. & Ferrara, A. 2001, *MNRAS*, 324, 648
- Clark, P. C., Glover, S. C. O., & Klessen, R. S. 2008, *ApJ*, 672, 757
- Clark, P. C., Glover, S. C. O., Smith, R. J., Greif, T. H., Klessen, R. S., & Bromm, V. 2011, *Science*, 331, 1040
- Clarke, C. J. 2009, *MNRAS*, 396, 1066
- Clarke, C. J. & Bromm, V. 2003, *MNRAS*, 343, 1224
- Dapp, W. B. & Basu, S. 2009, *MNRAS*, 395, 1092

- Ferrara, A., Pettini, M., & Shchekinov, Y. 2000, MNRAS, 319, 539
- Gardner, J. P. 2001, ApJ, 557, 616
- Gnedin, N. Y. & Ostriker, J. P. 1997, ApJ, 486, 581
- Greif, T. H., Bromm, V., Clark, P. C., Glover, S. C. O., Smith, R. J., Klessen, R. S., Yoshida, N., & Springel, V. 2012, MNRAS, 3229
- Greif, T. H., Springel, V., White, S. D. M., Glover, S. C. O., Clark, P. C., Smith, R. J., Klessen, R. S., & Bromm, V. 2011, ApJ, 737, 75
- Gutermuth, R. A., Megeath, S. T., Myers, P. C., Allen, L. E., Pipher, J. L., & Fazio, G. G. 2009, ApJS, 184, 18
- Hillenbrand, L. A. 1997, AJ, 113, 1733
- Hirano, S., Hosokawa, T., Yoshida, N., Umeda, H., Omukai, K., Chiaki, G., & Yorke, H. W. 2014, ApJ, 781, 60
- Hosokawa, T. & Omukai, K. 2009, ApJ, 691, 823
- Hosokawa, T., Omukai, K., Yoshida, N., & Yorke, H. W. 2011, Science, 334, 1250
- Johnson, J. L. 2010, MNRAS, 404, 1425
- Johnstone, D., Wilson, C. D., Moriarty-Schieven, G., Joncas, G., Smith, G., Gregersen, E., & Fich, M. 2000, ApJ, 545, 327
- Lada, C. J. & Lada, E. A. 2003, AR&AA, 41, 57
- Lin, C. C., Mestel, L., & Shu, F. H. 1965, ApJ, 142, 1431
- Miralda-Escudé, J. & Rees, M. J. 1997, ApJL, 478, L57
- Omukai, K. & Nishi, R. 1998, ApJ, 508, 141
- Omukai, K. & Palla, F. 2003, ApJ, 589, 677
- Omukai, K., Tsuribe, T., Schneider, R., & Ferrara, A. 2005, ApJ, 626, 627
- Onishi, T., Mizuno, A., Kawamura, A., Ogawa, H., & Fukui, Y. 1998, ApJ, 502, 296
- O'Shea, B. W. & Norman, M. L. 2007, ApJ, 654, 66

- Rydberg, C.-E., Zackrisson, E., Lundqvist, P., & Scott, P. 2013, *MNRAS*, 429, 3658
- Ryden, B. S. 1988, *ApJ*, 329, 589
- Safranek-Shrader, C., Milosavljević, M., & Bromm, V. 2014, *MNRAS*, 438, 1669
- Scannapieco, E., Schneider, R., & Ferrara, A. 2003, *ApJ*, 589, 35
- Shu, F. H. 1977, *ApJ*, 214, 488
- Smith, R. J., Hosokawa, T., Omukai, K., Glover, S. C. O., & Klessen, R. S. 2012a, *MNRAS*, 3212
- . 2012b, *MNRAS*, 424, 457
- Stacy, A., Greif, T. H., & Bromm, V. 2010, *MNRAS*, 403, 45
- Stahler, S. W., Palla, F., & Salpeter, E. E. 1986, *ApJ*, 302, 590
- Stamatellos, D. & Whitworth, A. P. 2008, *A&A*, 480, 879
- Stone, J. M. & Norman, M. L. 1992, *ApJS*, 80, 753
- Tan, J. C. & McKee, C. F. 2004, *ApJ*, 603, 383
- Tegmark, M., Silk, J., Rees, M. J., Blanchard, A., Abel, T., & Palla, F. 1997, *ApJ*, 474, 1
- Toomre, A. 1964, *ApJ*, 139, 1217
- Tornatore, L., Ferrara, A., & Schneider, R. 2007, *MNRAS*, 382, 945
- Tumlinson, J. & Shull, J. M. 2000, *ApJL*, 528, L65
- Turk, M. J., Abel, T., & O'Shea, B. 2009, *Science*, 325, 601
- Vorobyov, E. I. & Basu, S. 2005, *ApJL*, 633, L137
- . 2006, *ApJ*, 650, 956
- . 2010, *ApJ*, 719, 1896
- Vorobyov, E. I., DeSouza, A. L., & Basu, S. 2013, *ApJ*, 768, 131
- Windhorst, R. A., Cohen, S. H., Jansen, R. A., Conselice, C., & Yan, H. 2006, *New Astron. Rev.*, 50, 113

Yoshida, N., Abel, T., Hernquist, L., & Sugiyama, N. 2003, *ApJ*, 592, 645

Yoshida, N., Omukai, K., & Hernquist, L. 2008, *Science*, 321, 669

Yoshida, N., Omukai, K., Hernquist, L., & Abel, T. 2006, *ApJ*, 652, 6

Chapter 5

Conclusions

Our understanding of star formation in both the present-day and early universe has grown tremendously over the last decade. Many processes, including viscous accretion, dust settling, dynamical interactions, and photoevaporation by UV and X-ray radiation, have all been recognized as being important in determining the ultimate fate of protostellar disks. Debate as to their relative degrees of importance continues. In the context of primordial star formation there has been a falling out of favor of the picture of massive Population III stars forming in isolation. In its place has arisen a paradigm not so dissimilar from how star formation is thought to proceed in the nearby metal-rich universe: the formation of disks, their fragmentation, and even the possibility for the coëval formation of low-mass Population III companions, are each seen as viable outcomes of the process. Clearly the study of protostellar disks is an essential component of understanding star formation in all epochs.

In Chapter 2, we investigated the long-term evolution of disks around present-day protostars. Starting from initial conditions derived from robust 2D numerical hydrodynamics simulations of collapsing protostellar cores, we investigated the evolution of numerous protostellar-disk systems across two orders of magnitude in M_* . We parameterized the action of gravitationally-induced torques acting within the disk in terms of Toomre’s Q parameter. By drawing comparisons between the results of our models and the observational inferences of protostellar masses and their accretion rates, we have shown that the observed correlation— $\dot{M} \propto M_*^{-1.3}$ —and the scatter therein, is statistically reproducible. This is a direct result of the bimodal accretion history that is an outcome of gravitationally-induced torque driven angular momentum transport within the protostellar disks of our models. Even though other accretion mechanisms may be required for a more complete understanding, our results show that gravitational torques alone can go a long way toward explaining the observed correlation.

Chapter 3 presents the extension and expansion of this inquiry into the formation of the first stars. We explicitly model the self-consistent formation and evolution of disks around the

first protostars in the early universe, and provided the first evidence that these stars accrete mass via a burst mode of accretion. This is an entirely novel mechanism in contrast to the classical analytic scenario of smooth monolithic collapse, in which a single pre-stellar clump yields a singular and isolated massive star. The resupply of material that falls onto the disk at large radii establishes a pattern of recurrent gravitational–instability-driven fragmentation, as has been noted to occur in models of present-day disk evolution. Although most fragments are torqued inward onto the protostar, several alternative fates have been found to exist. Fragments capable of settling into stable orbits may evolve in conjunction with their hosts to form binary-pairs of first stars. A notion that has recently been invoked to explain the abundance patterns of at least two hyper metal-poor ($[\text{Fe}/\text{H}] < -5$) stars (e.g., [??](#)), in which a unique history of mass transfer occurs between a first star and its low-mass binary companion. We also posit that some of these fragments may be ejected to substantially larger orbits as a result of N -body-like interactions; raising the tantalizing possibility of a heretofore unseen population of low-mass primordial stars that may have survived into the present day.

Finally, in Chapter 4 we present a scenario for the assembly of a cluster of first stars. We posit that primordial gas that pools into dark matter halos in the early-universe may in fact inherit the imprint of the pre-virialization morphology. This in turn allows the gas to fragment into a multiplicity of young first stars. In this context we find that the Jeans criterion provides a sufficient basis for understanding this fragmentation, which results in massive clumps on the order of 10^2 to $10^3 M_{\odot}$, and thus clusters containing 10+ members (depending on the star formation efficiency). Utilizing numerical hydrodynamics simulations in the thin-disk limit we investigate the evolution of the cluster members, specifically calculating the accretion luminosity of these first stars prior to the onset of strong UV irradiation. There is a higher probability that two or more cluster members simultaneously experience a burst of accretion. Although such events are rare, in the context of the total accretion history of the cluster, these events are capable of producing luminous bursts that can be on the order $1000\times$ brighter than the cluster itself, reaching luminosities approaching $10^9 L_{\odot}$. However, this effect competes with the increases in a cluster’s mean luminosity as membership increases. As a result of the suppression of the prominence of individual and multiple burst events for clusters containing a very large number of members, we find that the clusters that exhibit the greatest luminosity variations tend to be those with only $\sim 10 - 20$ members, which is also the most likely cluster size.

It is clear that gravitational torques and instabilities are capable of producing significant enough effects in the protostellar environment that there are multiple avenues for detecting the signature of (for example) the burst mode of accretion. Next generation telescopes such as the Atacama Large Millimeter Array (ALMA), the James Webb Space Telescope (JWST), and the

European Extremely Large Telescope (E-ELT), are all poised to be able to provide a wealth of new insights into the nature of star formation across cosmic time. Additionally, stellar archaeology will continue to reveal more about metallicity production in the early universe, placing tighter constraints on primordial star formation. With large-scale surveys such as the Sloan Extension for Galactic Understanding, we will gain more knowledge of the chemical abundance patterns within stars residing in the local universe. The possibility remains for a truly metal-free star to be discovered in our own Milky Way or in nearby dwarf galaxies, observationally confirming the existence of low-mass Population III stars. There remain many avenues of exploration available for understanding the specific physics at work in the early protostellar environment, now and in the early universe—the ultimate goal of which is to understand how the universe came to be in its present state.

Bibliography

Abel, T., Anninos, P., Norman, M. L., & Zhang, Y. 1998, *ApJ*, 508, 518

Abel, T., Bryan, G. L., & Norman, M. L. 2000, *ApJ*, 540, 39

—. 2002, *Science*, 295, 93

Alexander, R. D. & Armitage, P. J. 2006, *ApJL*, 639, L83

Allen, A., Li, Z.-Y., & Shu, F. H. 2003, *ApJ*, 599, 363

André, P., Basu, S., & Inutsuka, S. 2009, in *Structure Formation in Astrophysics*, ed. G. Chabrier (Cambridge University Press)

André, P., Ward-Thompson, D., & Barsony, M. 1993, *ApJ*, 406, 122

Andrews, S. M. & Williams, J. P. 2005, *ApJ*, 631, 1134

Andrews, S. M., Wilner, D. J., Hughes, A. M., Qi, C., & Dullemond, C. P. 2009, *ApJ*, 700, 1502

Armitage, P. J., Livio, M., & Pringle, J. E. 2001, *MNRAS*, 324, 705

Balbus, S. A. & Hawley, J. F. 1991, *ApJ*, 376, 214

—. 1998, *Reviews of Modern Physics*, 70, 1

Barnes, J. & Efstathiou, G. 1987, *ApJ*, 319, 575

Basu, S. 1997, *ApJ*, 485, 240

—. 1998, *ApJ*, 509, 229

Basu, S. & Mouschovias, T. C. 1994, *ApJ*, 432, 720

Basu, S. & Vorobyov, E. I. 2012, *ApJ*, 750, 30

- Beckwith, S. V. W., Sargent, A. I., Chini, R. S., & Guesten, R. 1990, *ApJ*, 99, 924
- Binney, J. & Tremaine, S. 1987, *Galactic Dynamics* (Princeton University Press)
- . 2008, *Galactic Dynamics* (Princeton University Press)
- Blaes, O. M. & Balbus, S. A. 1994, *ApJ*, 421, 163
- Bodenheimer, P. 1995, *ARA&A*, 33, 199
- Bodenheimer, P., Laughlin, G. P., Różyczka, M., & Yorke, H. W. 2007, *Numerical Methods in Astrophysics: An Introduction* (Taylor & Francis Group)
- Boley, A. C., Mejía, A. C., Durisen, R. H., Cai, K., Pickett, M. K., & D'Alessio, P. 2006, *ApJ*, 651, 517
- Bond, J. R., Arnett, W. D., & Carr, B. J. 1984, *ApJ*, 280, 825
- Boss, A. P. 1997, *Science*, 276, 1836
- . 2001, *ApJ*, 563, 367
- Brandenburg, A., Nordlund, A., Stein, R. F., & Torkelsson, U. 1995, *ApJ*, 446, 741
- Bromm, V., Coppi, P. S., & Larson, R. B. 1999, *ApJL*, 527, L5
- . 2002, *ApJ*, 564, 23
- Bromm, V., Kudritzki, R. P., & Loeb, A. 2001, *ApJ*, 552, 464
- Bromm, V. & Larson, R. B. 2004, *ARA&A*, 42, 79
- Bromm, V. & Loeb, A. 2004, *Nature*, 9, 353
- Caffau, E., Bonifacio, P., François, P., Sbordone, L., Monaco, L., Spite, M., Spite, F., Ludwig, H.-G., Cayrel, R., Zaggia, S., Hammer, F., Randich, S., Molaro, P., & Hill, V. 2011, *Nature*, 477, 67
- Carilli, C. L., Furlanetto, S., Briggs, F., Jarvis, M., Rawlings, S., & Falcke, H. 2004, *New Astron. Rev.*, 48, 1029
- Carpenter, J. M., Meyer, M. R., Dougados, C., Strom, S. E., & Hillenbrand, L. A. 1997, *AJ*, 114, 198

- Chabrier, G. 2005, in *The Initial Mass Function 50 Years Later*, ed. E. Corbelli, F. Palla, & H. Zinnecker, 41
- Chiang, E. & Youdin, A. N. 2010, *AREPS*, 38, 493
- Ciardi, B. & Ferrara, A. 2001, *MNRAS*, 324, 648
- Clark, P. C., Glover, S. C. O., & Klessen, R. S. 2008, *ApJ*, 672, 757
- Clark, P. C., Glover, S. C. O., Klessen, R. S., & Bromm, V. 2011a, *ApJ*, 727, 110
- Clark, P. C., Glover, S. C. O., Smith, R. J., Greif, T. H., Klessen, R. S., & Bromm, V. 2011b, *Science*, 331, 1040
- Clarke, C. J. 2009, *MNRAS*, 396, 1066
- Clarke, C. J. & Bromm, V. 2003, *MNRAS*, 343, 1224
- Cole, S., Percival, W. J., Peacock, J. A., Norberg, P., Baugh, C. M., Frenk, C. S., Baldry, I., Bland-Hawthorn, J., Bridges, T., Cannon, R., Colless, M., Collins, C., Couch, W., Cross, N. J. G., Dalton, G., Eke, V. R., De Propris, R., Driver, S. P., Efstathiou, G., Ellis, R. S., Glazebrook, K., Jackson, C., Jenkins, A., Lahav, O., Lewis, I., Lumsden, S., Maddox, S., Madgwick, D., Peterson, B. A., Sutherland, W., & Taylor, K. 2005, *MNRAS*, 362, 505
- Cossins, P., Lodato, G., & Clarke, C. J. 2009, *MNRAS*, 393, 1157
- Couchman, H. M. P. & Rees, M. J. 1986, *MNRAS*, 221, 53
- D'Alessio, P., Calvet, N., & Hartmann, L. 2001, *ApJ*, 553, 321
- Dapp, W. B. & Basu, S. 2009, *MNRAS*, 395, 1092
- . 2010, *A&A*, 521, L56
- Dapp, W. B., Basu, S., & Kunz, M. W. 2012, *A&A*, 541, A35
- Davis, M., Efstathiou, G., Frenk, C. S., & White, S. D. M. 1985, *ApJ*, 292, 371
- Dicke, R. H., Peebles, P. J. E., Roll, P. G., & Wilkinson, D. T. 1965, *ApJ*, 142, 414
- Dullemond, C. P., Natta, A., & Testi, L. 2006, *ApJL*, 645, L69
- Eisner, J. A. & Carpenter, J. M. 2006, *ApJ*, 641, 1162
- Ercolano, B., Mayr, D., Owen, J. E., Rosotti, G., & Manara, C. F. 2014, *MNRAS*, 439, 256

- Ferrara, A., Pettini, M., & Shchekinov, Y. 2000, *MNRAS*, 319, 539
- Fleming, T. & Stone, J. M. 2003, *ApJ*, 585, 908
- Frebel, A., Aoki, W., Christlieb, N., Ando, H., Asplund, M., Barklem, P. S., Beers, T. C., Eriksson, K., Fechner, C., Fujimoto, M. Y., Honda, S., Kajino, T., Minezaki, T., Nomoto, K., Norris, J. E., Ryan, S. G., Takada-Hidai, M., Tsangarides, S., & Yoshii, Y. 2005, *Nature*, 434, 871
- Frieman, J. A., Turner, M. S., & Huterer, D. 2008, *ARA&A*, 46, 385
- Fromang, S., Terquem, C., & Balbus, S. A. 2002, *MNRAS*, 329, 18
- Fukagawa, M., Hayashi, M., Tamura, M., Itoh, Y., Hayashi, S. S., Oasa, Y., Takeuchi, T., Morino, J.-i., Murakawa, K., Oya, S., Yamashita, T., Suto, H., Mayama, S., Naoi, T., Ishii, M., Pyo, T.-S., Nishikawa, T., Takato, N., Usuda, T., Ando, H., Iye, M., Miyama, S. M., & Kaifu, N. 2004, *ApJL*, 605, L53
- Gammie, C. F. 2001, *ApJ*, 553, 174
- Garcia, P. J. V., Cabrit, S., Ferreira, J., & Binette, L. 2001, *A&A*, 377, 609
- Gardner, J. P. 2001, *ApJ*, 557, 616
- Gnedin, N. Y. & Ostriker, J. P. 1997, *ApJ*, 486, 581
- Goodman, A. A., Benson, P. J., Fuller, G. A., & Myers, P. C. 1993, *ApJ*, 406, 528
- Grady, C. A., Polomski, E. F., Henning, T., Stecklum, B., Woodgate, B. E., Telesco, C. M., Piña, R. K., Gull, T. R., Boggess, A., Bowers, C. W., Bruhweiler, F. C., Clampin, M., Danks, A. C., Green, R. F., Heap, S. R., Hutchings, J. B., Jenkins, E. B., Joseph, C., Kaiser, M. E., Kimble, R. A., Kraemer, S., Lindler, D., Linsky, J. L., Maran, S. P., Moos, H. W., Plait, P., Roesler, F., Timothy, J. G., & Weistrop, D. 2001, *AJ*, 122, 3396
- Greif, T. H., Bromm, V., Clark, P. C., Glover, S. C. O., Smith, R. J., Klessen, R. S., Yoshida, N., & Springel, V. 2012, *MNRAS*, 3229
- Greif, T. H., Springel, V., White, S. D. M., Glover, S. C. O., Clark, P. C., Smith, R. J., Klessen, R. S., & Bromm, V. 2011, *ApJ*, 737, 75
- Gutermuth, R. A., Megeath, S. T., Myers, P. C., Allen, L. E., Pipher, J. L., & Fazio, G. G. 2009, *ApJS*, 184, 18

- Hartmann, L. 2009, *Accretion Processes in Star Formation* (Cambridge University Press)
- Hartmann, L., Calvet, N., Gullbring, E., & D'Alessio, P. 1998, *ApJ*, 495, 385
- Hartmann, L., D'Alessio, P., Calvet, N., & Muzerolle, J. 2006, *ApJ*, 648, 484
- Hawley, J. F., Gammie, C. F., & Balbus, S. A. 1996, *ApJ*, 464, 690
- Hayashi, C. 1981, *Progress of Theoretical Physics Supplement*, 70, 35
- Hennebelle, P. & Fromang, S. 2008, *A&A*, 477, 9
- Herczeg, G. J. & Hillenbrand, L. A. 2008, *ApJ*, 681, 594
- Hernández, J., Hartmann, L., Calvet, N., Jeffries, R. D., Gutermuth, R., Muzerolle, J., & Stauffer, J. 2008, *ApJ*, 686, 1195
- Hillenbrand, L. A. 1997, *AJ*, 113, 1733
- Hinshaw, G., Larson, D., Komatsu, E., Spergel, D. N., Bennett, C. L., Dunkley, J., Nolte, M. R., Halpern, M., Hill, R. S., Odegard, N., Page, L., Smith, K. M., Weiland, J. L., Gold, B., Jarosik, N., Kogut, A., Limon, M., Meyer, S. S., Tucker, G. S., Wollack, E., & Wright, E. L. 2013, *ApJS*, 208, 19
- Hirano, S., Hosokawa, T., Yoshida, N., Umeda, H., Omukai, K., Chiaki, G., & Yorke, H. W. 2014, *ApJ*, 781, 60
- Hosokawa, T. & Omukai, K. 2009, *ApJ*, 691, 823
- Hosokawa, T., Omukai, K., Yoshida, N., & Yorke, H. W. 2011, *Science*, 334, 1250
- Hubble, E. 1929, *PNAS*, 15, 168
- Hueso, R. & Guillot, T. 2005, *A&A*, 442, 703
- Jeans, J. H. 1902, *Royal Society of London Philosophical Transactions Series A*, 199, 1
- Johnson, B. M. & Gammie, C. F. 2005, *ApJ*, 635, 149
- Johnson, J. L. 2010, *MNRAS*, 404, 1425
- Johnstone, D., Wilson, C. D., Moriarty-Schieven, G., Joncas, G., Smith, G., Gregersen, E., & Fich, M. 2000, *ApJ*, 545, 327
- Klahr, H. H. & Bodenheimer, P. 2003, *ApJ*, 582, 869

- Krasnopolsky, R., Li, Z.-Y., & Blandford, R. D. 2003, *ApJ*, 595, 631
- Kratter, K. M., Matzner, C. D., Krumholz, M. R., & Klein, R. I. 2010, *ApJ*, 708, 1585
- Lada, C. J. 2006, *ApJL*, 640, L63
- Lada, C. J. & Lada, E. A. 2003, *AR&AA*, 41, 57
- Lada, C. J. & Wilking, B. A. 1984, *ApJ*, 287, 610
- Larson, R. B. 1969, *MNRAS*, 145, 271
- . 1985, *MNRAS*, 214, 379
- . 2003, *Reports on Progress in Physics*, 66, 1651
- Lemaître, A. G. 1931, *Nature*, 128, 704
- Lin, C. C., Mestel, L., & Shu, F. H. 1965, *ApJ*, 142, 1431
- Lin, D. N. C. & Papaloizou, J. 1980, *MNRAS*, 191, 37
- Lin, D. N. C. & Pringle, J. E. 1987, *MNRAS*, 225, 607
- Lodato, G. 2008, *NAR*, 52, 21
- Lodato, G. & Rice, W. K. M. 2004, *MNRAS*, 351, 630
- Loeb, A. 2010, *How Did the First Stars and Galaxies Form* (Princeton University Press)
- Lynden-Bell, D. & Pringle, J. E. 1974, *MNRAS*, 168, 603
- Machida, M. N., Inutsuka, S.-i., & Matsumoto, T. 2010, *ApJ*, 724, 1006
- . 2011, *ApJ*, 729, 42
- Machida, M. N., Omukai, K., Matsumoto, T., & Inutsuka, S.-i. 2008, *ApJ*, 677, 813
- McCaughrean, M. J. & O'Dell, C. R. 1996, *AJ*, 111, 1977
- McKee, C. F. & Tan, J. C. 2008, *ApJ*, 681, 771
- Mellon, R. R. & Li, Z.-Y. 2008, *ApJ*, 681, 1356
- Miralda-Escudé, J. 2003, *Science*, 300, 1904
- Miralda-Escudé, J. & Rees, M. J. 1997, *ApJL*, 478, L57

- Muto, T., Grady, C. A., Hashimoto, J., Fukagawa, M., Hornbeck, J. B., Sitko, M., Russell, R., Werren, C., Curé, M., Currie, T., Ohashi, N., Okamoto, Y., Momose, M., Honda, M., Inutsuka, S., Takeuchi, T., Dong, R., Abe, L., Brandner, W., Brandt, T., Carson, J., Egner, S., Feldt, M., Fukue, T., Goto, M., Guyon, O., Hayano, Y., Hayashi, M., Hayashi, S., Henning, T., Hodapp, K. W., Ishii, M., Iye, M., Janson, M., Kandori, R., Knapp, G. R., Kudo, T., Kusakabe, N., Kuzuhara, M., Matsuo, T., Mayama, S., McElwain, M. W., Miyama, S., Morino, J.-I., Moro-Martin, A., Nishimura, T., Pyo, T.-S., Serabyn, E., Suto, H., Suzuki, R., Takami, M., Takato, N., Terada, H., Thalmann, C., Tomono, D., Turner, E. L., Watanabe, M., Wisniewski, J. P., Yamada, T., Takami, H., Usuda, T., & Tamura, M. 2012, *ApJL*, 748, L22
- Muzerolle, J., Luhman, K. L., Briceño, C., Hartmann, L., & Calvet, N. 2005, *ApJ*, 625, 906
- Myers, P. C. & Benson, P. J. 1983, *ApJ*, 266, 309
- Nakano, T., Nishi, R., & Umebayashi, T. 2002, *ApJ*, 573, 199
- O'Dell, C. R. & Wen, Z. 1994, *ApJ*, 436, 194
- Omukai, K. & Nishi, R. 1998, *ApJ*, 508, 141
- Omukai, K. & Palla, F. 2003, *ApJ*, 589, 677
- Omukai, K., Tsuribe, T., Schneider, R., & Ferrara, A. 2005, *ApJ*, 626, 627
- Onishi, T., Mizuno, A., Kawamura, A., Ogawa, H., & Fukui, Y. 1998, *ApJ*, 502, 296
- O'Shea, B. W. & Norman, M. L. 2007, *ApJ*, 654, 66
- Penston, M. V. 1969, *MNRAS*, 144, 425
- Penzias, A. A. & Wilson, R. W. 1965, *ApJ*, 142, 419
- Perlmutter, S., Aldering, G., della Valle, M., Deustua, S., Ellis, R. S., Fabbro, S., Fruchter, A., Goldhaber, G., Groom, D. E., Hook, I. M., Kim, A. G., Kim, M. Y., Knop, R. A., Lidman, C., McMahon, R. G., Nugent, P., Pain, R., Panagia, N., Pennypacker, C. R., Ruiz-Lapuente, P., Schaefer, B., & Walton, N. 1998, *Nature*, 391, 51
- Pringle, J. E. 1981, *ARA&A*, 19, 137
- Pudritz, R. E. & Silk, J. 1989, *ApJ*, 342, 650
- Rice, W. K. M. & Armitage, P. J. 2009, *MNRAS*, 396, 2228

- Rice, W. K. M., Armitage, P. J., Bate, M. R., & Bonnell, I. A. 2003, *MNRAS*, 339, 1025
- Riess, A. G., Filippenko, A. V., Challis, P., Clocchiatti, A., Diercks, A., Garnavich, P. M., Gilliland, R. L., Hogan, C. J., Jha, S., Kirshner, R. P., Leibundgut, B., Phillips, M. M., Reiss, D., Schmidt, B. P., Schommer, R. A., Smith, R. C., Spyromilio, J., Stubbs, C., Suntzeff, N. B., & Tonry, J. 1998, *AJ*, 116, 1009
- Riess, A. G., Strolger, L.-G., Tonry, J., Casertano, S., Ferguson, H. C., Mobasher, B., Challis, P., Filippenko, A. V., Jha, S., Li, W., Chornock, R., Kirshner, R. P., Leibundgut, B., Dickinson, M., Livio, M., Giavalisco, M., Steidel, C. C., Benítez, T., & Tsvetanov, Z. 2004, *ApJ*, 607, 665
- Rigliaco, E., Natta, A., Randich, S., Testi, L., & Biazzo, K. 2011, *A&A*, 525, A47
- Rydberg, C.-E., Zackrisson, E., Lundqvist, P., & Scott, P. 2013, *MNRAS*, 429, 3658
- Ryden, B. S. 1988, *ApJ*, 329, 589
- Safrank-Shrader, C., Milosavljević, M., & Bromm, V. 2014, *MNRAS*, 438, 1669
- Saigo, K., Matsumoto, T., & Umemura, M. 2004, *ApJL*, 615, L65
- Scannapieco, E., Schneider, R., & Ferrara, A. 2003, *ApJ*, 589, 35
- Shakura, N. I. & Sunyaev, R. A. 1973, *A&A*, 24, 337
- Shampine, L. E. 1994, *Numerical Solution of Ordinary Differential Equations* (Chapman & Hall)
- Shu, F. H. 1977, *ApJ*, 214, 488
- Shu, F. H., Adams, F. C., & Lizano, S. 1987, *ARA&A*, 25, 23
- Smith, R. J., Hosokawa, T., Omukai, K., Glover, S. C. O., & Klessen, R. S. 2012a, *MNRAS*, 3212
- . 2012b, *MNRAS*, 424, 457
- Springel, V., White, S. D. M., Jenkins, A., Frenk, C. S., Yoshida, N., Gao, L., Navarro, J., Thacker, R., Croton, D., Helly, J., Peacock, J. A., Cole, S., Thomas, P., Couchman, H., Evrard, A., Colberg, J., & Pearce, F. 2005, *Nature*, 435, 629
- Stacy, A., Greif, T. H., & Bromm, V. 2010, *MNRAS*, 403, 45

- Stahler, S. W., Palla, F., & Salpeter, E. E. 1986, *ApJ*, 302, 590
- Stamatellos, D. & Whitworth, A. P. 2008, *A&A*, 480, 879
- . 2009, *MNRAS*, 400, 1563
- Stone, J. M. & Balbus, S. A. 1996, *ApJ*, 464, 364
- Stone, J. M., Gammie, C. F., Balbus, S. A., & Hawley, J. F. 2000, in *Protostars and Planets IV*, ed. Mannings, V. and Boss, A. P. and Russell, S. S. (University of Arizona Press)
- Stone, J. M. & Norman, M. L. 1992, *ApJS*, 80, 753
- Suda, T., Aikawa, M., Machida, M. N., Fujimoto, M. Y., & Iben, Jr., I. 2004, *ApJ*, 611, 476
- Tan, J. C. & McKee, C. F. 2004, *ApJ*, 603, 383
- Tegmark, M., Silk, J., Rees, M. J., Blanchard, A., Abel, T., & Palla, F. 1997, *ApJ*, 474, 1
- Terebey, S., Shu, F. H., & Cassen, P. 1984, *ApJ*, 286, 529
- Toomre, A. 1964, *ApJ*, 139, 1217
- Tornatore, L., Ferrara, A., & Schneider, R. 2007, *MNRAS*, 382, 945
- Tozzi, P., Madau, P., Meiksin, A., & Rees, M. J. 2000, *ApJ*, 528, 597
- Truelove, J. K., Klein, R. I., McKee, C. F., Holliman, II, J. H., Howell, L. H., Greenough, J. A., & Woods, D. T. 1998, *ApJ*, 495, 821
- Tumlinson, J. & Shull, J. M. 2000, *ApJL*, 528, L65
- Turk, M. J., Abel, T., & O'Shea, B. 2009, *Science*, 325, 601
- Turner, M. S. & Widrow, L. M. 1988, *Phys. Rev. D*, 37, 2743
- Vorobyov, E. I. 2011, *ApJ*, 729, 146
- Vorobyov, E. I. & Basu, S. 2005a, *MNRAS*, 360, 675
- . 2005b, *ApJL*, 633, L137
- . 2006, *ApJ*, 650, 956
- . 2007, *MNRAS*, 381, 1009

- . 2008, *ApJL*, 676, L139
- . 2009a, *MNRAS*, 393, 822
- . 2009b, *ApJ*, 703, 922
- . 2010, *ApJ*, 719, 1896
- Vorobyov, E. I., DeSouza, A. L., & Basu, S. 2013, *ApJ*, 768, 131
- Williams, J. P. & Cieza, L. A. 2011, *ARA&A*, 49, 67
- Windhorst, R. A., Cohen, S. H., Jansen, R. A., Conselice, C., & Yan, H. 2006, *New Astron. Rev.*, 50, 113
- Yorke, H. W., Bodenheimer, P., & Laughlin, G. 1993, *ApJ*, 411, 274
- Yoshida, N., Abel, T., Hernquist, L., & Sugiyama, N. 2003, *ApJ*, 592, 645
- Yoshida, N., Omukai, K., & Hernquist, L. 2008, *Science*, 321, 669
- Yoshida, N., Omukai, K., Hernquist, L., & Abel, T. 2006, *ApJ*, 652, 6
- Zhu, Z., Hartmann, L., Gammie, C., & McKinney, J. C. 2009, *ApJ*, 701, 620
- Zhu, Z., Hartmann, L., Gammie, C. F., Book, L. G., Simon, J. B., & Engelhard, E. 2010, *ApJ*, 713, 1134

Appendix A

Appendix A

The applicability of the thin-disk approximation hinges upon the geometry of the considered configurations. Elongated shapes are typical for protostellar disks in nearby star-forming regions. Specifically, the thin-disk approximation is well justified as long as the aspect ratio $A = Z/r$ of the disk vertical scale height Z to radial distance in the plane of the disk r does not considerably exceed 0.1. This condition is usually fulfilled for disks with sizes up to 1000 AU (see e.g., Vorobyov & Basu, 2010), but its applicability may be less obvious for the evolution phase immediately preceding disk formation, when material accretes directly from the infalling core onto the forming star. Nevertheless, the temporal behaviour and magnitude of the accretion rate onto the star is very similar in the pre-disk stage for spherically symmetric and disk-like cores (Vorobyov & Basu, 2005a, 2006), ensuring that the stellar masses are calculated accurately in our simulations. Below we provide some analytical and numerical estimates justifying our use of the thin-disk approximation.

In a Keplerian disk, the aspect ratio $A = Z/r$ can be expressed as (Vorobyov & Basu, 2010)

$$A \leq \frac{Q_{\text{crit}} M_{\text{disk}}(r)}{CM_*}, \quad (\text{A.1})$$

where $M_{\text{disk}}(r) = \int \Sigma(r, \phi) r dr d\phi$ is the disk mass contained within radius r , M_* is the mass of the central star, Q_{crit} is the critical Toomre parameter, and C is a constant, the actual value of which depends on the gas surface density distribution Σ in the disk. For a disk of constant surface density, C is equal to unity and for the $\Sigma \propto r^{-1.5}$ scaling typical for gravitationally unstable disks (see Figure 3.7), $C = 4$. Adopting a conservative value of $C = 2$ and setting Q_{crit} to unity—characteristic for fragmenting disks—we obtain the radial profile of A shown in Figure A.1 by the dashed line. The ratio $M_{\text{disk}}(r)/M_*$ was calculated using the reference model at $t = 30$ kyr. Evidently, the aspect ratio derived using analytic considerations is smaller than 0.2 in the inner several thousand AU, which validates our use of the thin-disk approximation.

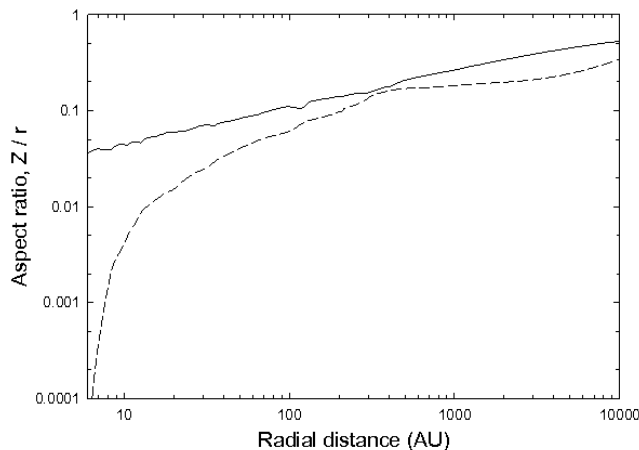


Figure A.1: Aspect ratio A of the disk vertical scale height to radius (Z/r) as a function of radius (r) in the reference model at $t = 30$ kyr after the formation of the central star. The solid line presents the data calculated using the assumption of local vertical hydrostatic equilibrium and the dashed line is derived using equation (??).

We note however that this approximation may become only marginally valid at large r where $M_{\text{disk}}(r)/M_*$ approaches its maximum value.

This estimate is confirmed by the exact calculations of the disk scale height in our models. The azimuthally averaged radial distribution of the aspect ratio $A = Z/r$ in the reference model at $t = 30$ kyr after the formation of the central star is shown by the solid line in Figure A.1. The vertical scale height Z is calculated assuming local vertical hydrostatic equilibrium in the disk using the method described in Vorobyov & Basu (2009). Figure A.1 reinforces our analytical estimate and demonstrates that the thin disk approximation is certainly obeyed within the actual disk, which, according to Figures 3.4 and 3.7, does not exceed 1000 AU in radius. Within this radial extent, the corresponding aspect ratio is below 0.25. Only at radial distances well in excess of 1000 AU might the thin-disk approximation be violated.

Finally, we note that the thin-disk approximation assumes the absence of vertical motions, which turns the usual momentum equation for the z -component of the gas velocity into the equation describing the local vertical hydrostatic equilibrium. This assumption is used to calculate the scale height Z and the aspect ratio A in equation (A.1). Therefore, a possible thick disk that is not in vertical hydrostatic equilibrium is not accessible through our modeling.

Appendix B

Appendix B

In the absence of sink particles, fragment identification on the computational mesh becomes a challenging task. Although from a numerical point of view the fragments are no different than from the rest of the disk, they can be identified based on the following set of physical criteria. First, we scan the disk and locate local maxima in the gas surface density that satisfy

$$\Sigma > \Sigma_{100} \left(\frac{r}{100 \text{ AU}} \right)^{-1.5}, \quad (\text{B.1})$$

where Σ_{100} is the gas surface density at a distance of 100 AU from the central star, and r is the radial distance in AU. A value of $\Sigma_{100} = 5000 \text{ g cm}^{-2}$ is chosen to represent typical densities of the fragments at 100 AU, based on the radial gas surface density profiles shown in Figure 3.7. Consequently, this criterion helps to filter out local maxima, e.g., spiral arms, while retaining those that represent the true fragments, which are usually characterized by a much higher density than the rest of the disk.

Once the radial and azimuthal coordinates of the local maximum, which define the center of a fragment, have been identified on the computational mesh, we determine which of the neighbouring cells also belong to the fragment by imposing the following two conditions on the gas pressure P and gravitational potential Φ

$$\frac{\partial P}{\partial r'} + \frac{1}{r'} \frac{\partial P}{\partial \phi'} < 0, \quad (\text{B.2})$$

$$\frac{\partial \Phi}{\partial r'} + \frac{1}{r'} \frac{\partial \Phi}{\partial \phi'} > 0, \quad (\text{B.3})$$

where $r' = r - r_c$ and $\phi' = \phi - \phi_c$. The first condition mandates that the fragment must be pressure supported, with a negative pressure gradient with respect to the center of the fragment. The second condition requires that the fragment be kept together by gravity, with the potential

well being deepest at the center of the fragment. Although substantial support against gravity may be provided by rotation, we assume it to not invalidate the first criterion.

In practice, we start from the center of the fragment and proceed in eight directions (along the coordinate directions and also at a median angle to them) until one of the above gradient criteria (or both) are violated. This procedure helps to outline an approximate shape of the fragment. We then check all the remaining cells that are encompassed by this shape and retain only those that meet both criteria. In addition, we filter out those cells with a gas surface density lower than that defined by equation (B.1) with $\Sigma_{100} = 5000 \text{ g cm}^{-2}$.

Curriculum Vitae

Name: Alexander Leonard DeSouza

Post-Secondary Education and Degrees: The University of Western Ontario
London, Canada
2010 - 2014 PhD Astronomy & Scientific Computing

The University of Western Ontario
London, Canada
2008 - 2010 MSc Astronomy

The University of Waterloo
Waterloo, Canada
2001 - 2006 BSc Honors Specialization in Astrophysics

Honours and Awards: Graduate Thesis Research Award
The University of Western Ontario
2012

Q.E. II Aiming for the Top Scholarship
The University of Waterloo
2001

Related Work Experience: Research Assistant
The University of Western Ontario
2008 - 2014

Teaching Assistant
The University of Western Ontario
2008 - 2014

Research Assistant
The University of Waterloo
2007 - 2008

Publications:Refereed Publications

1. **DeSouza, A. L.** and Basu, S. (2014), “*The Luminosity of Population III Star Clusters*”, Submitted to MNRAS
2. **DeSouza, A. L.** and Basu, S. (2014), “*The Role of Angular Momentum Transport in Establishing the Accretion Rate–Protostellar Mass Correlation*”, Submitted to New Astronomy
3. Vorobyov, E. I., **DeSouza, A. L.** and Basu, S. (2013), “*The Burst Mode of Accretion in Primordial Star Formation*”, ApJ, 768, 131

Conference Proceedings

1. **DeSouza, A. L.**, Vorobyov, E. I., Basu, S. (2012) “*The Burst Mode of Accretion in Primordial Star Formation*”, First Stars IV ed. Umemura, M., & Omukai, K. AIP Conference Proceedings, 1480, 346
2. Basu, S., Vorobyov, E. I., **DeSouza, A. L.** (2012) “*The Ejection of Low Mass Clumps During Star Formation*”, First Stars IV ed. Umemura, M., & Omukai, K. AIP Conference Proceedings, 1480, 63

Further Contributions

1. **DeSouza, A. L.**, Vorobyov, E. I., Basu, S. “*The Burst Mode of Accretion in Primordial Star Formation.*” The University of Nagoya. Nagoya, Japan (Contributed Talk; May 2012)
2. **DeSouza, A. L.**, Vorobyov, E. I., Basu, S. “*The Burst Mode of Accretion in Primordial Star Formation.*” First Stars IV. Kyoto, Japan (Poster Presentation; May 2012)
3. **DeSouza, A. L.**, Vorobyov, E. I., Basu, S. “*New Insights into Primordial Star Formation.*” Theoretical Physics Workshop. London, Canada (Contributed Talk; April 2012)
4. **DeSouza, A. L.**, Basu, S. “*Circumstellar Accretion Disks.*” Annual Meeting of the Canadian Astronomical Society. London, Canada (Poster Presentation; June 2011)
5. **DeSouza, A. L.**, Vorobyov, E. I., Basu, S. “*The Role of Gravitational Torques in Protostellar Disk Accretion.*” Annual Meeting of the Canadian Astronomical Society. Toronto, Canada (Poster Presentation; June 2009)